

ABSTRACT

Title of Dissertation: ALD-ENABLED CATHODE-CATALYST
ARCHITECTURES FOR LI-O₂ BATTERIES

Marshall Adam Schroeder, Doctor of Philosophy, 2015

Directed By: Professor Gary W. Rubloff
Minta Martin Professor of Engineering
Department of Materials Science and Engineering
Institute for Systems Research

The Li-O₂ electrochemical redox couple is one of the prime candidates for next generation energy storage. Known for its impressive theoretical metric for specific energy, even current practically obtainable values are competitive with state of the art Li-ion intercalation chemistries and the achievable performance of batteries featuring this nascent technology will continue to improve as fundamental scientific challenges in each component of the device are addressed. The positive electrode is particularly complicated by its role as a scaffold for oxygen reduction and evolution, exhibiting sluggish kinetics, poor chemical stability, and limited cyclability due to parasitic side reactions. Fortunately, recent Li-O₂ research has shown some success in improving the performance and cyclability of these O₂ cathodes by shifting toward nanostructured architectures with catalytic functionalizations.

Atomic layer deposition (ALD) is one of the most promising enabling technologies for fabricating these complex heterostructures. Offering precise control of film thickness,

morphology, and mass loading with excellent conformality, this vapor-phase deposition technique is applied in this work to deposit thin film and particle morphologies of different catalyst chemistries on mesostructured carbon scaffolds.

This thesis dissertation discusses: (1) development of a lab-scale infrastructure for assembly, electrochemical testing, and characterization of Li-O₂ battery cathodes including a custom test cell and a state of the art integrated system for fabrication and characterization, (2) design, fabrication, testing, and post-mortem characterization of a unique 3D cathode architecture consisting of vertically aligned carbon nanotubes on an integrated nickel foam current collector, (3) atomic layer deposition of heterogeneous ruthenium-based catalysts on a multi-walled carbon nanotube sponge to produce a freestanding, binder-free, mesoporous Li-O₂ cathode with high capacity and long-term cyclability, (4) evaluation of dimethyl sulfoxide as an electrolyte solvent for non-aqueous Li-O₂ batteries, and (5) investigation of the relative importance of passivating intrinsic defects in carbon redox scaffolds vs. introduction of heterogeneous OER/ORR catalysts for improving the long-term stability and cyclability of these Li-O₂ electrodes.

ALD-ENABLED CATHODE-CATALYST ARCHITECTURES FOR LI-O₂ BATTERIES

By

Marshall Adam Schroeder

Dissertation submitted to the Faculty of the Graduate School of the
University of Maryland, College Park in partial fulfillment
Of the requirements for the degree of
Doctor of Philosophy
2015

Advisory Committee:

Professor Gary Rubloff, Materials Science and Engineering – Committee Chair
Professor Sang Bok Lee, Chemistry and Biochemistry – Dean's Representative
Professor Liangbing Hu, Materials Science and Engineering
Professor John Cumings, Materials Science and Engineering
Professor Bryan Eichhorn, Chemistry and Biochemistry

© Marshall Adam Schroeder

2015

All Rights Reserved

Dedication

To my mother, Deborah Schroeder.

Acknowledgements

I would like to first acknowledge my colleagues in the Rubloff Research Group, past and present, with whom I have had the pleasure to work with since joining the group as an undergraduate work study in the spring of 2009. Chronologically, I must first address special thanks to Dr. Laurent Lecordier for teaching me the difference between Swagelok and VCR, as well as everything I would need to know about vacuum systems. I would like to thank Dr. Xinyi Chen for being a great friend and for exposing me to experimental work as an undergraduate. More recently, I am grateful for the fruitful discussions and support from Dr. Keith Gregorczyk, Alex Pearse, Alex Kozen, Chanyuan Liu, and Chuan-Fu Lin, and I will never forget the countless hours we spent together while assembling the new integrated system.

I will certainly miss working with Dr. Malakhi Noked. It is difficult to express the magnitude of my appreciation for his friendship and mentoring, from coffee brainstorms in the ISR kitchen to his worldly life perspectives. His work ethic is an inspiration and this project would not have been possible without him (especially the TEM and electrochemistry!).

I am indebted to my committee members for their assistance with reviewing this thesis and the guidance they provided throughout this project. Additionally, I would like to thank Dr. Jim O'Connor, Jon Hummel, Tom Loughran, and the rest of staff at the UMD Nanocenter Fablab for their instruction, patience, and advice. The IREAP staff also provided significant support in realizing this project (Nolan Ballew built all of the Li-O₂ test cells) and our state of the art research facility (Jay Pyle, Don Martin, Bryan Quinn).

I would like to address my most sincere gratitude and appreciation to Professor Gary Rubloff, who has been a tremendous role model, instructor, and advisor. Thank you for inspiring me to pursue research as an undergraduate, for encouraging me to try new things, and for always making time for me despite your insanely busy schedule.

None of this would have been possible without the loving support and encouragement from my family throughout this entire journey. This dissertation is proudly dedicated in loving memory to my mother, Deborah Schroeder, who passed away after a fierce battle with lung cancer in 2006.

Finally, I would like to acknowledge the gracious generosity of our funding sources. This work has been supported in part by Nanostructures for Electrical Energy Storage (NEES), an

Energy Frontier Research Center funded by the U.S. Department of Energy, Office of Science, Office of Basic Energy Sciences under award number DESC0001160. I would also like to give special thanks to the John and Maureen Hendricks Charitable Foundation for their extremely generous fellowship which allowed me to the freedom to attempt something completely foreign to my group's research and pursue my fascination with Li-O₂ batteries.

Table of Contents

Dedication	ii
Acknowledgements.....	iii
Table of Contents	v
List of Figures, Schemes, and Tables.....	vii
Chapter 1: Introduction	1
1.1 Motivation for Li-O ₂ Battery Research	1
1.2 History and Fundamentals of Nonaqueous Li-O ₂ Batteries	4
1.3 Problem Statement.....	5
1.3.1 Overpotential and Poor Round-Trip Efficiency	5
1.3.2 Chemical Stability of Carbon Electrodes and Parasitic Side Reactions	7
1.4 Overview of Dissertation	7
1.4.1 Objectives.....	7
1.4.2 Outline and Description of Subprojects.....	8
Chapter 2: Establishing a Platform for Li-O ₂ Battery Research	9
2.1 LAMP Fire and ANSlab Rebuild	9
2.2 Integrated System: Equipment and Capabilities.....	11
2.3 Lithium-Oxygen Test Cells.....	12
2.4 Atomic Layer Deposition (ALD)	14
2.5 Electrochemical Testing	16
Chapter 3: Vertically Aligned Carbon Nanotubes on Ni Foam—A Cathode Discovery Platform for Li-O ₂ Battery Research.....	17
3.1 Cathode Design Considerations	17
3.2 Cathode Development	18
3.3 Characterization of Pristine Structure	21
3.4 Electrochemical Testing	24
3.5 Characterization of Cycled Cathodes	28
3.6 Degradation Mechanism.....	32
3.7 Conclusions	35
Chapter 4: Realization of Rechargeable Li-O ₂ Cathodes with Catalysts Deposited via Atomic Layer Deposition.....	35

4.1	Introduction	35
4.2	Synthesis and Characterization of Pristine Ru-based Cathodes	38
4.3	Electrochemical Characterization	41
4.4	Stable Non-Li ₂ O ₂ Interfacial Layer	45
4.5	Conclusions	51
Chapter 5: Dimethyl Sulfoxide as a Stable Electrolyte Solvent for Li-O ₂ Research		52
5.1	Introduction	52
5.2	Experimental Methods.....	55
	DMSO ₂ as a Marker of DMSO Oxidation.....	55
	Long Term Stability of DMSO Against Oxidation in an Operational Li-O ₂ Cell	57
	Li ₂ O ₂ Decomposition	60
5.3	Density Functional Theory Study of DMSO/Li ₂ O ₂ Interfacial Stability	63
5.4	Discussion.....	67
5.5	Conclusions	71
Chapter 6: Investigating the Interplay of ALD Defect Passivation and Catalysis for Practical Secondary Li-O ₂ Cathodes		72
6.1	Introduction	72
6.2	Approach.....	74
6.3	Results and Discussion	74
6.4	Conclusions	79
6.5	Future Work.....	80
6.6	Closing Perspectives.....	81
Chapter 7: Appendix		83
7.1	Experimental Methods.....	83
7.2	Hendricks Energy Research Fellowship Proposal.....	89
References		92

List of Figures, Schemes, and Tables

Figure 1: Energy density projections of theoretical Li-O ₂ cell configurations as compared to current and future Li-ion systems. ^[115]	3
Table I: Mass and volume-specific energy densities of battery technologies across a range of maturity ^[3]	3
Figure 3: Schematic of a Li-O ₂ battery during discharge showing O ₂ reduction at cathode and oxidation of lithium metal at the anode. ^[9]	4
Figure 2: Discharge profile of the Li/C pouch cell used in the IR gas sampling experiment. ^[6]	4
Scheme 1: Discharge (ORR) and charge (OER) processes in a Li-O ₂ battery	5
Figure 4: Schematic of a typical Li-O ₂ cycle profile. ^[106]	6
Figure 5: 1 st generation integrated high vacuum system in lab for advanced materials processing (LAMP in J.M. Patterson building)	9
Figure 7: Final floor plan for new ALD Nanostructures Laboratory (ANSLab) and picture of the new lab setup.	10
Figure 6: LAMP lab on the evening of the fire.	10
Figure 8: Specialized Li-O ₂ coin cell.....	13
Figure 9: 1 st generation sealed O ₂ chamber with electrical feedthrough for Li-O ₂ coin cell testing.	13
Figure 10: Schematic of cell design used by many of the leading lithium oxygen research groups which allows for non-destructive testing and characterization of battery components.....	13
Figure 11: Schematic of an atomic layer deposition process starting with a pristine substrate and showing the process sequence for self-limited growth of each monolayer of the compound.....	15
Figure 12: The electrochemical workstations used for Li-O ₂ research. a) The <i>BioLogic</i> VSP potentiostat/galvanostat b) The <i>Arbin</i> BT2000 battery test station.	16
Figure 13: 5/8" nickel foam disc as a growth substrate for CVD (left), low magnification SEM image of nickel foam structure (center), and TEM image of nickel foam surface morphology (right).	18
Figure 14: Process flow for chemical vapor deposition of vertically aligned carbon nanotubes on nickel foam.....	19
Figure 15: SEM images of vertically aligned carbon nanotubes grown on nickel foam. These images illustrate the desired dual pore hierarchical structure with mesoporous voidspace between the VACNT and macropores preserved by the underlying Ni foam.....	21
Table II: Growth parameters for low pressure chemical vapor deposition (LPCVD) reactor during successful VACNT growth processes on nickel foam, as confirmed by SEM characterization. All growth substrates were nickel foam with 5nm Al ₂ O ₃ underlayer and 7.5Å Fe,.....	22
Figure 16: TEM and electron diffraction of the growth showing that the vertically aligned carbon structures are in fact, nanotubes with ~10 walls (left). STEM showing Fe CVD catalyst embedded in the base of the VACNT, suggesting a “base-growth” mechanism.	23
Figure 17: XPS Survey spectrum of the pristine cathode structure showing the only elements present are carbon and a small amount of oxygen.....	23
Figure 18: High-res C 1s spectrum of the as-grown cathode.....	24
Figure 19: Electrochemical performance of the VACNT-Ni electrode architecture as a Li-O ₂ cathode with 0.1M LiClO ₄ in DMSO, DME, and Diglyme-based electrolytes. A) Cyclic voltammetry plot of the cathodic	

peak (indicative of ORR behavior) showing the most favorable onset potential for ORR in DMSO. B) Galvanostatic discharge at 20 μ A (cell current) showing superior discharge behavior in the DMSO-based electrolyte. C) Chronoamperometry measurements at different voltages in 0.1M LiClO₄ in DMSO. D) Galvanostatic discharge @20 μ A cell current of electrode structures with two different ALD interlayers.25

Figure 21: Comparison of select cycle profiles from the DMSO-cell in Figure 20. 27

Figure 20: Galvanostatic cycle profile comparison of VACNT-Ni foam electrode architecture operated in Li-O₂ cells with two different electrolytes. The DMSO shows slightly better performance, reaching the 22nd discharge without failure and maintaining a consistently higher discharge voltage (~2.75V for DMSO vs. 2.65V for TEGDME) 27

Figure 22: SEM (a,b) and TEM (c,d) images of a cathode galvanostatically discharged to 2V vs. Li/Li⁺ 28

Figure 23: XPS spectra of discharged cathode including survey scan (a) and high resolution scans of (b)O 1s,(c) Li 1s, and(d) C 1s peaks. 29

Figure 24: SEM images of VACNT-Ni cathode after 1st charge. The VACNT tube forests are slightly collapsed but remain intact and a significant amount of the reduction products have been evolved..... 30

Figure 25: VACNT cathode after extended cycling showing delamination of the VACNT from the current collector. This mechanism is suspected to be the cause of the observed performance decline in capacity and discharge voltage. Images a-d are of the cathode cycled in DMSO with e and f showing a similar degradation mode for a cathode cycled in TEGDME-based electrolyte..... 31

Figure 26: Schematic showing the interfaces in the VACNT-Ni cathode architecture as a roadmap for identifying potential failure mechanisms. 32

Figure 27: Schematic outlining the mechanism for degradation of the CNT base that eventually leads to complete fracture and delamination of the tubes from the current collector. The higher concentration of defects and sp³ hybridized carbon at the interface are more susceptible to oxidation by Li-O₂ intermediates and products. 33

Figure 29: SEM of VACNT-Ni cathode after 150 cycles as a Li-S cathode. The VACNT are still in contact with the nickel foam under a thin solid electrolyte interface layer. 34

Figure 28: Galvanostatic cycling performance of VACNT-Ni Li-S cell cycled at two different rates (250mAg⁻¹s and 375mAg⁻¹s)..... 34

Figure 30: CV of MWCNT sponges loaded with ALD catalysts to probe OER/ORR activity. 37

Figure 31: SEM (a) and TEM(c) of the pristine MWCNT sponge cathode shown in (b). TEM images of the sponge after 300 cycles of Ru (d) and RuO₂ (e) ALD. 39

Figure 32: High resolution XPS spectra of the C 1s/ Ru 3d region of the a) pristine, b) RuO₂ functionalized, and c) Ru functionalized MWCNT foam. Red open circles indicate raw data, and blue lines show the fitted envelope. The spectra are normalized to the same arbitrary intensity. The spectrum in (a) is typical of high quality carbon nanotubes. The spectra in (b) and (c) are dominated by signal from the Ru 3d orbital, as its photoelectron cross section is over 15 times larger than that of the C 1s. (b) supports the deposition of nearly pure RuO₂, while (c) shows the deposition of metallic Ru which is covered by a thin native oxide. The “Ru⁴⁺ sat.” peak refers to a conduction band screening final state effect commonly observed in conductive ruthenium oxides.^[116] 40

Figure 33: A) Cyclic voltammetry of bare MWCNT sponge (1st cycle shown) and sponges loaded with 300cyc ALD Ru and 300cyc ALD RuO₂ (fourth CV cycles shown). The scan rate is 0.5mVs⁻¹. B) Comparison

of first galvanostatic charge/discharge profile with a 20 μ A total cell current for sponges loaded with catalyst. Despite little difference in ORR behavior, Ru exhibits significantly lower charge voltage for full capacity recovery. 41

Figure 34: Galvanostatic cycle performance of MWCNT@Ru cathode. A) Overlay of select cycle profiles under capacity and voltage limited conditions (2,130 mAh g⁻¹_{carbon} with a current of 70mA g⁻¹_{carbon}). Profile shows stable cycling until failure during the 25th discharge due to voltage limitation. B) Reclosing the cathode in a new cell resulted in recovery of the cycle profile after the 25th charge, as shown on the right, for up to 40 cycles. C) Cycle profile overlay for cathode cycled at higher current density. D) Discharge capacity for cathode cycled in C is maintained for over 300 cycles..... 43

Figure 35: Mass spectroscopy headspace sampling of MWCNT/Ru cell after 25th discharge (premature cell failure requiring anode replacement). The primary component is O₂ and there are barely detectable levels of CO₂ which in previous works has been used to indicate Li₂CO₃ the presence on the cathode as a result of parasitic side reactions.^[15] The lack of a clear reason for failure encouraged us to replace the anode and resume testing. 44

Figure 35: Survey scans of the first discharge and charge of a Ru functionalized MWCNT cathode. The spectra are normalized so that the C 1s peaks have the same intensity, highlighting the relative change of the O and Li peaks. The peak heights are proportional to the total amount of each element. Inset: C : O : Li atomic ratios calculated using photoelectron cross sections. 46

Figure 36: A systematic comparison of the high resolution C 1s/ Ru 3d (a,b), O 1s (c,d), and Li 1s (e,f) XPS peak regions for the first discharge and charge of a Ru functionalized cathode. All spectra are normalized to the same arbitrary peak intensity to highlight changes in peak shape and location, though the absolute quantities change significantly (Fig 35 inset). Peak locations for (a) and (b) can be found in the text. Some peaks in (b) shift slightly relative to (a), possibly due to small amounts of differential charging. Explicit peak fitting was not attempted for (c), (d), (e), and (f), though locations of possible species are highlighted, with locations based on either measured standards (LiTFSI, Li₂O₂) or literature values (all others).^[85,117,118] 46

Figure 37: High resolution XPS spectra of the (a) Li 1s and (b) O 1s of commercially available Li₂O₂ powder. The spectra are calibrated by placing the C 1s hydrocarbon peak at 284.8 eV. 47

Figure 38: High resolution C 1s / Ru 3d spectrum of a Ru functionalized cathode after the 40th charge cycle (see Figure 34). The charge spectrum from a different cathode after a single charge (Figure 36b) is almost identical. The Ru peaks can no longer be clearly resolved into metallic and oxide components, but the primary Ru 3d j=5/2 intensity centered at 280eV suggests the catalyst is still at least partially metallic..... 48

Figure 39: TEM image of the MWCNT-Ru cathode after the 1st charge (left) and the 40th charge cycle (right) showing the surface film remaining on the cathode with underlying and intact Ru catalyst. 49

Figure 40: TEM image of MWCNT-Ru cathode after 1st discharge showing interfacial layer and the presence of ~1.5nm spherically shaped deposited particles, mainly on the Ru surface. It seems likely that these particles are primarily composed of Li₂O₂ based on the XPS analysis because the only significant difference between the spectra for charged and discharged cathodes can be attributed to the presence of Li₂O₂. Though those deposited species disappear upon charging of the cathode (Figure 39b) the

amorphous SEI stays on its surface without noticeable change in morphology (e.g. or composition as found by XPS) 50

Figure 41: High resolution F 1s and S 2p spectra from a Ru functionalized MWCNT cathode after a single discharge-charge cycle. The F 1s shows a small amount of formed LiF, possibly from TFSI decomposition. This amount of LiF was consistent across essentially all samples tested. The S 2p shows a peak at a slightly lower binding energy than the main TFSI peak, which would nominally be associated with a more reduced sulfur species. This feature is again consistently observed and does not grow after 40 cycles. The S intensity at ~163 eV was a feature observed on all samples loaded into the XPS during a particular time, and has been identified as slight contamination from an unrelated outgassing S loaded sample stored in the same vacuum chamber. 50

Figure 42: Raman spectrum of pristine KO₂ powder (left) showing strong peak at 1142cm⁻¹ which can be attributed to the O=O stretch. KO₂ powder aged in air shows evolution of multiple peaks. 56

Figure 43: FTIR and Raman spectra for limit of detection of mol% DMSO₂ in DMSO. The measured limit of detection is ~0.05 mol% for FTIR and 1% for Raman as indicated by the onset of the symmetric SO₂ stretch at 1142cm⁻¹. 56

Figure 44: Raman spectrum of electrolyte after 14 days of rest within a discharged cell. No signal at 1142 cm⁻¹ suggests oxidation of DMSO is below detection limits or not present. 57

Figure 45: SEM (left) and TEM (right) images of ALD-Pt coated carbon nanotube sponge used as a cathode for extensive cycling to probe DMSO stability over long cycles (80 hrs round trip) 58

Figure 46: Cyclic voltammetry of pristine sponge cathode (1st cycle shown) compared to CNT@Pt cathode (fourth cycle shown). As obtained, the onset potentials for ORR are higher for the catalyst-loaded cathodes, suggesting enhanced activity which agrees well with the report on catalytic trends for ORR.^[61] The more prominent improvement in activity is observed during the oxygen evolution reaction, with significant increases in current obtained at much lower onset potential as compared to the pristine MWCNT. 58

Figure 47: Raman spectrum of electrolyte sample from CNT@Pt showing no detectable levels of DMSO₂ (v_{s, so2}). Shown with 20 mol% DMSO₂ in DMSO for comparison 59

Figure 48: Figure 4. XPS spectra of as-received Li₂O₂ powder (a,c,e) and Li₂O₂ powder immersed in DMSO for over 2 months at room temperature (b,d,f). (a) and (b) compare the C 1s region with peak fitting, and (c) and (d) compare the O 1s region with peak fitting. (e) and (f) show a wide energy region (0- 600eV) which contains the O 1s, C 1s, S 2p, and Li 1s peaks. The numbers next to each peak reflects the calculated atomic percent composition of each sample. The insets show high resolution data from the S 2p regions. The y-scales of all graphs are normalized to approximately the same size to highlight differences in peak shape, except for the insets in (e) and (f) which have the same y-scale to highlight changes in quantity. 60

Figure 49: XRD of Li₂O₂ aged in DMSO for two months showing no indication of decomposition to LiOH or Li₂CO₃. 61

Figure 50: FTIR of Li₂O₂ aged in DMSO for seven months showing no indication of oxidation to DMSO₂. 62

Figure 51: Plot of capacity vs. voltage during linear voltage scan. The blue curve represents a cell that had no rest time between the end of discharge and this charge sweep. The red curve represents a cell that rested for 100 hours before the charge sweep. 62

Figure 52: DMSO adsorbed atop superoxide (left) and peroxide (right) terminated Li ₂ O ₂ surfaces.....	63
Figure 53: The NEB barrier for DMSO decomposition atop superoxide (a) and peroxide (b) terminated Li ₂ O ₂ surfaces. The high precision PBE0 calculation ((■ in (b)) predicts a higher barrier and an exothermicity that is lowered by 0.29eV.....	65
Figure 54: The NEB barrier for DMSO decomposition atop a monolayer of broken DMSO on peroxide terminated Li ₂ O ₂ surface. The H that is abstracted from DMSO and transferred to the broken DMSO fragment is shown with the dashed circle in Image 0 (Frame i).....	66
Scheme 2. Suggested Mechanisms for Oxidation of DMSO: (A) ^[76] , (B) ^[94] , (C) ^[21] , and (D), the mechanism proposed/studied in this work.....	69
Scheme 3. Strategy for optimizing ALD functionalization of MWCNT scaffold as a practical route to long term cyclability.....	73
Figure 55: Galvanostatic cycling profile (300mA g ⁻¹ to 300mA h g ⁻¹) to failure (2V lower limit) for the pristine MWCNT sponge.....	74
Figure 56: TEM image of MWCNT sponge after accelerated GV cycling test showing loss of crystallinity.....	75
Figure 57: Galvanostatic cycling profile (300mA g ⁻¹ to 300mA h g ⁻¹) of MWCNT sponge coated with two different thicknesses of ALD TiO ₂ . Despite a similar number of total cycles to failure (CtF), the cathode with the thinner TiO ₂ layer exhibited slightly longer charge durations.....	75
Figure 58: TEM image showing 100 cycles (~5nm) core-shell coating of ALD TiO ₂ on MWCNT.	76
Figure 59: TEM images of 75 cycles of ALD Pt on pristine MWCNT sponge (left) and a 5nm MWCNT@TiO ₂ core shell.....	77
Figure 60: Galvanostatic cycling data under accelerated testing conditions (100mA g ⁻¹ to 300mA h g ⁻¹) of TiO ₂ @Pt core shell cathodes with two different TiO ₂ interlayer thicknesses (~5nm and 20nm). This data shows a slight enhancement in reversibility of the thinner TiO ₂ layer. Both curves show a 5X improvement in cyclability as compared to MWCNT@TiO ₂ and a 25X improvement as compared to the pristine sponge.....	77
Figure 61: Profile of 1 st discharge and charge under the accelerated galvanostatic cycling conditions. All cathodes discharge to the full capacity but there is a large discrepancy in charge capacity under the 4V upper limit as a result of the different surface functionalizations.	78
Figure 62: TEM image of MWCNT@TiO ₂ @Pt MWCNT double core shell structure with reduced ALD cycle counts (25 Pt and 40TiO ₂) showing a conformal but thinner shell.....	79
Figure 63: Galvanostatic cycling of cathodes with reduced Pt and TiO ₂ loading. 25 ALD cycles of Pt shows a 3x improvement over the MWCNT@TiO ₂ in Figure 57 and 75 cycles shows a significant improvement over the analogous structure with 100TiO ₂ (Figure 60).	79

Chapter 1: Introduction

1.1 Motivation for Li-O2 Battery Research

The International Energy Agency (IEA) projects that the world's primary energy demand will increase by 37% by 2040.^[1] The power sector represents over half of this increase in global primary energy use, a surge comparable to the current total energy demand in North America.^[1] Fossil fuels play a vital role in the world energy landscape with coal and natural gas as the principal energy sources for power generation, and oil fueling the transportation infrastructure; however, there are major consequences of such a heavy dependence on the world's finite carbon fuel reservoir. An uneven worldwide distribution of these fuels has led to significant geopolitical tension, and within the foreseeable future, fuel production will eventually be eclipsed by consumption, further intensifying the problem. Further cause for concern is the projected increase in CO₂ emissions by 20% by 2040^[1], which will set the world on a path toward long-term global temperature increases and the associated but uncertain ramifications.

The clear but challenging solution to this problem is the aggressive adoption of renewable sources of energy, including solar, hydro, wind, biomass, and geothermal. These renewable sources are unlimited and generally untapped means of energy generation with minimal pollution or global warming emissions. Renewable energy modes generally require completely different infrastructures for generating electricity and have been the focus of extensive research and development but have yet to realize widespread implementation due to limitations in geographic and temporal availability. These limitations bring into question the reliability of an electric grid that would draw a significant portion of its power from sources with variable generation, but these setbacks can be overcome by coupling renewable energy systems with appropriate energy storage schemes.

In terms of energy storage for electric grid applications, there are three classes based on the expected discharge duration: storage technologies for power quality applications with ~10 min discharge time (flywheels, capacitors, superconducting magnetic energy storage), bridging power with discharge durations of ~1 hour (high power batteries), and energy management schemes with discharge times of several hours or more (Pumped hydro, compressed air, thermal energy storage, and high capacity batteries).^[2] Batteries are a particularly adaptable energy storage scheme due to portability, scalability, and versatility in deliverable power and energy density based on the chemistry.

Batteries will also play a major role in enabling a shift toward electrification of the transportation sector, further reducing dependence on geopolitically sensitive, emission-producing fossil fuels and providing an environmentally friendly, lower cost alternative to combustion powered vehicles in the long term if coupled to clean, domestic sources of electricity.

Indeed, commercially available battery technologies have already seen initial implementation (Pb-acid, Ni-Cd, Ni-MH, Li-ion, and Na-S) in grid storage and electric vehicles (Li-ion, Ni-MH, Pb-acid), but there are multiple chemistries still in the development phase that offer significantly enhanced theoretical performance ceilings, potentially paving the way for long term application. One of these most promising next generation battery technologies is the Li-O₂ battery.

With a theoretical specific energy density of 3,458 Wh kg⁻¹ and 4,170 Wh L⁻¹, the Li-O₂ system stands at the pinnacle of a research shift toward high risk, high reward battery chemistries including high voltage Li-ion cathodes such as LiNi_{1/3}Mn_{1/3}Co_{1/3}O₂ (LMRNC), metal-molecule electrochemical redox couples like Li-S, and other metal-air chemistries.^[3] **Figure 1**

shows the projected practical energy density of multiple Li-O₂ cell configurations as compared to the battery packs currently used in commercially available electric vehicles (e.g. Nissan Leaf, Tesla Model S), showing the possibility of a 5x improvement in specific energy (vehicle driving range). **Table I**^[3] compares these calculated theoretical values to a variety of other battery technologies at different stages of developmental maturity and the relative promise this technology offers pending successful optimization is clear.

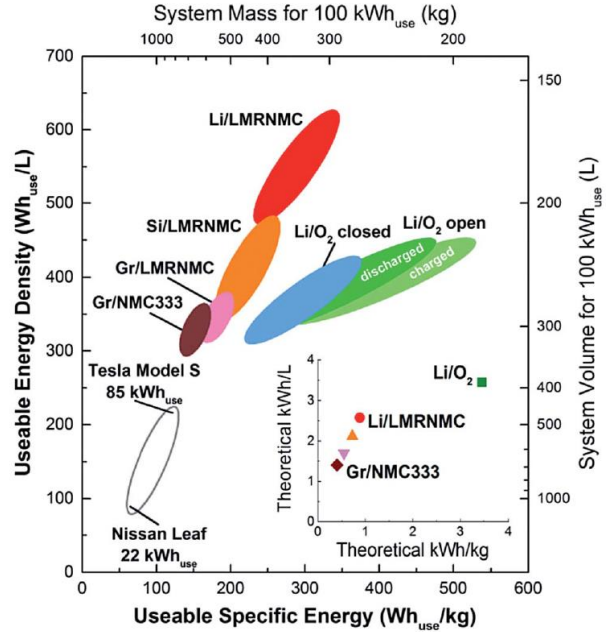


Figure 1: Energy density projections of theoretical Li-O₂ cell configurations as compared to current and future Li-ion systems.^[115]

Despite the excellent theoretical metrics previously mentioned, currently achievable practical values are significantly lower. In order for Li-O₂ batteries to play an active role in the future energy storage landscape, a variety of technical issues in each component of the device (cathode, anode, separator, and electrolyte) must be addressed. A detailed study of the system presents even more challenges, including lackluster round-trip efficiency and poor cycling stability. Fortunately, this system has recently been the subject of significant research attention and the next section will take a look at its history, some of the recent advances, and outline

Table I: Mass and volume-specific energy densities of battery technologies across a range of maturity^[3]

System	Gravimetric ED (Wh kg ⁻¹)		Volume-Specific ED (Wh L ⁻¹)	
	Calculated	Practical	Calculated	Practical
Li/O ₂	3,458	?*	6,170	?*
Li/S	2,566	350	4,260	350
Zn/air	1,086	180	6,091	208
C/LiCoO ₂	387	100	1,015	150
M-H/NiOOH	180	63		142
Pb/PbO ₂	171	60.6	370	108

the challenges addressed in the context of this dissertation.

1.2 History and Fundamentals of Nonaqueous Li-O₂ Batteries

The Li-O₂ battery concept was originally proposed by Littauer and Tsai in 1974 with the use of an aqueous alkaline electrolyte.^[4,5] A little over 20 years later, Abraham and Jiang discovered the nonaqueous lithium air battery while

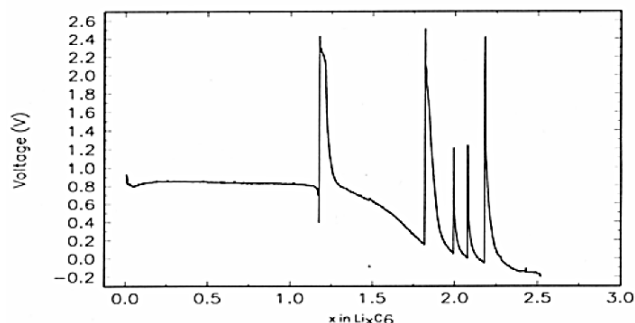


Figure 2: Discharge profile of the Li/C pouch cell used in the IR gas sampling experiment.^[6]

studying Li intercalation behavior of graphite in a Li/C cell with gel-polymer electrolyte.^[6,7] By inadvertently introducing small amounts oxygen while sampling the gas phase headspace for IR studies, the resumed discharge behavior would briefly yield capacity at ~2.3V, as shown in **Figure 2**. They later used these preliminary results to build and patent^[8] the first practical nonaqueous Li-O₂ battery.^[6] Due to significantly reduced theoretical metrics, major issues with anode stability and limitations in rechargeability with aqueous electrolytes, the non-aqueous system will be the focus of this work.

The nonaqueous Li-O₂ battery conventionally consists of a porous carbon positive electrode scaffold designed to promote oxygen diffusion and reduction, an organic Li-ion conducting electrolyte, and a pure lithium metal anode, as shown in **Figure 3**.^[9] During discharge, lithium metal is oxidized at the anode, generating an external

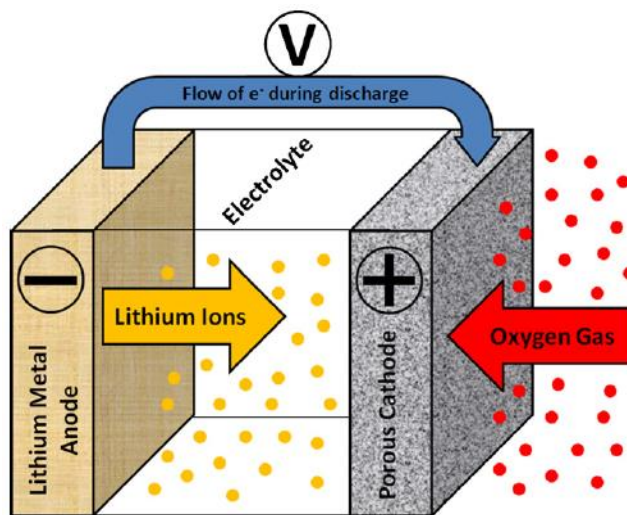


Figure 3: Schematic of a Li-O₂ battery during discharge showing O₂ reduction at cathode and oxidation of lithium metal at the anode.^[9]

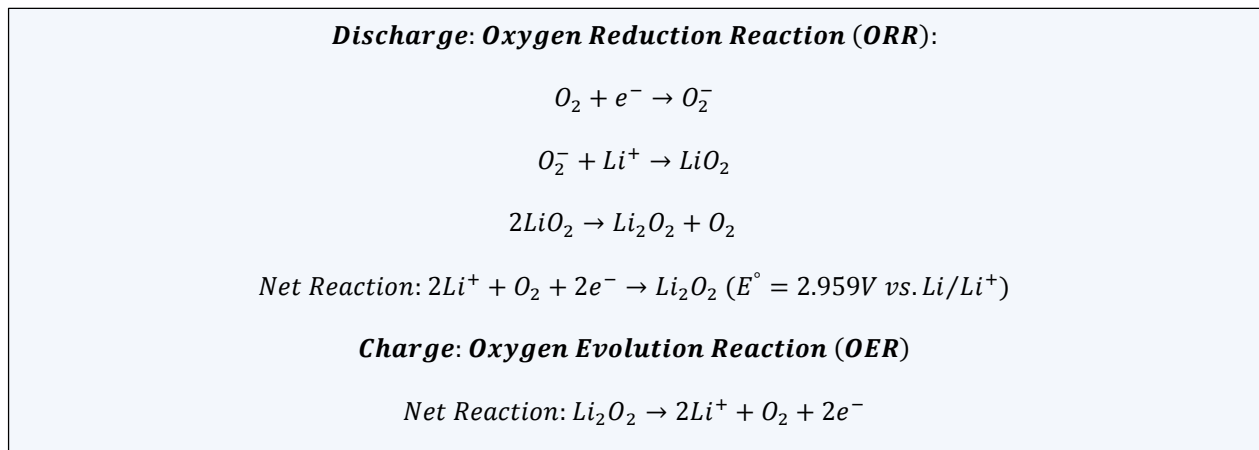
electron current as the dissociated lithium ions flow through the electrolyte with the electrochemical potential gradient to the cathode. Upon meeting the cathode surface, the lithium is reduced with dissolved oxygen in the electrolyte, forming Li_2O_2 on the cathode surface in a process known as the oxygen reduction reaction (ORR). During subsequent charging, this process is reversed, as Li_2O_2 is electrochemically dissociated to evolve oxygen gas and Li^+ , a process known as the oxygen evolution reaction (OER). Many non-idealities in these electrochemical processes at the positive electrode surface diminish the performance of this system, as outlined in the following section.

1.3 Problem Statement

1.3.1 Overpotential and Poor Round-Trip Efficiency

As introduced briefly in the previous section, the secondary, nonaqueous Li- O_2 system is characterized by two net reactions shown in **Scheme 1**. The consensus from various studies^[10–13] is that the oxygen reduction mechanism involves formation of O_2^- as an intermediate, while the charge process occurs directly without requiring formation of an intermediate.^[14] **Figure 4** shows a practical cycle profile for a Li- O_2 cell with a dashed line showing the standard potential for the discharge reaction, $U_0=2.96\text{V}$ vs. Li/Li^+ , as calculated by the Nernst equation. A characteristic

Scheme 1: Discharge (ORR) and charge (OER) processes in a Li- O_2 battery



drop (~250mV) in the operating voltage from the theoretical ORR value is observed in practical Li-O₂ systems as a result of three experimental factors: Ohmic losses, activation polarization (charge transfer resistance), and concentration polarization (mass transfer resistance). The Ohmic losses are attributed to the electronic resistivities of

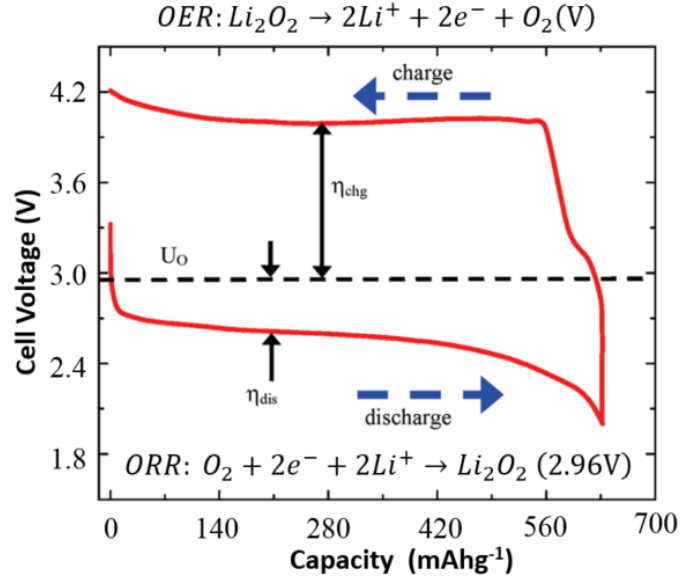


Figure 4: Schematic of a typical Li-O₂ cycle profile.^[106]

the lithium and carbon electrodes, and the ionic resistivity of the nonaqueous electrolyte. Non-idealities associated with activation polarization are kinetic bottlenecks related to charge transfer processes (oxidation and reduction) occurring at the surfaces of both electrodes. Finally, voltage loss associated with the concentration polarization occurs as a result of local reactant depletion over time, essentially starving the reactions. The effects of each of these limitations increase with current density, meaning that the power density of Li-O₂ batteries hinges on addressing bottlenecks in generation and transport of active species. A significantly higher voltage is required to reverse this process, typically requiring $E_{OER} > 4V$ vs. Li/Li⁺ before full capacity recovery. The area within the red curve is essentially wasted energy, and this behavior is a major barrier to commercialization. Thus, one of the key challenges to realizing a practical Li-O₂ system is finding a way to reduce cell overpotentials during discharge and charge (η_{dis} and η_{chg} , respectively).

1.3.2 Chemical Stability of Carbon Electrodes and Parasitic Side Reactions

The most important characteristics of an O₂ cathode scaffold are high surface area, good electronic conductivity, and chemical stability in the presence of the electrolyte, reaction intermediates, and products. Carbon possesses many of these qualities, and its affordability and natural abundance make it an ideal material for commercialization. As a result, myriad variants of carbon (both allotropes and morphologies) have been tested as the positive electrode in Li-O₂ batteries. Several studies have examined the stability of these electrodes in operating cells and observed side reactions at the cathode as a result of carbon decomposition.^[15-19] While carbon is chemically stable in static systems and electrochemically stable below 3.5 V vs. Li/Li⁺ during discharge and charge, oxidative decomposition to lithium carbonate and carboxylates is observed upon charging above 3.5 V in the presence of Li₂O₂.^[19] The products of these side reactions are not completely oxidized during subsequent charging, leading to accumulation throughout cycling and associated electrode passivation and capacity fading. Interestingly, the extent and rate of carbon degradation is greater for hydrophilic carbon electrodes which is attributed to higher densities of C-O, COOH, and C-OH intrinsic surface defects.^[19]

1.4 Overview of Dissertation

1.4.1 Objectives

1. Develop and test atomic layer deposition chemistries for OER/ORR catalysis to reduce cell OER/ORR overpotentials, thus improving round trip energy efficiency.
2. Experiment with electrochemically inactive ALD protection layers as a mode of defect passivation in carbon cathode substrates to deter parasitic side reactions and improve long term cycle stability.

3. Design cathode-catalyst architectures, enabled by ALD, that allow for performance optimization with optimal materials utilization. This focuses on the cooperation between cathode protection and catalysis, with an emphasis on attempting to reduce the required loading of noble metal catalysts, and/or improving loading efficiency per process.

1.4.2 Outline and Description of Subprojects

For organizational purposes, the following subprojects will be addressed in the coming chapters as outlined, below:

Chapter 2: Development of a lab-scale infrastructure for assembly, electrochemical testing and characterization of Li-O₂ battery cathodes including a custom test cell and state of the art integrated system.

Chapter 3: Design, fabrication, and testing of a unique 3D cathode architecture of vertically aligned carbon nanotubes on an integrated nickel foam current collector as a discovery platform for studying performance and degradation Li-O₂ battery cathodes.

Chapter 4: Assessment of the chemical and electrochemical stability of dimethyl sulfoxide (DMSO) as a suitable electrolyte solvent for Li-O₂ battery research and development.

Chapter 5: Creation of a Li-O₂ cathode architecture that exhibits exceptional long term cycling stability via atomic layer deposition of ruthenium and ruthenium oxide heterogeneous catalysts on a multi-walled carbon nanotube sponge

Chapter 6: Interplay between carbon defect passivation vs. heterogeneous catalysis as modes of improving operational stability of Li-O₂ cathodes with atomic layer deposition.

Chapter 2: Establishing a Platform for Li-O₂ Battery Research

2.1 LAMP Fire and ANSlab Rebuild

The first generation of our integrated vacuum system which was located in the lab for advanced materials processing (LAMP) in the J.M. Patterson building is shown in Figure 5. This system featured a Leybold-Heraeus X-ray photoelectron spectrometer (XPS), which I assisted in refurbishing as an undergraduate, coupled to an aluminum evaporator and a FIJI F200 atomic layer

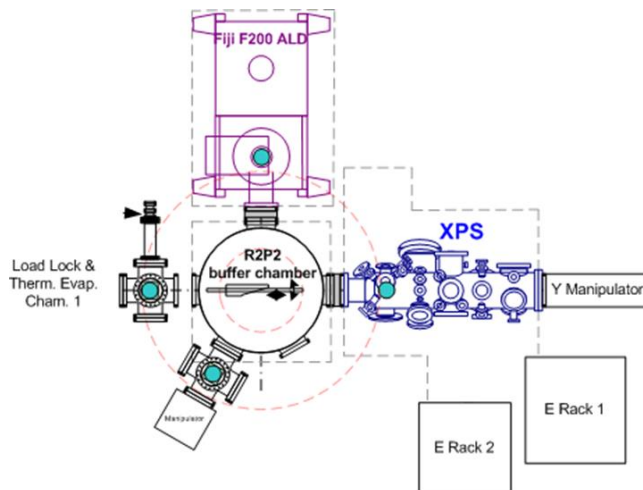


Figure 5: 1st generation integrated high vacuum system in lab for advanced materials processing (LAMP in J.M. Patterson building)

deposition system with a manual rotary feedthrough vacuum chamber. After receiving the John and Maureen Hendricks Energy Research Fellowship to study Li-O₂ batteries there was a brief period in early January 2012 when we considered adding a glove box to this system, but those plans were quickly postponed as a result of a lab fire.

On Monday January 16th, 2012, a HEPA filter fan motor in the ceiling of our LAMP lab cleanroom failed, causing an electrical fire and ensuing smoke and water damage to all of our equipment inside, as shown in **Figure 6**. With damages exceeding \$2.5 million and loss of all three atomic layer deposition systems, the probe station used for electrical characterization, the ellipsometer, the x-ray photoelectron spectrometer and a few other tools, research came to an abrupt halt. We had no choice but to rebuild the lab from the ground up.

We spent the next two years developing a new lab arrangement in a larger workspace in the Institute for Research in Electronics and Applied Physics (IREAP). We first researched and ordered new replacement equipment after comparing device specifications offered by different manufacturers. The subsequent lead time for equipment delivery was spent installing gas delivery lines, mapping out electrical needs for installation of new outlets, building an exhaust system and a water cooling infrastructure, and drawing potential floor plans.

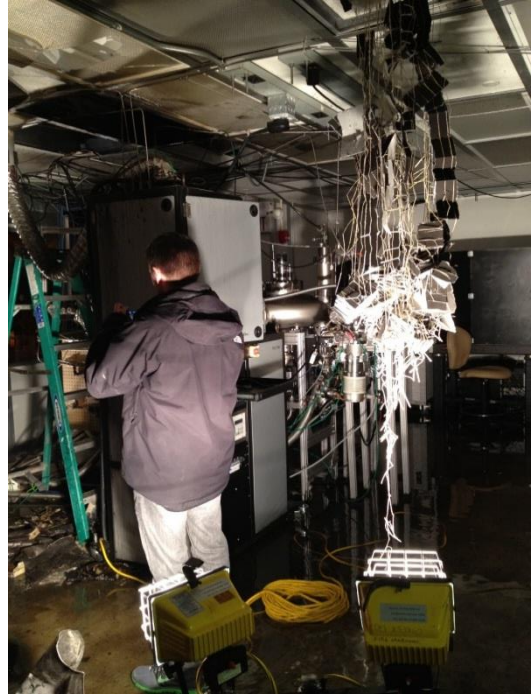


Figure 6: LAMP lab on the evening of the fire.

Design and assembly of this lab/system has been an invaluable and unique learning experience that was well worth the cost in research time. The equipment featured in this state of the art integrated characterization and processing facility (**Figure 7**) will be discussed in detail in the next section.

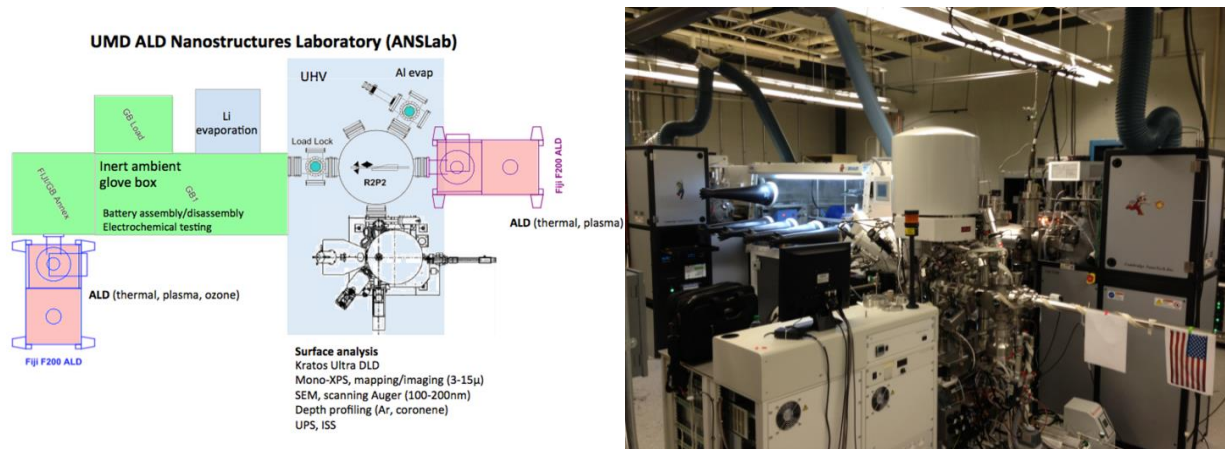


Figure 7: Final floor plan for new ALD Nanostructures Laboratory (ANSLab) and picture of the new lab setup.

2.2 Integrated System: Equipment and Capabilities

Working from left to right across the schematic in Figure 7, the first piece of equipment is the newer of the two Ultratech FIJI F200 atomic layer deposition (ALD) systems, and is known as “Luigi”. This system has been outfitted with a variety of chemistries (Al_2O_3 , TiO_2 , TiN , MnO_x , Pt, Cu, SnO_2 , etc.) and is the lab workhorse with a 12” sample chuck allowing for high throughput. “Luigi” offers the most versatility in terms of process types including thermal ($T < 500\text{ }^\circ\text{C}$), plasma-enhanced (remote inductively coupled 300W RF plasma generator), and ozone-based atomic layer deposition, and the platinum ALD referenced in this work was performed in this reactor. This ALD tool is directly coupled with a custom annex to a 7-glove Ar-filled MBraun Labmaster glovebox. This annex allows for both external sample loading and direct transfer from the glovebox (an important capability for post-growth characterization without air exposure). The glovebox is customized with multiple 8” conflate port attachments for direct integration with other vacuum systems attachments. The first of these attachments is a chamber equipped with an effusion cell for thermal evaporation of lithium metal (and a quartz crystal monitor for tracking deposition rate), providing a cleaner, thin film alternative to the lithium ribbon used in most battery experiments. A load-lock chamber mounted on the side conflat port connects the glovebox to the rest of the system and holds a custom carousel for sample storage and transfer. This is coupled to the replacement rotary feedthrough chamber, featuring *Kurt J. Lesker Company*’s radial telescopic transfer robot arm, which acts as the main transfer hub for the entire integrated system. Clockwise from top to bottom, the remaining attachments include a load-lock chamber, the refurbished Ultratech FIJI F200, and a new Kratos surface analysis system. The load-lock chamber is equipped with an aluminum effusion cell for thermal evaporation and a quartz crystal monitor for tracking deposition rate. The original FIJI

F200 has been dedicated to atomic layer deposition Li-containing thin films (Li_2O , LiOH , Li_2CO_3 , Li_3PO_4 , and others). Both of these ALD systems are equipped with viewports for in-situ ellipsometry and downstream mass spectroscopy sampling which are extremely powerful tools for process development and in-situ growth characterization.

The final component of the integrated system is its crowning jewel, the *Kratos* AXIS Ultra DLD surface analysis platform. This spectrometer is outfitted for a variety of powerful techniques, including x-ray and ultraviolet photoelectron spectroscopy (XPS/UPS), x-ray imaging and mapping, scanning Auger microscopy (SAM), and scanning electron microscopy (SEM). Additional components that are extremely useful include an Ar^+ /Coronene/ He^+ ion source for depth profiling and ion scattering spectroscopy (ISS), a monochromated Ag/Al XPS source, and a charge neutralization system for characterizing insulating materials. All of the XPS measurements discussed in this work were collected with this system.

2.3 Lithium-Oxygen Test Cells

Unlike conventional battery chemistries, lithium oxygen test cells require unique designs that allow for oxygen access to the cathode. Due to a previously established infrastructure for handling coin cells, we initially adopted specialized coin cells with a stainless steel mesh positive case for oxygen access, as shown in **Figure 8**. The size and nature of our electrodes resulted in cells that were frequently shorted, and the cases also caused irreversible damage to the electrode materials after crimping. These cells also required an externally sealed container (**Figure 9**) filled with O_2 as the cell itself could not be sealed. All of these difficulties encouraged consideration of alternative options.

We then adopted a much more versatile and non-destructive cell design based on those used by many of the leading Li-O₂ research groups^[20–22], as shown in **Figure 10**. This design is composed of two stainless steel



Figure 8: Specialized Li-O₂ coin cell

current collectors separated by a polychlorotrifluoroethylene (PCTFE) annulus. This material has much lower gas permeability and higher hardness than virgin polytetrafluoroethylene (PTFE), ensuring an uncontaminated system

even during extended cycling studies .^[20] Virgin PTFE O-rings ensure gas-tight sealing at the annulus-

current collector interface. The bottom current collector has concentric insets for the lithium metal anode and wetted separators, respectively. The top current collector has a gas inlet and outlet ports with ball-valves for leak-proof

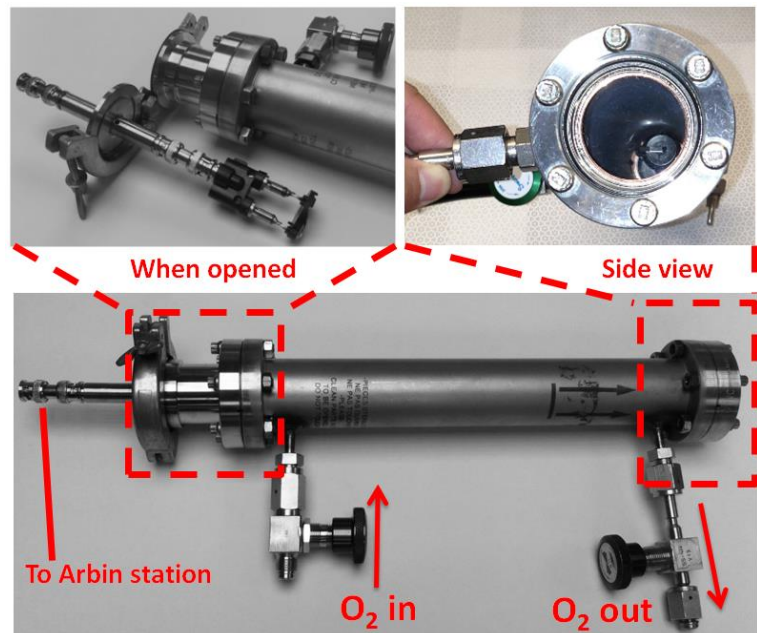


Figure 9: 1st generation sealed O₂ chamber with electrical feedthrough for Li-O₂ coin cell testing.

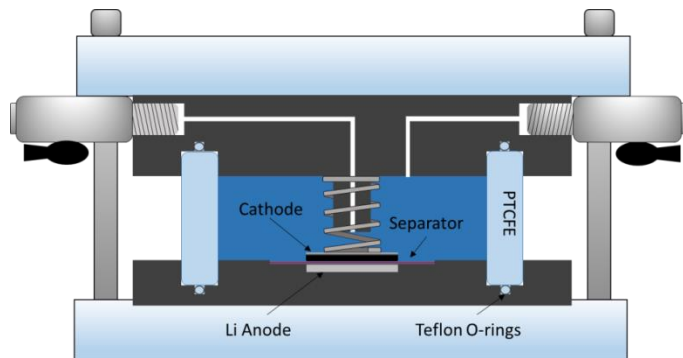
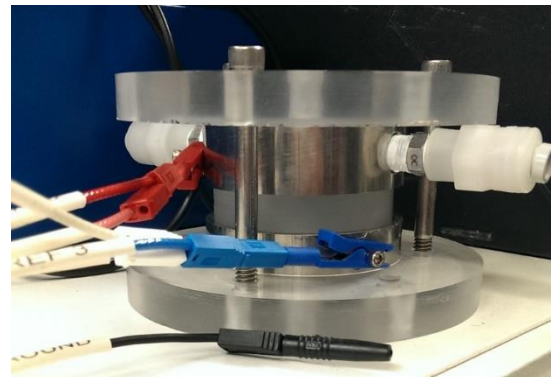


Figure 10: Schematic of cell design used by many of the leading lithium oxygen research groups which allows for non-destructive testing and characterization of battery components.



sealing after filling the cell with O₂ for cycling or purging with Ar for reloading in the glovebox. Electrical contact is made internally with the top current collector by a mounted 316SS spring, as shown in Figure 10. After assembly of cell components, the cell is clamped externally by two polypropylene discs and six 2 3/4" socket head screws.

This cell is extremely useful for studying Li-O₂ batteries and a great match for our integrated system because of the ability to non-destructively disassemble the device at any point during electrochemical testing for characterization of cell components. If desired, the cell can then be reclosed following the measurement for further electrochemistry. It can also be functionalized for other purposes easily. Two of the modifications we have experimented with include in-situ sampling of the headspace for mass spectroscopy (performed in this dissertation as a failure diagnostic) and addition of an IR-transparent spinel-glass window in the bottom current collector for *in-situ* and *in-operando* vibrational spectroscopy.

2.4 Atomic Layer Deposition (ALD)

Introduced as atomic layer epitaxy (ALE) in 1977 by Suntola and Antson as a method^[23] of epitaxially growing thin film compounds, this technique evolved as precursors were developed for a variety of metals and metal oxides, ultimately adopting the name of atomic layer deposition (ALD) as applications progressed. ALD is a gas-phase deposition technique in which sequential pulses of vaporized precursors drive self-limited surface reactions. As a result of this mechanism, ALD offers Angstrom-level thickness control, tunable film composition as a function of process parameters, and remarkable conformality, particularly on high aspect ratio nanostructures.^[24,25] These strengths in concert with a shift toward processing of complex nanoscale device architectures has driven the emergence of ALD in a variety of research

applications and is fueling development of commercial systems for batch and roll-to-roll processing.^[26]

These processes are generally performed under vacuum to keep the reactants and products mobile while maintaining a clean chamber environment, though some success with atmospheric pressure atomic layer deposition has been demonstrated.^[25] Unlike chemical vapor deposition processes which generally require higher temperatures, the window for ALD processes is more modest (<350°C).^[26] While ALD can be used to coat a variety of substrate materials, the commonly used precursor chemistries generally grow most effectively on oxide surfaces with hydroxyl terminations. A schematic of the idealized ALD process flow is shown in **Figure 11**. Initially, a substrate is loaded into the vacuum chamber and is heated to the respective process temperature. The process is initiated by a pulse of reactant A, which is typically an organometallic material containing the metal atom of the ultimately desired metal or metal oxide

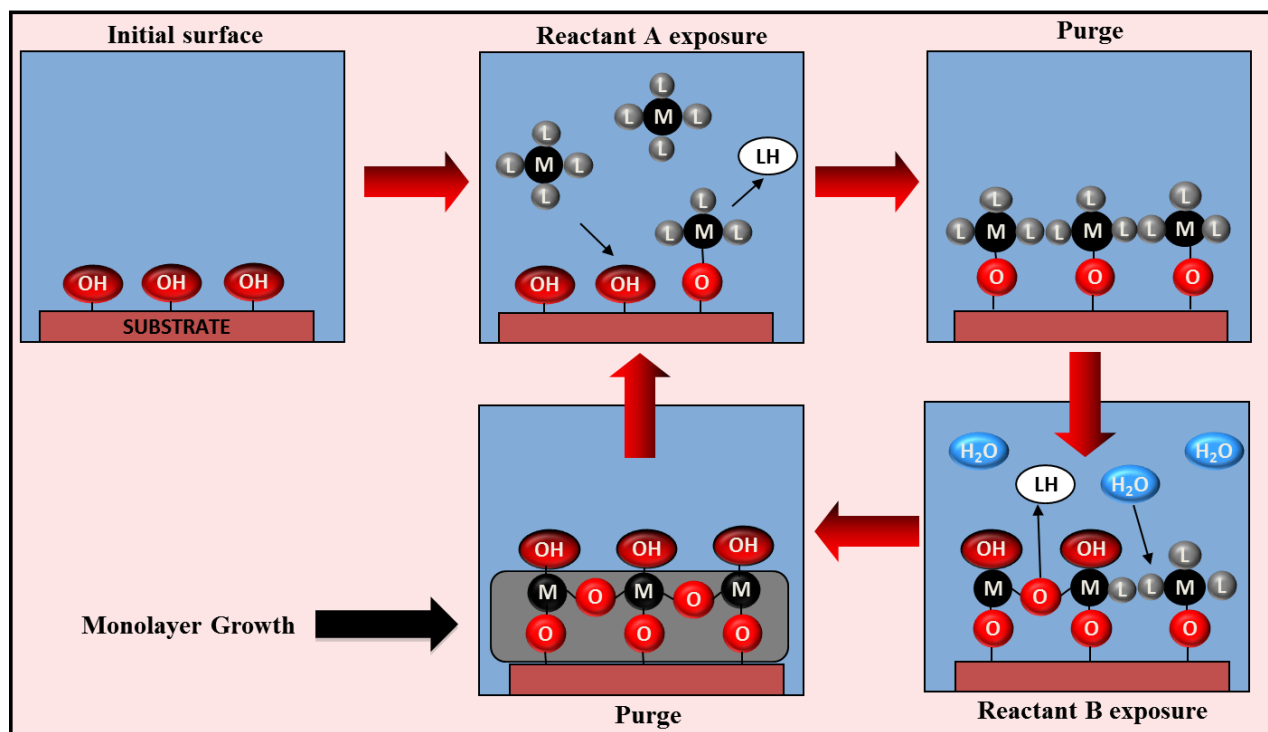


Figure 11: Schematic of an atomic layer deposition process starting with a pristine substrate and showing the process sequence for self-limited growth of each monolayer of the compound.

film (designated as ML₄ in Figure 11). This precursor is chemisorbed on the surface where it reacts with the surface termination (e.g. -OH), producing non-reactive byproducts (e.g. CH₄) that are pumped away with inert gas flow during the subsequent purge step. In an ideal process, the precursor dose is saturated to the extent that the surface has a complete monolayer of reactant A chemisorbed to the surface after this pulse step. Following the first purge step, Reactant B, which is conventionally an oxidant (H₂O, O₂ plasma, O₃), is pulsed and chemisorbed to the surface, again producing byproducts that are pumped away in the subsequent purge. Ideally after this second purge, a single, complete monolayer of the desired compound (M_xO_y) will coat the surface. This cycle process is further repeated, as needed, to achieve the desired film thickness.

2.5 Electrochemical Testing

Electrochemical characterization is the keystone of investigating performance of energy storage systems. For all of the testing performed in this work, two systems were used: a Biologic VSP and an Arbin BT2000 battery test station, as shown in **Figure 12**. All cyclic voltammetry and chronopotentiometry measurements performed in this project used the *Biologic* and the *Arbin* was generally used for long term cycling studies. A two electrode configuration was used for all measurements unless otherwise noted.

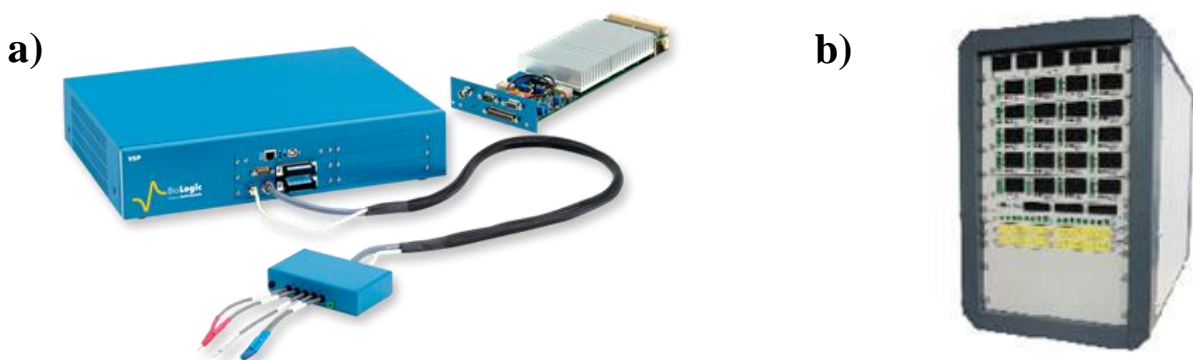


Figure 12: The electrochemical workstations used for Li-O₂ research. a) The *BioLogic* VSP potentiostat/galvanostat b) The *Arbin* BT2000 battery test station.

Chapter 3: Vertically Aligned Carbon Nanotubes on Ni Foam—A Cathode Discovery Platform for Li-O₂ Battery Research

3.1 Cathode Design Considerations

With an infrastructure in place for Li-O₂ research, the next step was to select or develop a cathode platform to start exploring the intricacies of Li-O₂ battery performance and the enhancements that could be achieved with atomic layer deposition. Despite widespread use as the basis of porous cathodes for Li-O₂ cells, issues with the stability of carbon and its known role in electrolyte decomposition brought into question whether it was an appropriate choice as the principal cathode material. Indeed, carbon exhibits many material properties that are favorable for an O₂ cathode scaffold including good electronic conductivity, high surface area, it is lightweight, shows some activity toward the oxygen reduction reaction (ORR)^[27,28], and exists in a wide variety of architectures and morphologies. Other appealing factors for commercialization include its low cost, worldwide abundance, and processing flexibility. Thus, if the stability and electrolyte interaction of a carbon system was a manageable concern, it would be the ideal system for our studies. Fortunately, recent studies indicated that carbon materials that are hydrophobic with a low intrinsic density of functional groups (C-O, COOH, C-OH) and defects demonstrate healthy stability.^[19,29] Thus, the candidate list was further narrowed to graphene, carbon nanotubes, and other sp² based carbon systems without requiring the use of a binder such as PVDF, which has been shown to participate in parasitic side reactions.^[17]

The carbon scaffold-current collector interface is another important consideration in these electrodes due to the fact that Li₂O₂, the expected reduction product in these batteries, is a wide bandgap insulator in bulk form.^[30–33] This has major implications regarding the charge transfer resistance and associated interfacial voltage drop (further contributing to the overpotential in

these batteries) if the quality of the electrical contact is poor. This suggests efforts toward integration of the current collector with the active material will improve device performance.

Based on the operating mechanism of Li-O₂ batteries, which involves the three phase reaction of Li⁺, O₂, and e⁻ on the cathode scaffold in an aprotic environment, there are also important structural considerations that must be taken into account for optimal design performance of the positive electrode scaffold. Because Li₂O₂ is insoluble in nonaqueous electrolytes, it will accumulate according to the depth of discharge. Therefore energy performance enhancement of cathode materials is linked to maximizing the surface area and accommodating a substantial amount of Li₂O₂ without blocking the cathode pore orifices, which could ultimately reduce or completely compromise transport of Li⁺ and oxygen.^[34] Maximizing energy density is thus clearly connected to efficient design of the cathode pore structure, as suggested by modeling of dual-pore systems featuring one pore system dedicated to product storage (mesopores-storage) and a second pore system (macropores-venting) for preserving active species transport.^[34-37]

3.2 Cathode Development

With the previously mentioned design considerations in mind, we selected a nickel foam (MTI Corporation, see **Figure 13**) current collector as a chemical vapor deposition (CVD)

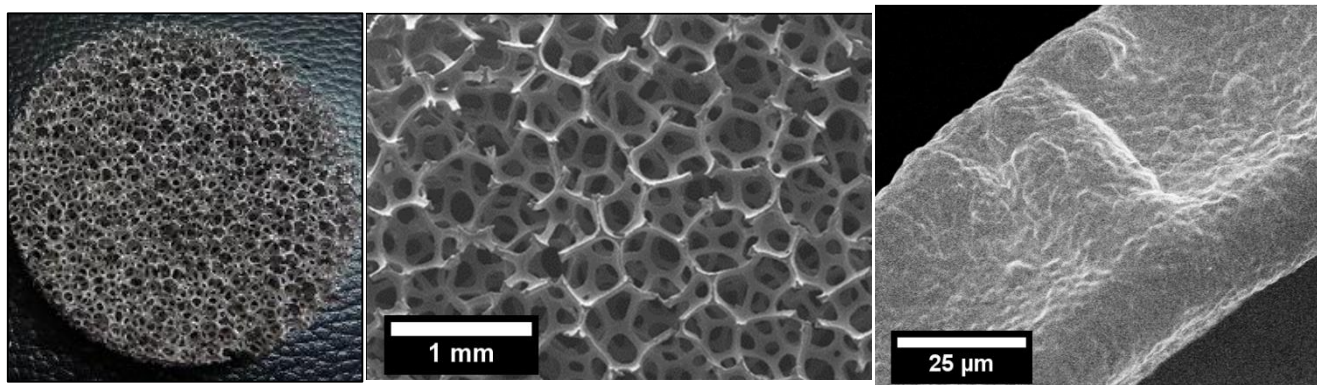


Figure 13: 5/8" nickel foam disc as a growth substrate for CVD (left), low magnification SEM image of nickel foam structure (center), and TEM image of nickel foam surface morphology (right).

growth substrate for carbon with the intent of growing carbon nanotubes or graphene on this substrate. Discs with a diameter of 5/8” (based on our test cell geometry) were punched out of nickel foam, bath sonicated in acetone for 20 minutes, and baked in a vacuum oven at 120C for 8 hours. The foam discs were then loaded into “Luigi”, our *Ultratech FIJI F200* ALD system for a 5nm thermal Al₂O₃ deposition process at 150°C. The purpose of this layer was to act as a CVD catalyst (Fe) diffusion barrier to prevent alloying with the Ni foam during the pre-growth ripening process. After ALD, a 7.5 angstrom Fe CVD catalyst layer was deposited in an *AJA International Inc. ATC 1800V* sputtering system. The sputtering process effectively penetrated the macroporous structure of the foam. With the CVD catalyst layer in place, the samples were weighed with a microbalance and then loaded into an *Atomate Corp.* low pressure chemical vapor deposition system for the acetylene-based carbon growth process. An outline of this process flow and a schematic of the resulting cathode structure after extensive process optimization are shown in **Figure 14**.

Optimization of this process yielded a new 3D electrode architecture of densely packed mesoscale arrays of vertically aligned carbon nanotubes (VACNT) grown directly on nickel foam. This self-supporting, hierarchically porous system features a binder-free, integrated current collector electrode, without requiring delamination of the CNT from the growth

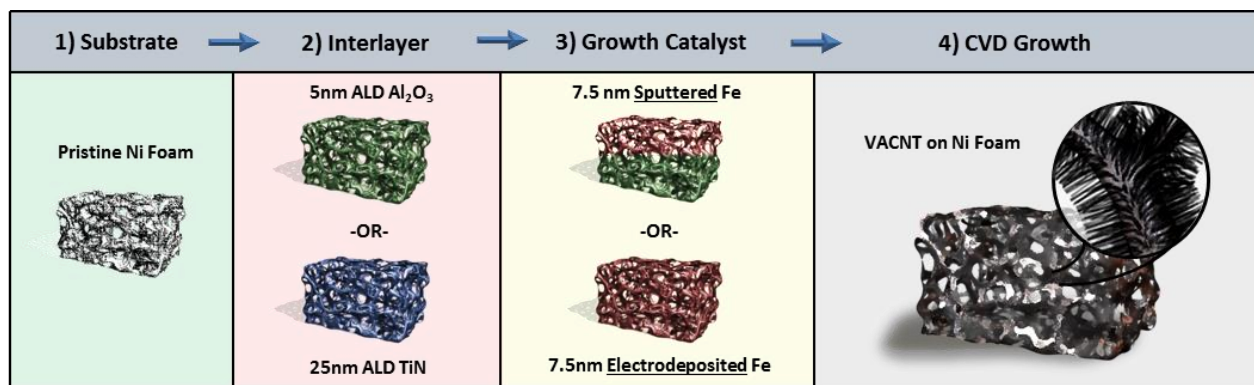


Figure 14: Process flow for chemical vapor deposition of vertically aligned carbon nanotubes on nickel foam.

substrate. Myriad reports of VACNT syntheses by CVD on metal substrates such as stainless steel^[38–40] and gold^{[41],[42]} have been published in recent years; however, to the best of our knowledge there is no successful growth of VACNT by CVD directly on a Ni substrate. The challenge in growing directly on Ni is due to accelerated diffusion rates of the CVD catalysts into the Ni substrate as compared to Si and insulating substrates. To overcome a similar problem, recently, Teblum et al. grew carpets of VACNTs by introducing a conformal but relatively thin (5nm) Al₂O₃ underlayer on a planar copper substrate and suggested the use of these VACNT for Li-ion battery anodes.^[43] This had been accomplished previously for a different application but required a thicker interlayer to achieve regular growth.^[44] However, in both cases, the use of 2D metallic substrates inherently limits the area-normalized mass loading of the VACNT, requiring growth of dense carpets of long VACNT in order to approach practical loading of individually aligned nanotubes on the mesoscale. Additionally, the pressure associated with assembling these planar electrodes in practical devices can significantly change the mesoscale morphology, tortuosity, and porosity of the VACNT carpet, which has not been addressed in previous reports.^[18,43]

The nickel foam current collector is a robust, macroporous structural scaffold (80-110 pores per inch, 95% porous) that minimizes deformation of the final freestanding electrode when closed in the test cell, maintaining less tortuous pathways for the active species. The open three dimensional structure of the foam promotes formation of VACNT domains, providing increased CNT sidewall exposure as compared to a 2-D substrate, and results in a hierarchical pore structure with uniform electrolyte and charge carrier accessibility into the VACNT carpet. Additionally, the growth of the VACNTs directly onto the Ni foam avoids the adverse impact of polymeric binders and the associated parasitic side reactions.^[17] While this electrode was

specifically designed for Li-O₂ research, we believe this structure is applicable to a variety of electrochemical systems, and tested its performance and degradation mechanisms in two different systems as scaffolds for reduction of oxygen and sulfur in rechargeable Li-O₂ and Li-S batteries. Characterization of the pristine structure in addition to electrochemical performance testing will be discussed in the next section.

3.3 Characterization of Pristine Structure

Scanning electron microscopy (SEM) images of the hierarchical cathode structure of VACNTs on the nickel foam are shown in **Figure 15**. Distinct directional domains of VACNTs are visible, offering a large amount of sidewall and top surface area access for the electrochemically active species. This structure is highly porous and features a hierarchical

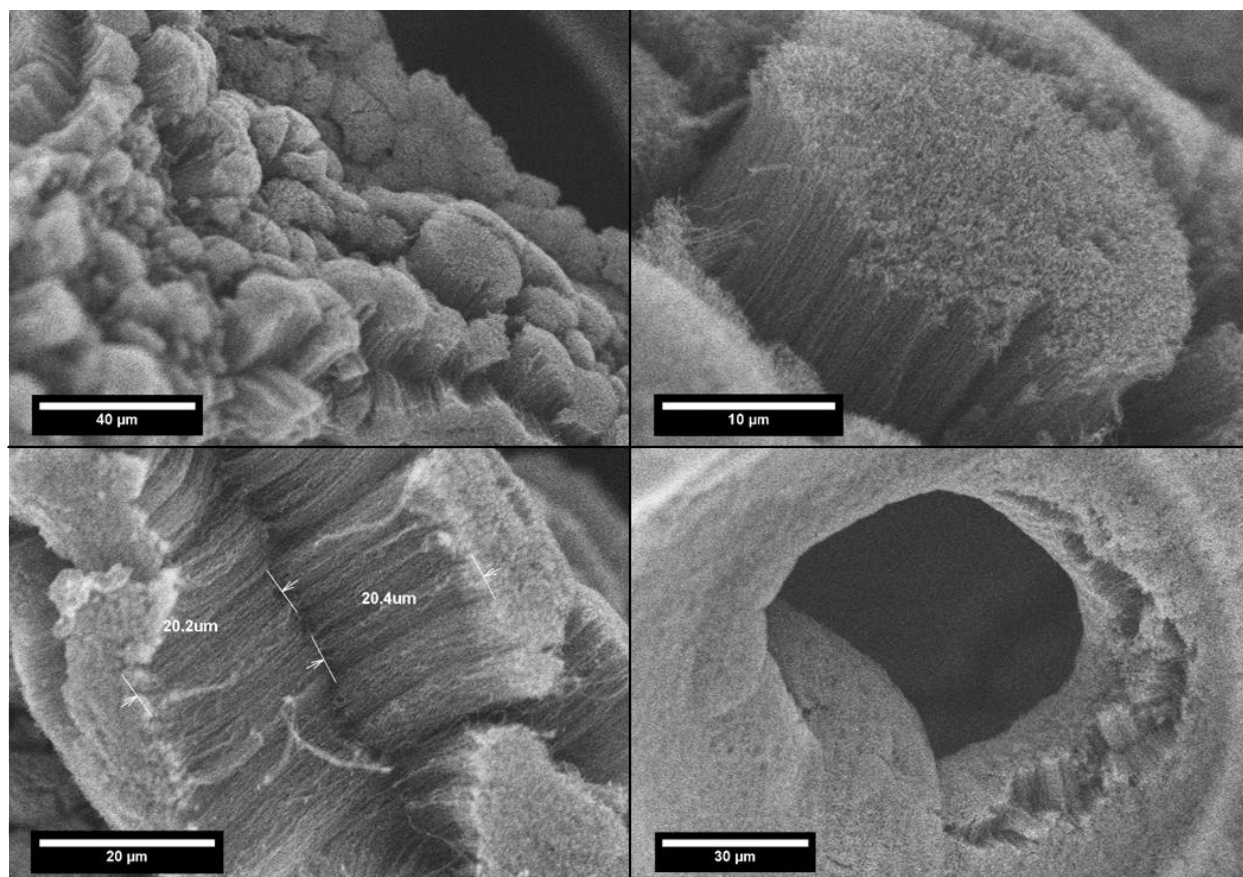


Figure 15: SEM images of vertically aligned carbon nanotubes grown on nickel foam. These images illustrate the desired dual pore hierarchical structure with mesoporous voidspace between the VACNT and macropores preserved by the underlying Ni foam.

architecture. The nickel foam itself is macroporous, with an open structure of interconnected branches and void-space on the order of $\sim 100\mu\text{m}$. The mesoscale array of micrometric domains of VACNT obtained is believed to be a product of the surface morphology of the underlying nickel foam (see Figure 13), and separated by distances of $\sim 10\mu\text{m}$. Adsorption isotherm indicates mesoporosity according to density functional theory (DFT) modeling of pore sizes which is in good agreement with the SEM, and a BET surface area of $\sim 300\text{m}^2/\text{g}$ which matches the geometry of the CNTs (7-10 walls). The VACNT length is tunable by modifying the growth time, and the growth conditions (**Table 2**). VACNT 3D carpets with length of $\sim 10\mu\text{m}$ were used for the cathodes in the Li-O₂ cathode experiments. No bare Ni was observed in the SEM, suggesting a dense, uniform coating of the Ni foam with the VACNTs. The growth of the VACNT was achieved throughout the entirety of Ni foam by two different methods of catalyst application, sputtering and electrodeposition, which allow 3D loading of the VACNT on the interconnected current collector. Transmission electron microscopy and electron diffraction confirmed that the growth is indeed CNTs, as shown in **Figure 16**, and that they have multiple walls (~ 10 walls).

Table II: Growth parameters for low pressure chemical vapor deposition (LPCVD) reactor during successful VACNT growth processes on nickel foam, as confirmed by SEM characterization. All growth substrates were nickel foam with 5nm Al₂O₃ underlayer and 7.5Å Fe,

Growth Temp	Ripening Temp (C°)	Growth Pressure (torr)	Precursor Flow Rate (sccm)	Ar Flow Rate (sccm)	H2 Flow Rate (during growth)	Post Growth Reduction? (H2 gas)	Comment (length/form?)
600	550 (15 min to 550)	2	200	100	0	200 sccm H2 10 mins	Short patches of VACNT growth
600	20 min to 550, 5 min to 600	12	300	100	0	200 sccm H2 10 mins	2 μm long clusters of VACNT
670	670 (16 min ramp)	12	200	120	0	None	Continuous domains of VACNT ($\sim 6.5\mu\text{m}$ long)
700	700 (10 min ramp)	12	200	120	0	None	Larger discrete very dense domains of VACNT ($10\mu\text{m}$)
750	750 (16 min ramp)	12	250	120	60	200 sccm Ar, no H2, 5 min @750	Conformal VACNT with good sidewall exposure, $20\mu\text{m}$ long
750	750 (16 min ramp)	12	200	120	0	None	Extremely dense continuous fields of VACNT (3-5 μm)

XPS of the as-grown 3D cathode showed that the VACNTs were extremely clean (minimal amorphous carbon), conductive, and conformal on the nickel foam substrate. The

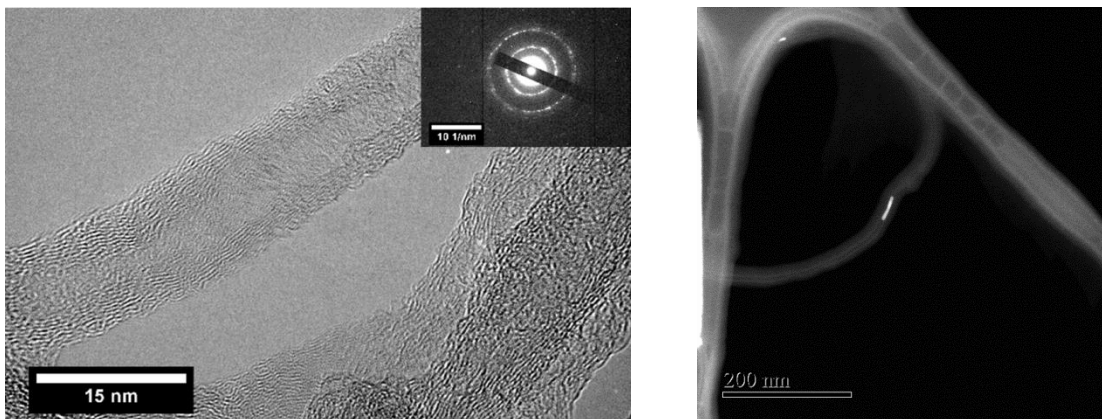


Figure 16: TEM and electron diffraction of the growth showing that the vertically aligned carbon structures are in fact, nanotubes with ~10 walls (left). STEM showing Fe CVD catalyst embedded in the base of the VACNT, suggesting a “base-growth” mechanism.

survey spectrum (Figure 17) demonstrates the only elements present to be carbon and a small amount of oxygen. Quantification of the high-resolution C 1s (shown in Figure 18) and O 1s (not shown) peaks indicated the composition to be 99.2% C and 0.8% O. Most of the oxygen is believed to be chemisorbed species acquired during transfer from the CVD system to the XPS. Notably, no signal from either the Ni substrate or the Al₂O₃ interlayer could be observed, demonstrating the complete conformality of the VACNT growth process. Further, no signal from the iron CVD catalyst was observed suggesting a “base-growth” mechanism, as further

supported by STEM images (Figure 16). The C 1s high resolution spectrum (Figure 18) was typical of highly crystalline pristine CNTs. The spectrum was well-fit with three components. The first is an asymmetric, narrow peak centered at 284.6 eV which is typical of sp² hybridized carbon as is found in CNT walls. The peak at 285 eV corresponds to sp³ hybridized carbons associated with

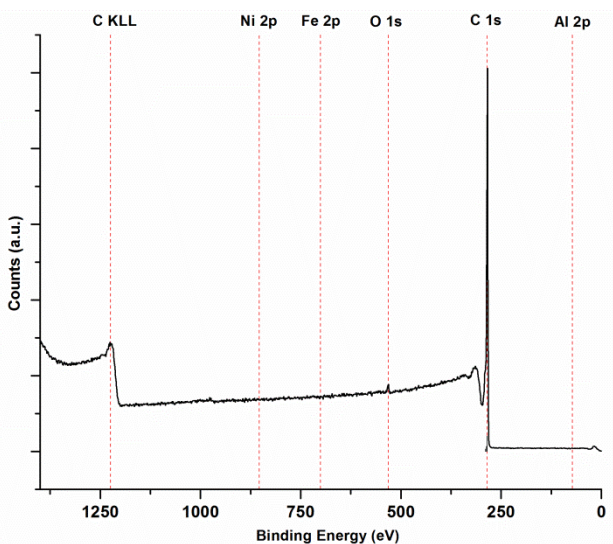


Figure 17: XPS Survey spectrum of the pristine cathode structure showing the only elements present are carbon and a small amount of oxygen.

disordered tube regions and small amounts of amorphous carbon. Presumably there is a very small peak associated with oxidized carbons in this region, but at a maximum of 0.8% of the total area it is unresolvable. The broad peak centered at 289.8 eV is associated with the π - π^* electronic transition found in highly conductive sp^2 carbon structures. These peak locations are in excellent

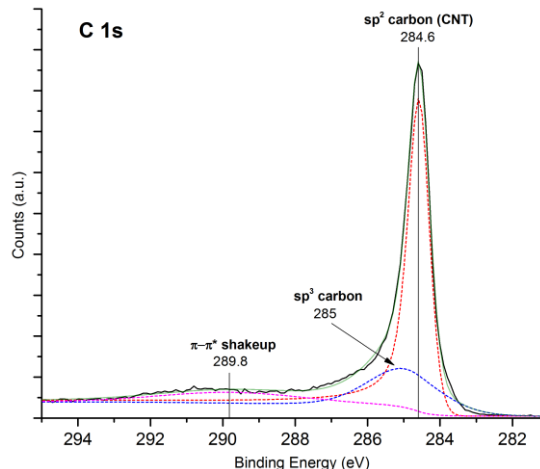


Figure 18: High-res C 1s spectrum of the as-grown cathode.

agreement with the literature^[45], highlighting the fact that the CNTs are conductively coupled to the Ni foam even through an ultrathin insulating interlayer. If they were not, more significant charging and peak shifting might be expected.

Characterization of the pristine electrode strongly suggests that this structure is an exciting and novel prospective cathode scaffold due to its dual-pore hierarchy, integrated current collector, and high mass loading and surface area of sp^2 -hybridized carbon. In the next section, performance results from electrochemical testing will be presented and discussed.

3.4 Electrochemical Testing

Electrochemical performance of the architecture as a Li-O₂ cathode was tested in three different electrolyte-solvent systems (0.1M LiClO₄ in dimethyl sulfoxide (DMSO), diglyme (dimethyl ether), and glyme (dimethoxyethane (DME))). These were some of the first Li-O₂ measurements we performed and at this time there was no clear solvent choice, so we wanted to gauge performance metrics in a few of the different solvents commonly used in literature as a basis for future experiments. **Figure 19a** shows the cathodic peaks generated during sweeping voltammetry, indicating higher onset voltages for ORR (or discharge) in DMSO and DME. This

result is mirrored in the galvanostatic discharge profiles at a rate of $20\mu\text{A}$ (10mA g_c^{-1}) in **Figure 19b**, showing superior performance (sustained discharge voltage) in DMSO and DME as compared to the diglyme-based electrolyte. This discharge corresponds to a high capacity of $2,000\text{mAh g}_c^{-1}$. We also tested rate performance with chronoamperometry (**Figure 19c**) in a DMSO-based electrolyte at three different voltages for comparison with a similar cathode structure featuring delaminated VACNT pressed onto a stainless steel mesh current collector.^[46] Our electrode architecture exhibited significantly higher discharge currents at the same potentials

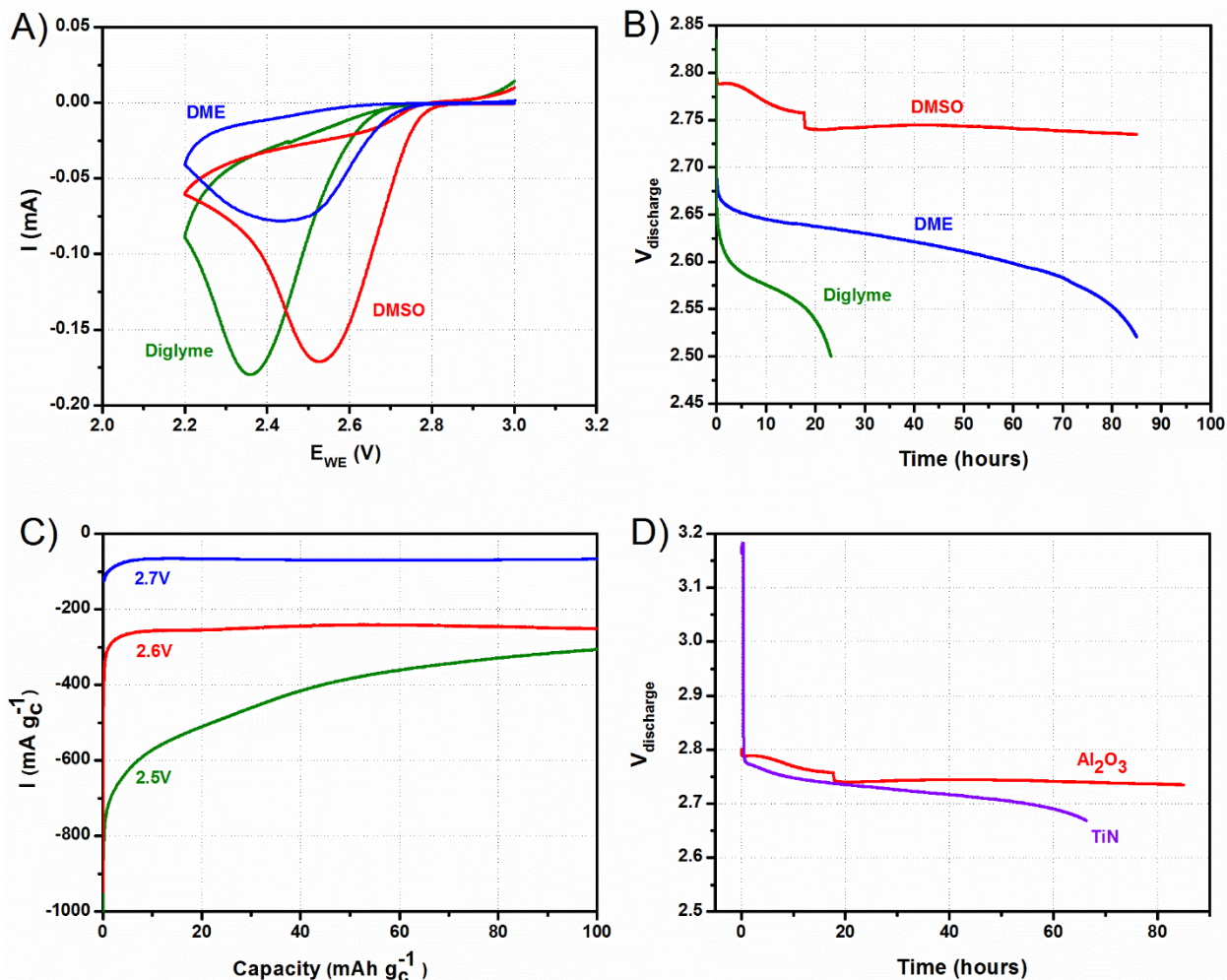


Figure 19: Electrochemical performance of the VACNT-Ni electrode architecture as a Li-O₂ cathode with 0.1M LiClO₄ in DMSO, DME, and Diglyme-based electrolytes. A) Cyclic voltammogram plot of the cathodic peak (indicative of ORR behavior) showing the most favorable onset potential for ORR in DMSO. B) Galvanostatic discharge at $20\mu\text{A}$ (cell current) showing superior discharge behavior in the DMSO-based electrolyte. C) Chronoamperometry measurements at different voltages in 0.1M LiClO₄ in DMSO. D) Galvanostatic discharge @ $20\mu\text{A}$ cell current of electrode structures with two different ALD interlayers.

vs. Li/Li^+ (100 mAgc^{-1} vs. 50 mAgc^{-1} at 2.7V, and 300 mAgc^{-1} vs. 110 mAgc^{-1} at 2.6V for our cathode and the delaminated VACNT electrode, respectively.^[46]

The observed differences in the discharge currents can be attributed to the hierarchically porous structure of our 3D cathode and the presence of an integrated current collector, providing improved electrical contact for the individual CNTs and a more homogenous current distribution over the entire conformally coated nickel foam scaffold. Despite significant carbon mass loading ($\sim 1.75 \text{ mg cm}^{-2}$), we believe that not all of the carbon in our structure is electrochemically active. Carbon diffusion into Al_2O_3 thin films in the temperature range of the VACNT CVD growth process has been observed^[47] and may explain the observed electronic conductivity of the Ni- Al_2O_3 -VACNT ALD interlayer, which is ordinarily a standard dielectric. Additionally a significant fraction of the VACNT is most likely inaccessible because the nanotubes are multi-walled. Both of these factors suggest the energy density of the active carbon in the structure is significantly higher.

In order to evaluate a possible voltage drop caused by the thin Al_2O_3 interlayer between the Ni and VACNT, we grew a cathode with the same structure, but changed the interlayer to conductive 25nm TiN layer deposited by ALD.^[48] The galvanostatic discharge profile comparison between the 3D cathode with Al_2O_3 interlayer and the 3D cathode with TiN interlayer is presented in **Figure 19d**. A similar initial ORR potential was observed, independent of the conductivity of the interlayer, suggesting the thin Al_2O_3 layer does not impede the electrical connection between the Ni and VACNT. The more stable discharge voltage plateau of the cathodes with the Al_2O_3 interlayer as compared to a TiN interlayer, as shown in Figure 19d, was unexpected, but could be related to the relative stability of the interlayers in the presence of oxygen radicals which induce oxidation of the TiN layer during a long discharge process^[49] and

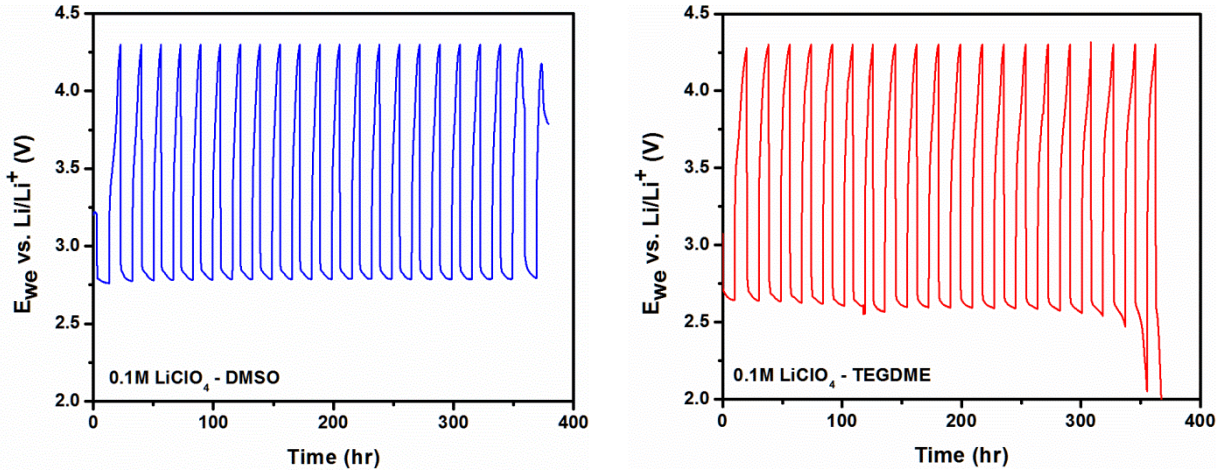


Figure 20: Galvanostatic cycle profile comparison of VACNT-Ni foam electrode architecture operated in Li-O₂ cells with two different electrolytes. The DMSO shows slightly better performance, reaching the 22nd discharge without failure and maintaining a consistently higher discharge voltage (~2.75V for DMSO vs. 2.65V for TEGDME)

would result in an increased interfacial resistance, leading to declined performance and discharge potential. Due to inferior performance, known difficulties in reproducibility with TiN growth layers^[50], and demonstration of no negative effect of the Al₂O₃ interlayer on the ORR potential, we decided to use ALD Al₂O₃ as the growth interlayer.

The cathode performance over extended galvanostatic cycling was also tested in DMSO and tetraglyme (tetraethylene glycol dimethyl ether (TEGDME)). **Figure 20** shows the cycle profile performance comparison, with DMSO exhibiting slightly better behavior, as indicated by the consistently higher discharge voltage and cyclability exceeding the TEGDME cell. A comparison of select cycle profiles from the DMSO cell cycling is shown in **Figure 21**. Aside from the first cycle which shows slightly enhanced charging behavior, the OER/ORR profiles are stable. These results are extremely competitive for a pure carbon

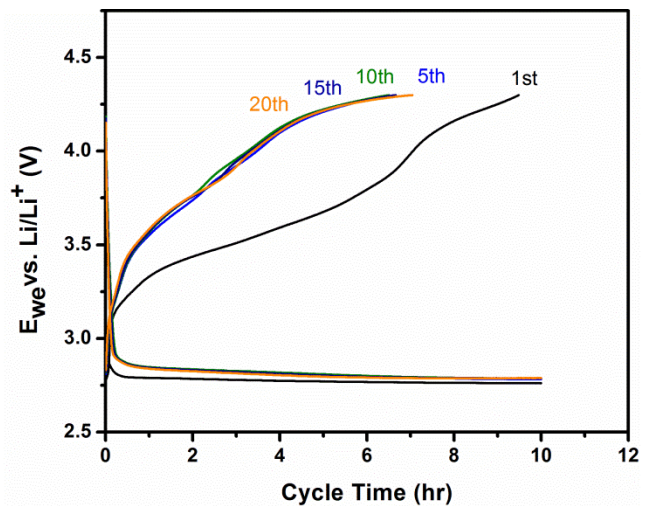


Figure 21: Comparison of select cycle profiles from the DMSO-cell in Figure 20.

system without a catalyst, and the cycle stability is attributed to the sp^2 hybridized carbon.^[19,29]

3.5 Characterization of Cycled Cathodes

Characterization of the electrodes after cycling yielded significant insights regarding the performance strengths and limitations of the electrode architecture. SEM and TEM imaging of the cathodes was performed to characterize the morphology of the reduction products. **Figure 22** shows images of the cathode after a single galvanostatic discharge @20 μ A cell current to 2V. In Figure 22a, it is clear the underlying structure of the VACNT forest is maintained; however, the CNTs are not exposed and the mesopores appear to be heavily saturated with the discharge products. These images emphasize the strength of hierarchical porosity and indicate that the reaction was not limited by a deficiency of active species throughout the discharge reaction, even to extreme depths of discharge. The reduction products appear to have a spherical morphology,

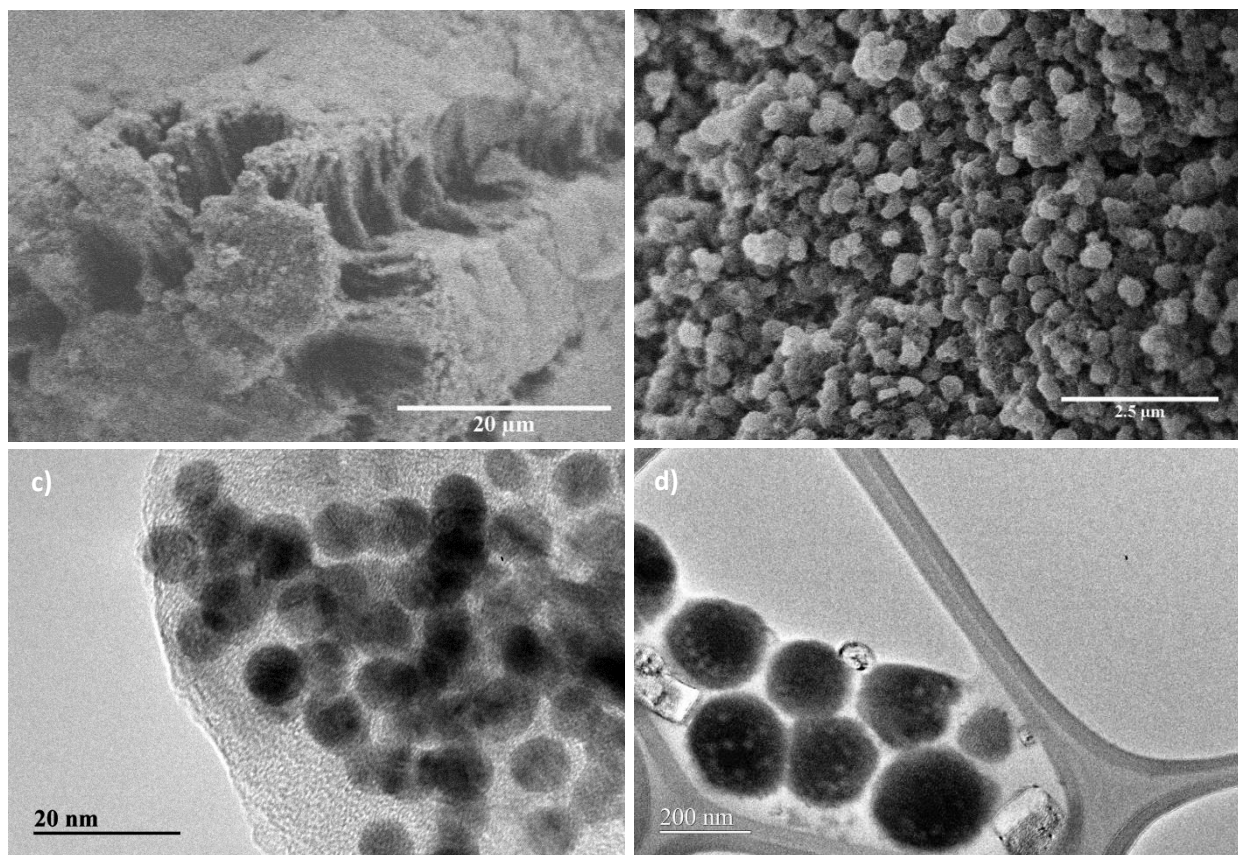


Figure 22: SEM (a,b) and TEM (c,d) images of a cathode galvanostatically discharged to 2V vs. Li/Li⁺

which is consistent with previous literature on Li_2O_2 .^[18,19,28,34,46]

XPS analysis of the discharged cathode was completed in-situ via direct transfer from the glovebox through a UHV system as presented in Figure S4. The cathode was never exposed to air or any measurable source of moisture. The survey spectrum (Figure 3) indicated the presence of C, O, Li, and Cl, as well as trace amounts of N, Si, and S. Again, there was no indication of Ni (or Al from the ALD interlayer), indicating that the ALD could be preventing dissolution of the current collector into the electrolyte and that the nanotube coating is still both dense and conformal. The high resolution spectra were calibrated relative to the primary carbon peak at

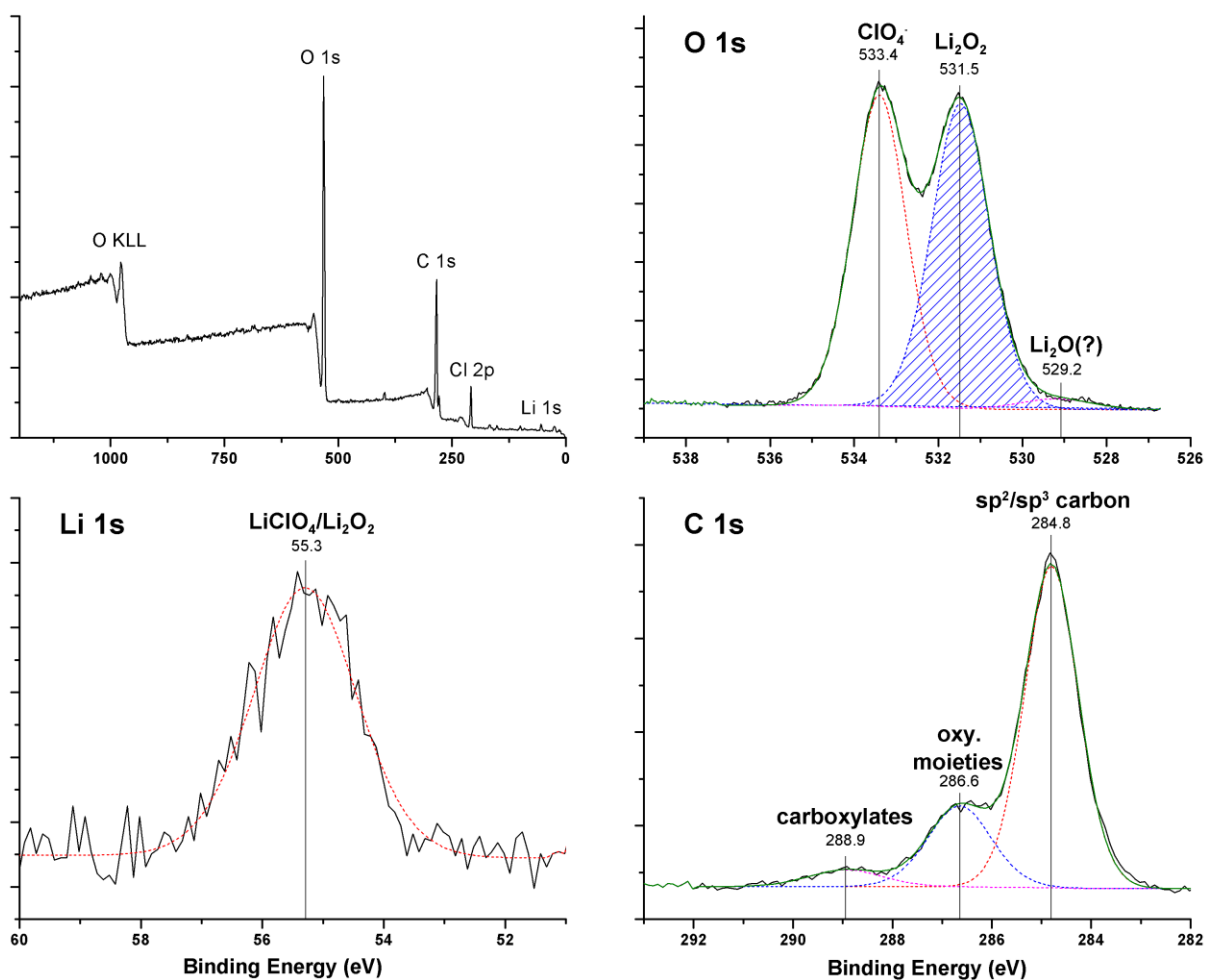


Figure 23: XPS spectra of discharged cathode including survey scan (a) and high resolution scans of (b) O 1s, (c) Li 1s, and (d) C 1s peaks.

284.8 eV (a blend of the positions of sp^2 and sp^3 carbons). The identity of the majority of the surface film is a combination of lithium salt from evaporated electrolyte and Li_2O_2 as the primary discharge product with possibly some $LiOH$ and Li_2O , as confirmed by both peak positions and atomic quantification. The only other discharge products identified include a small amount of oxidation of the VACNTs themselves, as well as some carboxylates likely generated from atmospheric hydrocarbon contamination before cell closure. The absence of a significant quantity of carbonates is a decent indicator of stability with respect to the cathode-electrolyte interface.^[19]

SEM imaging of the cathodes after the first charge (**Figure 24**) show that a significant amount of the discharge products are evolved. Despite the slight collapse of the tube forest domains, the cathode structure is generally preserved after a single charge cycle. Imaging of cathodes after extended cycling and performance decline begins to shed light on degradation in these structures. As shown in **Figure 25**, delamination of the VACNT from the Ni foam current collector surface appears to be a common failure mechanism for systems operated both in TEGDME and DMSO-based electrolytes. These sections of the cathode can no longer participate in OER/ORR, thus resulting in a significant loss of capacity and increases in cell overpotential

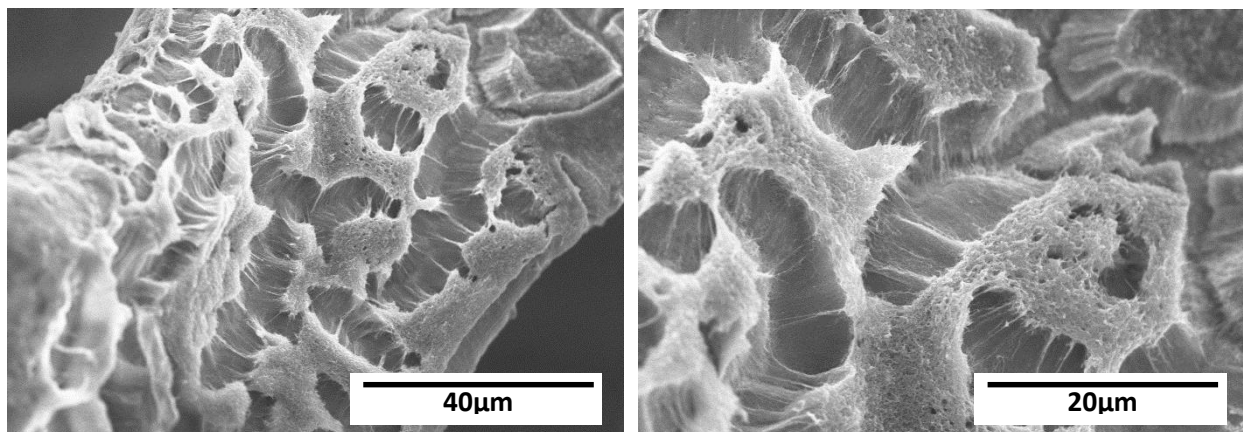


Figure 24: SEM images of VACNT-Ni cathode after 1st charge. The VACNT tube forests are slightly collapsed but remain intact and a significant amount of the reduction products have been evolved.

due to amplified current density in the intact portions of the structure. Because this mechanism is observed in cathodes cycled in two different electrolyte systems, it is less likely to be related to a

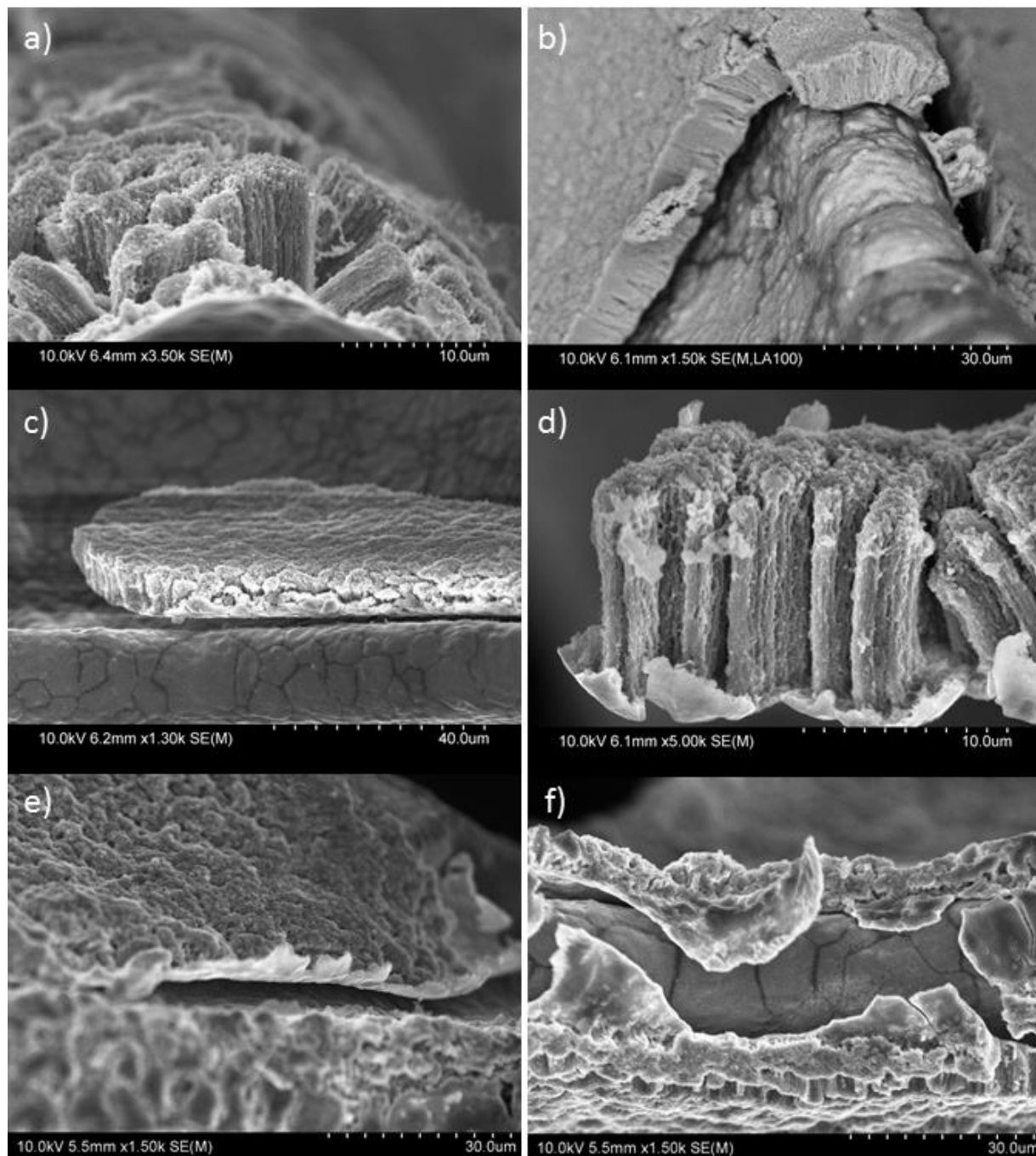


Figure 25: VACNT cathode after extended cycling showing delamination of the VACNT from the current collector. This mechanism is suspected to be the cause of the observed performance decline in capacity and discharge voltage. Images a-d are of the cathode cycled in DMSO with e and f showing a similar degradation mode for a cathode cycled in TEGDME-based specific electrolyte chemistry stability problem, but elucidating the specific cause of this mechanism will be discussed more in the next section.

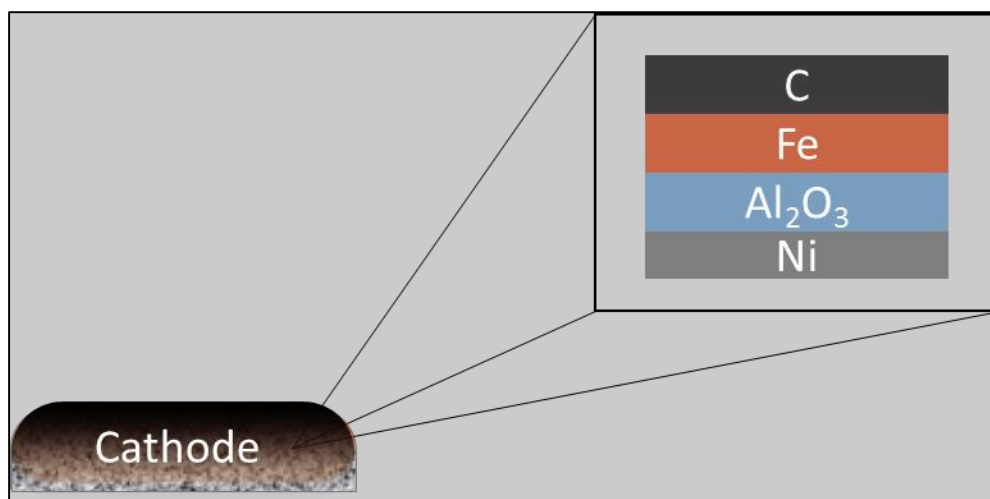


Figure 26: Schematic showing the interfaces in the VACNT-Ni cathode architecture as a roadmap for identifying potential failure mechanisms.

3.6 Degradation Mechanism

Due to the nature of the failure, our investigation of the degradation mechanism began by considering the interfaces present in the structure, as shown in **Figure 26**. As shown in the schematic, there are three main interfaces that could be the cause of failure (Ni- Al_2O_3 , Al_2O_3 -Fe, and Fe-C). Atomic layer deposition of Al_2O_3 on a native metal oxide is expected to form a very stable interface that would be inherently resistant to oxidation or decomposition, and as such, this conformal layer/interface was not expected to be the cause of delamination. STEM of the grown VACNT (Figure 16) shows that the Fe layer is incorporated into the base of the carbon as a result of the growth mechanism, meaning that the only other effective interface remaining is carbon- Al_2O_3 . Both XPS and EDS characterization of residual surface after delamination of the VACNT (see the dark, textured subsurface in Figures 26c and 26f) indicate that this surface is purely carbon, with no signal from the underlying Ni foam. Thus, rather than failure at the C- Al_2O_3 interface, these observations suggest that the break point is somewhere in the carbon growth itself. After some searching in the literature, we discovered a logical mechanism had already been discovered and put to use for a different purpose—VACNT release and transfer.

Experts in chemical vapor deposition of carbon had discovered that weakly oxidative environments could be used for delamination of VACNT from the growth substrate for applications requiring transfer.^[51,52] This mechanism is possible due to difference in chemical stability of the

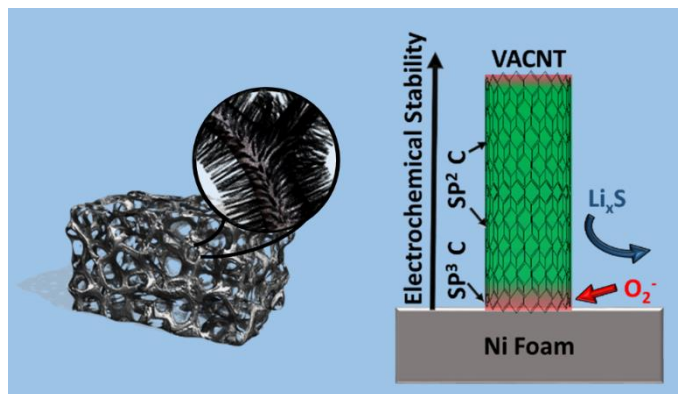


Figure 27: Schematic outlining the mechanism for degradation of the CNT base that eventually leads to complete fracture and delamination of the tubes from the current collector. The higher concentration of defects and sp^3 hybridized carbon at the interface are more susceptible to oxidation by $Li-O_2$ intermediates and products.

CNT root from the rest of the nanotube. Compared with well-crystallized graphite layers in the main tube body, the root contains a higher density of amorphous carbon, turbostratic carbon, and carbon in contact with metallic catalyst particles (high electron density), all of which are more susceptible to oxidation (**Figure 27**).^[53–55] Thus, throughout $Li-O_2$ battery operation, the presence of highly oxidative intermediates and products gradually weakens the carbon nanotube roots until mechanical stress from the peroxide formation and evolution of trapped O_2 are enough to completely delaminate the tubes from the surface of the current collector.

This type of failure presents a new mechanism for degradation of mesoscale $Li-O_2$ positive electrode architectures. Despite the enhanced power capabilities and robust structure offered by an integrated current collector, susceptibility of the carbon growth at the interface to the presence of aggressively oxidative species strongly discourages the application of these structures to this specific advanced battery technology. In an effort to confirm the mechanism, we also tested the electrode architecture as a scaffold for the reduction of sulfur in another next-generation battery technology, the $Li-S$ battery. The $Li-S$ cathodes were synthesized via impregnation of Li_2S_6 solution made in DME into the VACNT cathode with a sulfur loading of

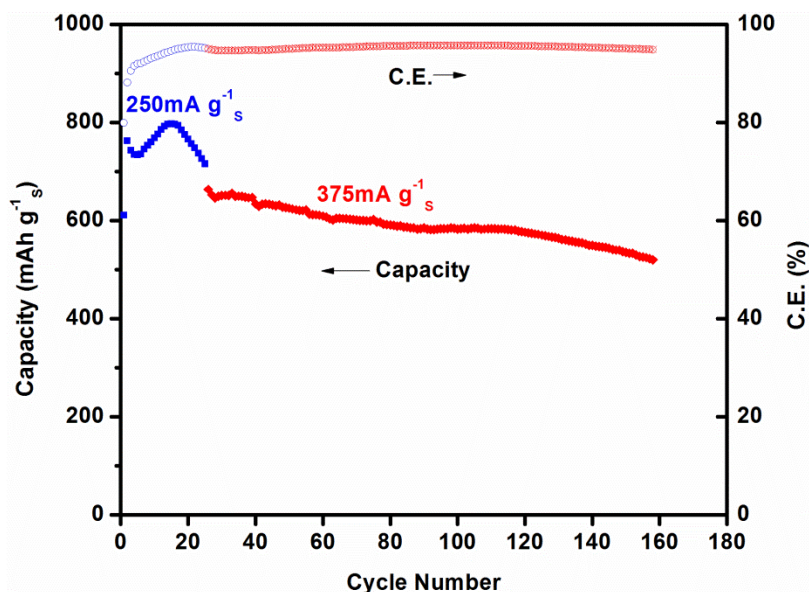


Figure 28: Galvanostatic cycling performance of VACNT-Ni Li-S cell cycled at two different rates ($250\text{mA g}^{-1}_{\text{s}}$ and $375\text{mA g}^{-1}_{\text{s}}$)

1.25mg cm^{-2} . The electrolyte used for these tests was 0.3M LiTFSI with $2\%\text{LiNO}_3$ in DOL:DME .

As a scaffold for polysulfide redox reactions in a Li-S battery, this 3D electrode yielded promising cycling stability (Figure 28) at high rates ($250\text{mA g}^{-1}_{\text{s}}$ and $375\text{mA g}^{-1}_{\text{s}}$)

without exhibiting a similar degradation mechanism, suggesting that contact between the CNT and integrated current collector is sensitive to intermediates and products associated with oxygen reduction and evolution, but stable toward sulfur reduction. The gradual loss of capacity while cycling at high rates can be associated with loss of sulfur to insoluble, inactive short chain polysulfides.^[14,56] SEM imaging of the cathode after cycling shows that the VACNT are well preserved under a thin solid electrolyte interfacial layer (SEI).

While Li-S batteries are not the focus of this dissertation, the excellent performance of this electrode architecture as a Li-S cathode reveals the utility of mesoscale, hierarchical architectures with an integrated current collector for a variety of energy

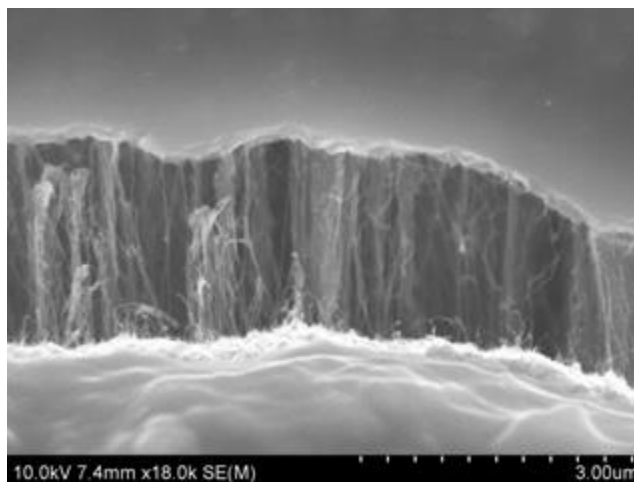


Figure 29: SEM of VACNT-Ni cathode after 150 cycles as a Li-S cathode. The VACNT are still in contact with the nickel foam under a thin solid electrolyte interface layer.

storage applications. It is also clear that electrode design for Li-O₂ battery applications requires even more stringent considerations for chemical/electrochemical stability.

3.7 Conclusions

In summary, we successfully conceived, developed, and tested a novel 3D, hierarchically porous, freestanding Li-O₂ electrode architecture. The electrode performed well as a high capacity, Li-O₂ cathode scaffold for oxygen reduction and the integrated current collector yielded significant enhancements in rate performance as compared to previously published structures in which VACNT were delaminated from the growth substrate. Long term cycling studies revealed a new failure mechanism associated with oxidation of the tube base, resulting in delamination of the CNT from the Ni foam and corresponding losses in capacity and increases in overpotential. This work contributes new understanding regarding the growth of VACNT directly on metal (and specifically Ni) substrates with the use of a thin ALD interlayer, and reveals important implications regarding the use of mesoscale architectures for next generation battery applications.

Chapter 4: Realization of Rechargeable Li-O₂ Cathodes with Catalysts Deposited via Atomic Layer Deposition

4.1 Introduction

Having developed a lab scale infrastructure for Li-O₂ research and learned the basics of Li-O₂ battery chemistry and its associated components with the VACNT-based electrode architecture, the next project was to incorporate catalysis as a mode of realizing a stable, rechargeable Li-O₂ battery. While considerable research efforts have been dedicated to the exploration of OER/ORR catalysts for Li-O₂ batteries^[6,22,34,57-62], the promise of atomic layer deposition as a mode of conformally functionalizing complex architectures with catalysts of

different chemistries and morphologies is just beginning to be realized. This is confirmed by a literature search, revealing a handful of works using ALD-deposited heterogenous catalysts for general OER/ORR studies^[63–67] and only two specifically dedicated to Li-O₂ batteries.^[68,69]

Based on our previous success with carbon nanotubes as a cathode material and new insight regarding the cause of degradation of the VACNT structure, a multi-walled carbon nanotube sponge (MWCNT) was the selected cathode substrate for these catalyst studies. Made available by a collaboration with Dr. Liangbing Hu's group in Materials Science and Engineering (MSE), the unique properties of this sponge material include high electronic conductivity, large surface area with mesoporosity, good chemical stability, and low intrinsic defect density which has been shown to greatly improve stability of carbon-based cathodes.^[29] Three-dimensional networks of carbon nanotubes exhibit considerable promise as mesoporous O₂ electrodes^[70] as a result of an open structure with high surface area that is conducive to reduction product storage and diffusion of active species, particularly at significant depths of discharge. This MWCNT sponge has the added advantages of a freestanding structure, further improving cell stability by avoiding the use of a binder^[71] and offering extensive versatility as a scalable substrate platform for both practical and fundamental Li-O₂ studies. The sponge is fabricated in bulk samples with a ferrocene-based spray-catalyst chemical vapor deposition process described elsewhere.^[72]

With a new cathode platform and a variety of ALD precursor chemistries, we began fabricating cathode architectures functionalized with different catalyst chemistries. For substrate surface chemistries that are chemically inert with respect to the precursor ligand chemistry, such as the sp² hybridized carbon in the MWCNTs, deposition will only be nucleated at defect sites, resulting in island growth as described by the Volmer-Weber growth mechanism.^[25] Thus, ALD

offers tremendous control for fabricating highly dispersed, heterogenous catalyst nanostructures with excellent control over mass loading and morphology. We used these strengths of atomic layer deposition to functionalize sponge cathodes with a variety of chemistries (Ru, RuO₂, Pt, MnO, Ru+Pt, ZnO, and TiO₂).

Due to the high capacity of Li-O₂ batteries, conventional cycle durations are significantly longer than almost any other electrochemical energy storage platform, so a quick diagnostic for gauging OER/ORR activity was critical to preserve resources (cells, channels, and time) for the most promising chemistries. Cyclic voltammetry is the most versatile electroanalytical method in this regard. By sweeping the potential of the working electrode (positive electrode in Li-O₂ cell) vs. a reference (the Li metal anode, also the counter electrode in this case) in a triangular waveform between upper and lower potential limits, the measured current reflects potential windows for electrochemical activity. The obtained voltammogram displays the current (response signal) vs. potential (excitation signal). The potential scan rate is an extremely useful input for discerning kinetics of different electrochemical processes, but is generally kept constant at 0.50mV s⁻¹ in this work since we

are interested in gauging OER/ORR activity of similar structures. A composite voltammogram of the sponges with different catalysts is shown in **Figure 30**. The important aspects of these plots are the onset potentials for OER/ORR (thermodynamic values) and the

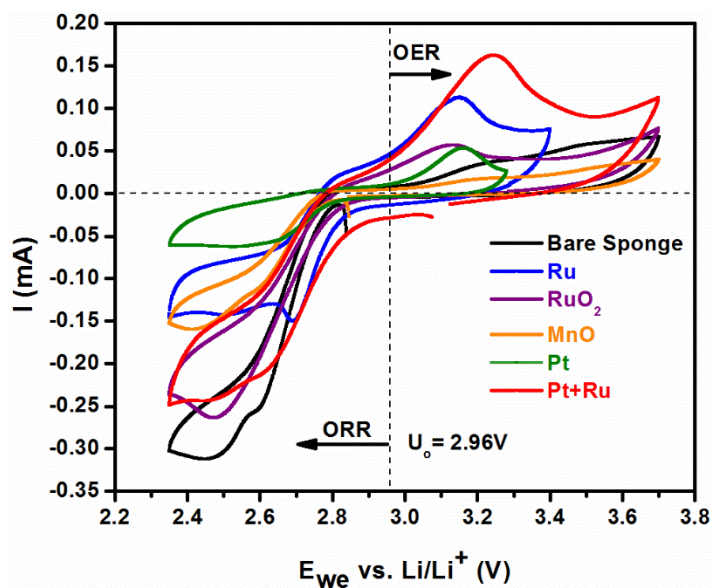


Figure 30: CV of MWCNT sponges loaded with ALD catalysts to probe OER/ORR activity.

magnitude of the current which can be roughly correlated to the activity of the catalyst (value is highly dependent on the mass loading and surface area of the catalyst). The cathodic peak, which is manifested during potential sweeps below and away from the thermodynamic reaction potential ($U_o=2.96V$) corresponds to the discharge reaction (ORR) and the catalysts performed accordingly ($ORR_{onset} : Pt/Ru > Ru > RuO_2 > Pristine\ Sponge > Pt > MnO$). The anodic peak, which is indicative of the OER reaction during charge, is manifested during potential sweeps above and away from U_o , and the catalysts performed accordingly ($OER_{onset} : Ru < Pt/Ru < RuO_2 < Pt < Pristine\ Sponge < MnO$). Based on the promising OER/ORR behavior of the Ru-based electrocatalysts, we proceeded with a further investigation of this system.

Ru-based catalyst systems deposited via wet chemical methods have been investigated in recent works for Li-O₂ batteries.^[73–75] Unfortunately, the reported cells were tested over a large parameter space (e.g. carbon mass loading, different carbon types, O₂ pressure/volume, catalyst loading amount and morphology, electrolyte, etc.), making a performance comparison of the different reported Ru-based catalysts extremely difficult. Furthermore, the cycling conditions are not always adequately reported, thus complicating any effective comparison of cell current or true cycle duration.^[76] By studying comparable systems using the same electrochemical test platform with clearly outlined process parameters, we are able to draw an effective assessment between cathode substrates selectively functionalized with Ru or RuO₂ nanoparticle catalysts via atomic layer deposition, as outlined in the next section.

4.2 Synthesis and Characterization of Pristine Ru-based Cathodes

Synthesis of the sponge/catalyst composites was performed with an ALD process previously developed by our group^[77,78] for deposition of Ru or RuO₂ depending on the oxygen dose in the deposition process. ALD presents a distinct advantage over the wet chemical methods

used for Ru/RuO₂ decoration in previous works because surface reactions will be more energetically favorable on defect sites in the sp² hybridized carbon.^[79,80] Because these defect sites and the oxygenated functional groups associated with them are active sites for superoxide radical attacks to form carbonates^[29], the ALD growth simultaneously augments cathode stability by selectively passivating defects in the MWCNT substrate while decorating the sponge with the Ru-based catalyst for enhanced ORR/OER activity. Chemically binding the catalyst to the substrate during atomic layer deposition may also improve long-term durability as compared to other Ru/RuO₂ decoration methods which have shown tendencies toward catalyst particle aggregation during cycling.^[81] Additionally, the excellent thickness control granted by ALD allows for decoration of the cathode substrate while preserving the mesoporous structure of the

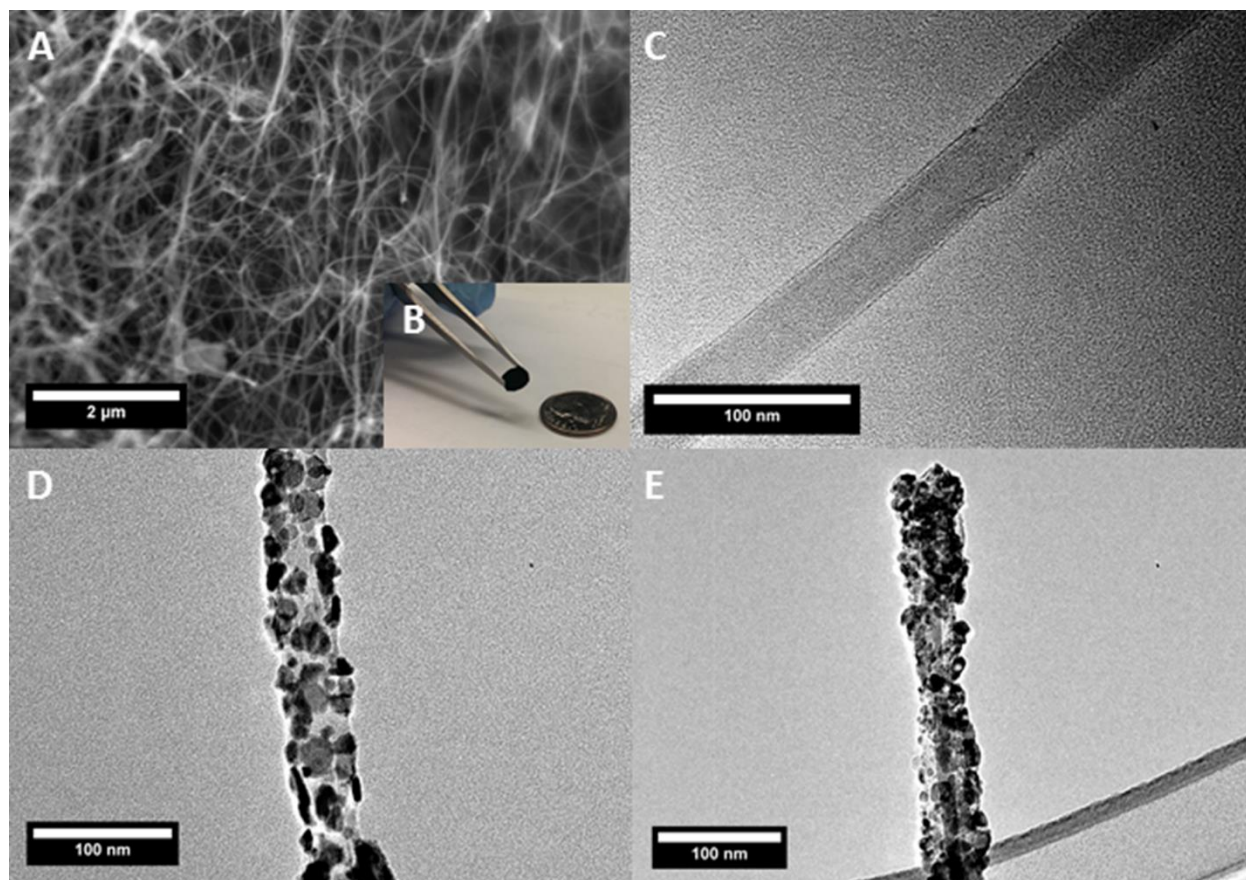


Figure 31: SEM (a) and TEM(c) of the pristine MWCNT sponge cathode shown in (b). TEM images of the sponge after 300 cycles of Ru (d) and RuO₂ (e) ALD.

sponge.

SEM and TEM images of the pristine sponge, as shown in **Figure 31a/c**, confirm the mesoporous structure and show that the individual carbon nanotubes (CNTs) have an average diameter of $\sim 30\text{nm}$ with 10-20 walls. The macroscale stability and freestanding nature of the sponge is demonstrated in Figure 31b, as a cathode is held between tweezers near a U.S. dime for size comparison. The inherently low defect density on the surface of the CNTs results in growth characteristic of ALD nucleation, as shown in Figure 31d/e, in which MWCNTs are decorated with discrete nanoparticles of ruthenium or ruthenium oxide after 300 cycles of the respective ALD growth process, while the open network of the sponge is preserved. The self-limiting nature of the ALD process enables controlled nucleation of the catalyst particles on the CNT with morphology/size loosely dictated by the number of process cycles.

XPS characterization of the pristine MWCNT before and after the 300-cycle Ru and RuO₂ ALD processes are shown in **Figure 32**. The sharp C 1s peak of the pristine sponge, shown in Figure 32a, is characteristic of the sp² hybridized carbon in CNTs and shows signs of very mild oxidation and/or adsorbed oxygen with some amorphous carbon, consistent with the low density of surface defects that enable nucleation growth of ALD catalyst. After ALD, XPS

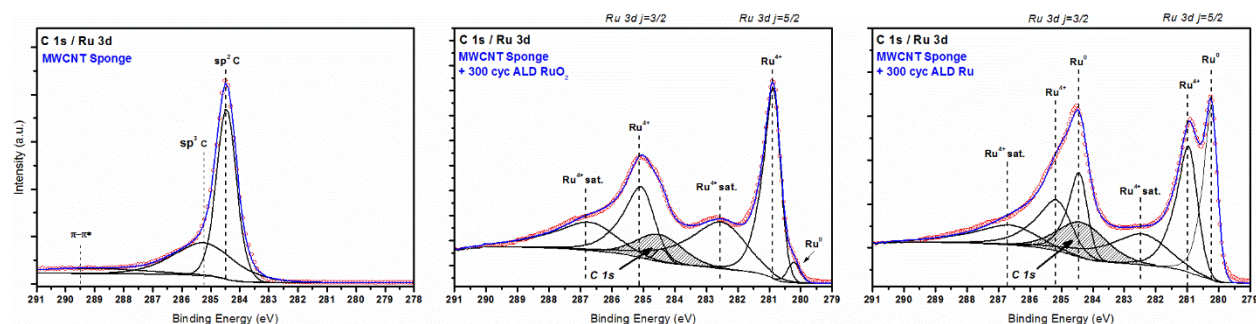


Figure 32: High resolution XPS spectra of the C 1s/ Ru 3d region of the a) pristine, b) RuO₂ functionalized, and c) Ru functionalized MWCNT foam. Red open circles indicate raw data, and blue lines show the fitted envelope. The spectra are normalized to the same arbitrary intensity. The spectrum in (a) is typical of high quality carbon nanotubes. The spectra in (b) and (c) are dominated by signal from the Ru 3d orbital, as its photoelectron cross section is over 15 times larger than that of the C 1s. (b) supports the deposition of nearly pure RuO₂, while (c) shows the deposition of metallic Ru which is covered by a thin native oxide. The “Ru⁴⁺ sat.” peak refers to a conduction band screening final state effect commonly observed in conductive ruthenium oxides.^[116]

indicates the presence of metallic Ru and a thin native oxidized surface layer consistent with RuO₂ in Figure 2b. The spectrum in Figure 2c for the RuO₂ ALD process is consistent with bulk RuO₂. TEM characterization of these growth processes indicates that the mesoscale morphology of the cathode is preserved, maintaining access for transport of active species while functionalizing the sponge with controlled catalyst chemistries, enabling a direct performance comparison.

4.3 Electrochemical Characterization

The cyclic voltammetry (CV) response of the bare sponge and the decorated MWCNT cathodes are presented in **Figure 33**. For the pristine MWCNT the first cycle is plotted since after this cycle the onset of OER was shifted to significantly higher potential, possibly due to oxidation of the cathode surface.^[14,19,29,76] The CV responses of the decorated cathodes were stable for all of the 10 recorded cycles, and the fourth cycle of each measurement is plotted in Figure 33a. As obtained, the onset potentials for ORR are higher for the catalyst-loaded cathodes, suggesting enhanced activity which agrees well with the report on catalytic trends for

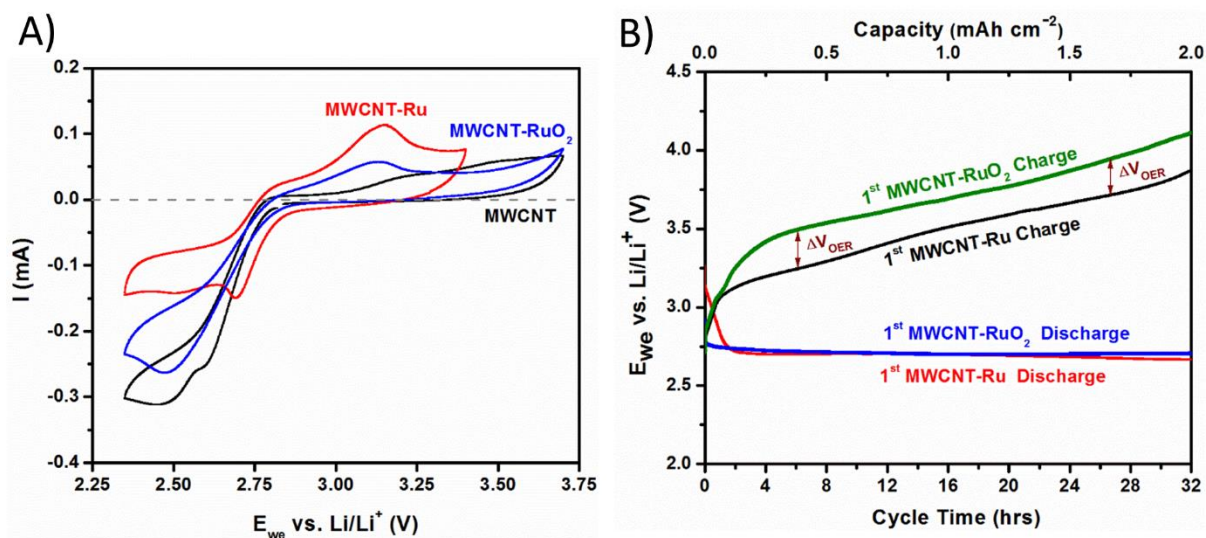


Figure 33: A) Cyclic voltammetry of bare MWCNT sponge (1st cycle shown) and sponges loaded with 300cyc ALD Ru and 300cyc ALD RuO₂ (fourth CV cycles shown). The scan rate is 0.5mVs⁻¹. B) Comparison of first galvanostatic charge/discharge profile with a 20μA total cell current for sponges loaded with catalyst. Despite little difference in ORR behavior, Ru exhibits significantly lower charge voltage for full capacity recovery.

ORR.^[61] In particular, the Ru-decorated cathode demonstrates superior ORR activity, shifting the onset potential for oxygen reduction from $\sim 2.8\text{V}$ to $>2.85\text{V}$. The more prominent improvement in activity is observed during the oxygen evolution reaction, with significant increases in current obtained at much lower onset potential as compared to the pristine MWCNT, approaching the theoretical value for the OER of Li_2O_2 (3.1V vs. Li/Li^+) at low scan rates. The Ru decorated cathode demonstrated higher reversibility than the RuO_2 , by recovering the charge gained during the cathodic scan at lower potentials in the anodic scan. Despite the enhanced OER activity exhibited by both catalyst systems, **Figure 33b** shows the significant decrease in charge overpotential ($\sim 0.3\text{V}$ lower compared to RuO_2) after the first discharge exhibited by the MWCNT/Ru cathode.

We tested the galvanostatic cycling stability of our MWCNT@ALD-Ru cathode with round trip cycle duration of 180 minutes (90 per discharge) and a current density of 200mA g_c^{-1} . As indicated by the stable cycle profile overlay in **Figure 34C**, the cathode was able to deliver the discharge capacity for 300 cycles under these conditions (Figure 34d). The stability of this voltage profile and the extremely long cycle life is even more remarkable considering our cell is a full Li- O_2 cell, with a Li metal anode, whereas a similar cathode stability study used a more stable electrode material as the counter electrode (Li source).^[82]

While the previous experiment confirmed the stability of our cathodes under high current densities and relatively short round-trip durations, a recent investigation suggested that the absolute exposure time of the Li_2O_2 discharge product to DMSO is crucial factor in the evaluation of the chemical stability of the deposited peroxides on the surface of the MWCNT.^[83] The implication is that while many works perform cycling studies with a short individual cycle time to probe the performance of their system, cycling studies with longer individual cycle

durations are necessary to gauge the chemical stability of the cell components during extended operation. To test this, we also cycled our Li-O₂ cell for longer cycle durations (see 34a/b) to address the chemical instability of the system under extended exposure of the solvent and cathode to Li₂O₂ and O₂⁻. The round-trip cycle duration was 64 hours (32 hour discharge) and full recovery of the capacity was obtained at voltages below 4V for more than 20 consecutive cycles. To our knowledge, this is one of the longest individual cycle durations used in a study of

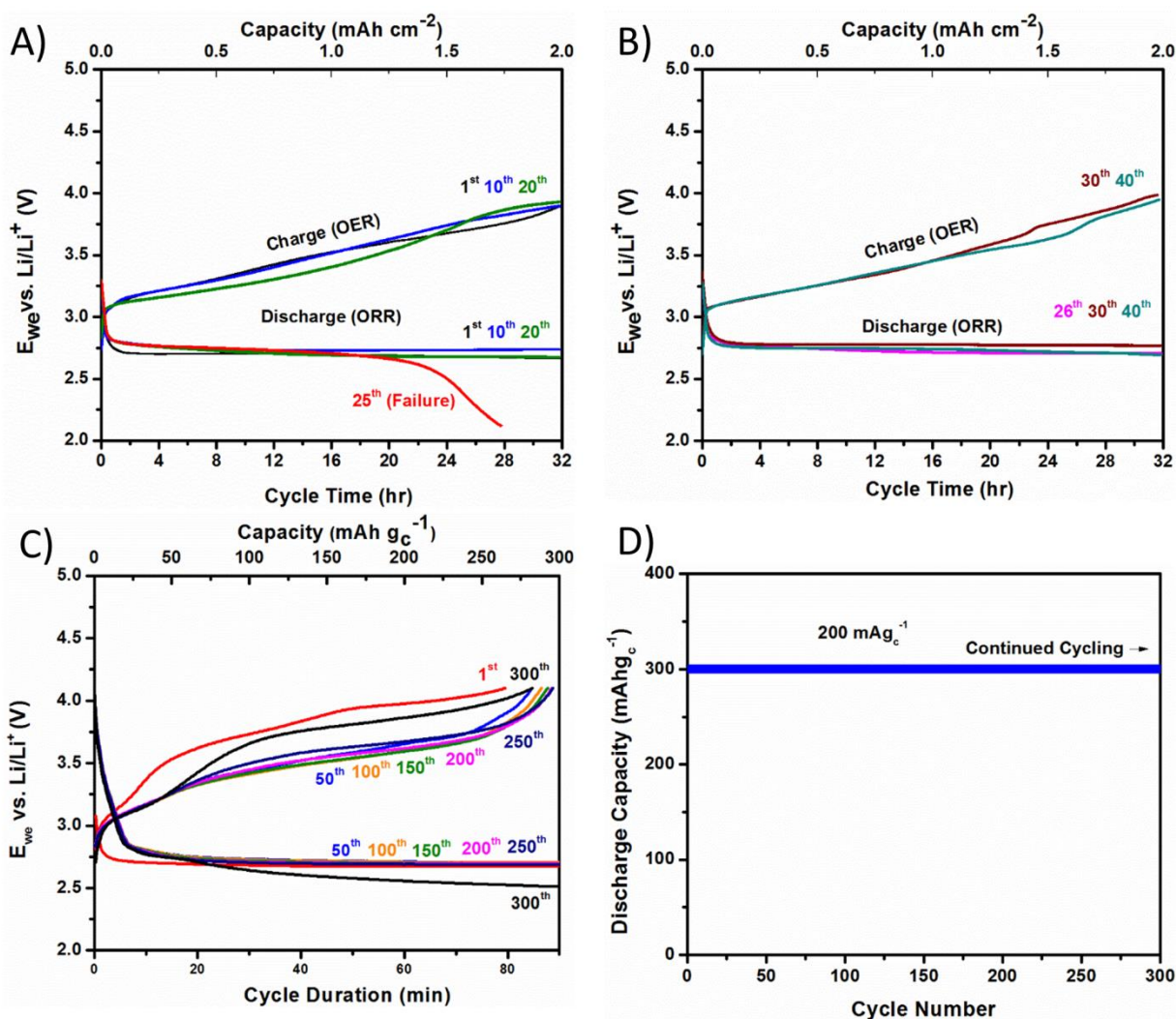


Figure 34: Galvanostatic cycle performance of MWCNT@Ru cathode. A) Overlay of select cycle profiles under capacity and voltage limited conditions (2,130 mAh g⁻¹ carbon with a current of 70 mA g⁻¹ carbon). Profile shows stable cycling until failure during the 25th discharge due to voltage limitation. B) Reclosing the cathode in a new cell resulted in recovery of the cycle profile after the 25th discharge, as shown on the right, for up to 40 cycles. C) Cycle profile overlay for cathode cycled at higher current density. D) Discharge capacity for cathode cycled in C is maintained for over 300 cycles.

a reversible Li-O₂ cathode.

This extended duration cycling stability was tested galvanostatically with currents of 70-150 mA g⁻¹_{carbon} with fixed discharge capacities of 2,100-2,500 mA h g⁻¹_{carbon} (>2 mA h/cm² and 580-1,000 mA h g⁻¹_{electrode}) which is a significant fraction (~25%) of the total cathode capacity at these rates. The pristine MWCNT cathode demonstrated limited stability, unable to cycle with a total cell current of 20 μA with 0.1 M LiTFSI/DMSO reproducibly for more than 10 cycles before irreversibly exceeding the cycling voltage window (2-4.0 V). However, under similar conditions (specifically: 2,130 mA h g⁻¹_{carbon}, 588 mA h g⁻¹_{electrode}, 2 mA h cm⁻²_{electrode} capacity at a rate of 70 mA g⁻¹_{carbon}) the Ru-decorated cathode demonstrated a healthy cycle profile for more than 24 cycles until the voltage of the discharge exceeded the 2 V lower limit without reaching the capacity limit. Mass spectroscopy is frequently used as a mode of tracking formation and evolution of Li₂CO₃ as a

result of parasitic side reactions in Li-O₂ cells^[15,19,84] which have been shown to evolve CO₂ (g) during charge. Prior to failure, the cell showed no early signs of performance degradation, so we collected a mass spectrum of the cell headspace after the prolonged cycling, as

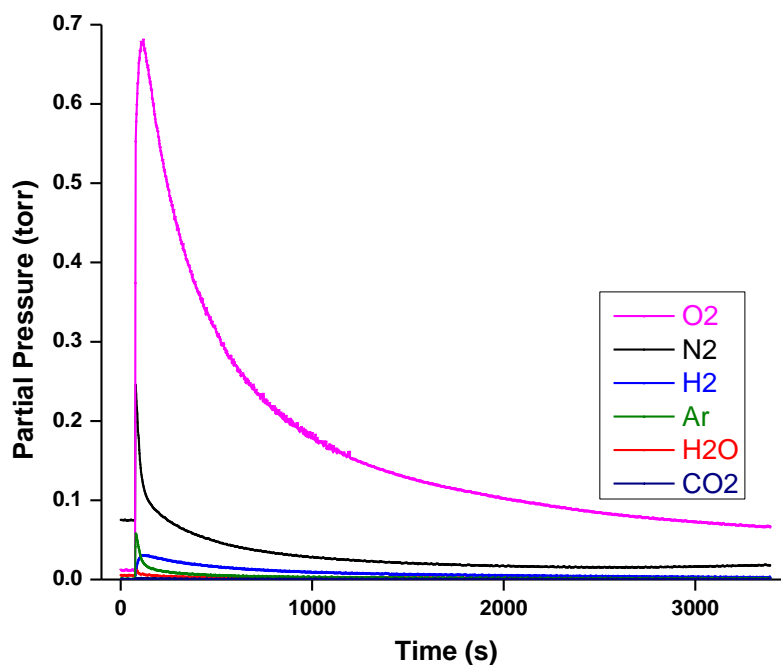


Figure 35: Mass spectroscopy headspace sampling of MWCNT/Ru cell after 25th discharge (premature cell failure requiring anode replacement). The primary component is O₂; and there are barely detectable levels of CO₂ which in previous works has been used to indicate Li₂CO₃ the presence on the cathode as a result of parasitic side reactions.^[15] The lack of a clear reason for failure encouraged us to replace the anode and resume testing.

shown in **Figure 35**, in an attempt to probe the cause of cell failure. Remarkably, oxygen was still the dominant gaseous species in the cell and negligible amounts of CO₂ or H₂O were detected. The cell was then reopened inside the glove box and only the anode was replaced. Surprisingly, after reclosing the cell and continuing the galvanostatic cycling program, the cathode showed full recovery of the voltage profile and continued cycling with the same healthy voltage profile observed before cell failure, as shown in Figure 34b. The consistency of the voltage profile before and after anode replacement strongly suggests similar surface chemistry/electrochemistry. Similar behavior was also demonstrated with the previously discussed cathode cycled to a lower capacity at higher currents from Figure 34c/d. After closing the previously cycled cathode in a new cell without air exposure, the voltage profile showed recovery and the cathode recovered cycling under the same conditions of Figure 34a. These results, when taken together, strongly suggest that in our cells the limiting factor for cell lifetime is the anode/electrolyte interface and not the cathode.

4.4 Stable Non-Li₂O₂ Interfacial Layer

After another prolonged cycling period to more than 40 total cycles without additional signs of failure, we reopened the cell cycled over extended durations inside the glove box and loaded it via high vacuum transfer directly to the XPS using our integrated system. Semi in-situ XPS characterization of Li-air cathodes directly from realistic cells, and in particular direct comparisons of discharged and charged cathodes, is uncommon in the literature but is important for understanding the chemistry of surface layers developed during operation. We identify a thin solid electrolyte interphase formed during the first discharge/charge cycle, which appears to be subsequently very stable in terms of chemistry and morphology upon charging, as well as after extensive cycling in a limited capacity window.

We first made a comparative XPS analysis of an ALD Ru-decorated MWCNT sponge after the first discharge and the first charge. **Figure 35** shows the survey scans from 0-650 eV, which demonstrate the relative change in the quantities of oxygen and lithium. As expected, the charging process liberates a majority of the oxygen and lithium from the cathode, though a significant quantity of oxygen remains

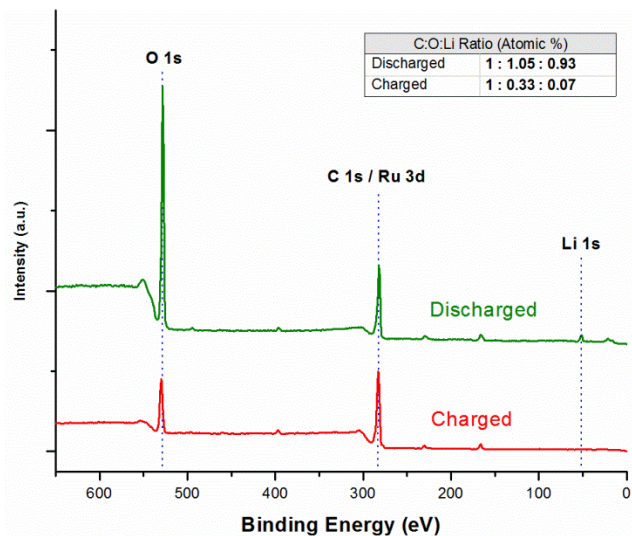


Figure 35: Survey scans of the first discharge and charge of a Ru functionalized MWCNT cathode. The spectra are normalized so that the C 1s peaks have the same intensity, highlighting the relative change of the O and Li peaks. The peak heights are proportional to the total amount of each element. Inset: C : O : Li atomic ratios calculated using photoelectron cross sections.

present after charge when compared to the pristine cathode. The high-resolution spectra in **Figure 36** help elucidate the chemical identity of both the discharge products and the residual surface film. The discharged C 1s/ Ru 3d spectrum (36a) demonstrates the near-complete

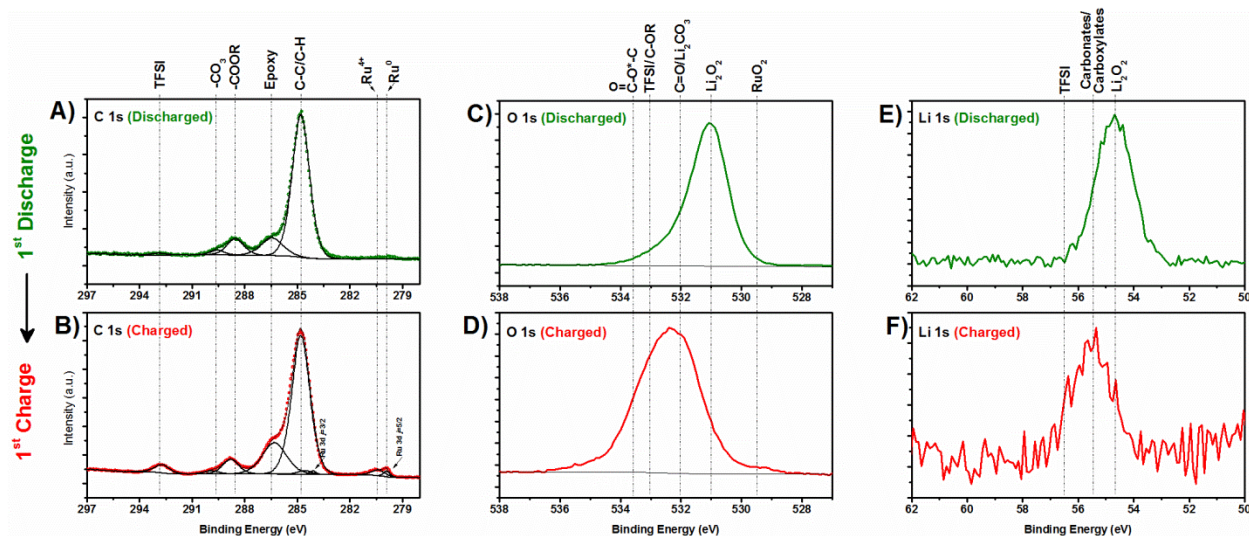


Figure 36: A systematic comparison of the high resolution C 1s/ Ru 3d (a,b), O 1s (c,d), and Li 1s (e,f) XPS peak regions for the first discharge and charge of a Ru functionalized cathode. All spectra are normalized to the same arbitrary peak intensity to highlight changes in peak shape and location, though the absolute quantities change significantly (Fig 35 inset). Peak locations for (a) and (b) can be found in the text. Some peaks in (b) shift slightly relative to (a), possibly due to small amounts of differential charging. Explicit peak fitting was not attempted for (c), (d), (e), and (f), though locations of possible species are highlighted, with locations based on either measured standards (LiTFSI, Li₂O₂) or literature values (all others).^[85,117,118]

suppression of the Ru signal at 280eV, which implies that the cathode has been covered in a thick layer of discharge products. The primary intensity of the discharged O 1s (531 eV) and the Li 1s (54.6 eV) spectra (Figure 36c and 36e) match extremely well with the locations expected for Li_2O_2 , as compared to both literature values^[85] and our own measurements of a Li_2O_2 commercial powder standard, shown in **Figure 37**. This confirms that the dominant discharge product is Li_2O_2 . However, the C 1s spectrum confirms the formation of a variety of C-containing side products. The primary peak at 284.8 eV contains signal from the nanotubes, but is dominated by non- sp^2 carbon and hydrocarbons as is clear from the symmetry of the peak, which points to the presence of a polymer-like material interspersed with the Li_2O_2 . The C 1s also demonstrates the formation of small amount of lithium carboxylates (HCO_2Li or $\text{CH}_3\text{CO}_2\text{Li}$) and carbonates (Li_2CO_3) upon first discharge, which are possibly due to the reaction of residual amorphous carbon and hydrocarbons on the surface of the pristine CNTs.^[29] This process would be expected to be self-limiting, and indeed the amounts of these products change only slightly with further cycling. Continued growth of this type of Li-O₂ cathode/electrolyte interlayer, as observed in a recent work^[86], could be attributed to cell operation outside of the voltage stability

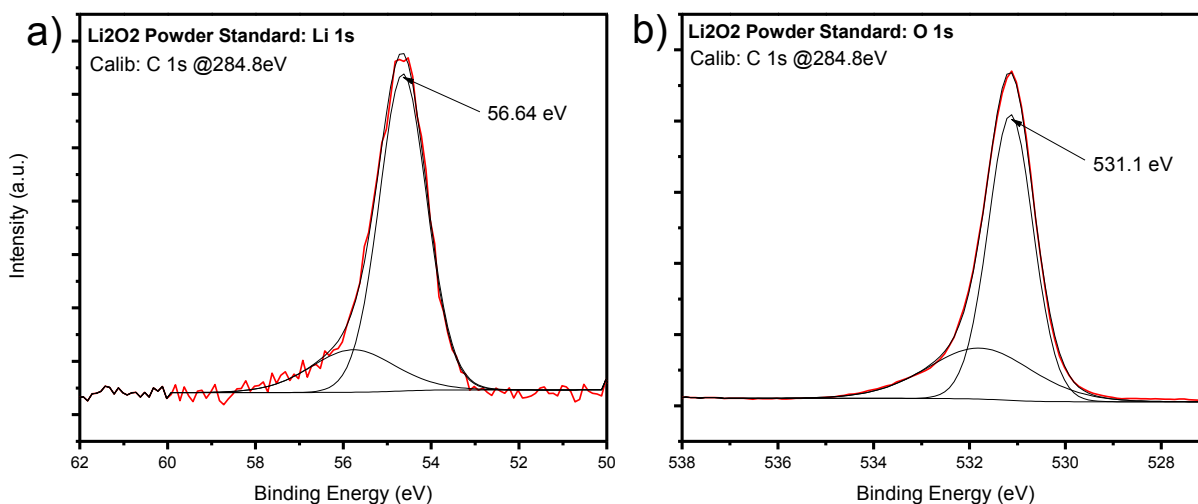


Figure 37: High resolution XPS spectra of the (a) Li 1s and (b) O 1s of commercially available Li_2O_2 powder. The spectra are calibrated by placing the C 1s hydrocarbon peak at 284.8 eV.

window of the cathode/electrolyte, leading to parasitic side reactions and decomposition products. While these cycling conditions will initially yield higher capacity, long term cycling stability is compromised by continuous growth and evolution of the SEI layer. We demonstrate that achieving long duration cycling and a stable cathode/electrolyte interface depends on selection of an appropriate cycle capacity and potential limitations.

After the first charge, the intensities of the O 1s (Figure 36d) and the Li 1s (Figure 36f) peaks near the locations associated with Li_2O_2 are strongly suppressed, indicating the expected charge process. The small amount of remaining Li appears to be associated with carbonate/carboxylate species, which cannot be decomposed within the typical charging potential of our cathode, as well as residual LiTFSI salt. The O 1s spectrum reveals a wide peak spread over binding energies associated with a variety of possible carbon-based moieties, but the broadness of these features precludes reliable peak fitting. We anticipate most of the residual oxygen to be bound within the polymeric surface film or involved in functionalization of the CNT surface. The higher detected amount of TFSI on the cathode after charge as indicated in Figure 36(a-b), is attributed to stronger electroadsorption of the anion when higher potential was applied on the cathode upon charging the battery. The C 1s/ Ru 3d (Figure 38) spectrum shows the partial recovery of the Ru signal, which demonstrates that either the catalyst

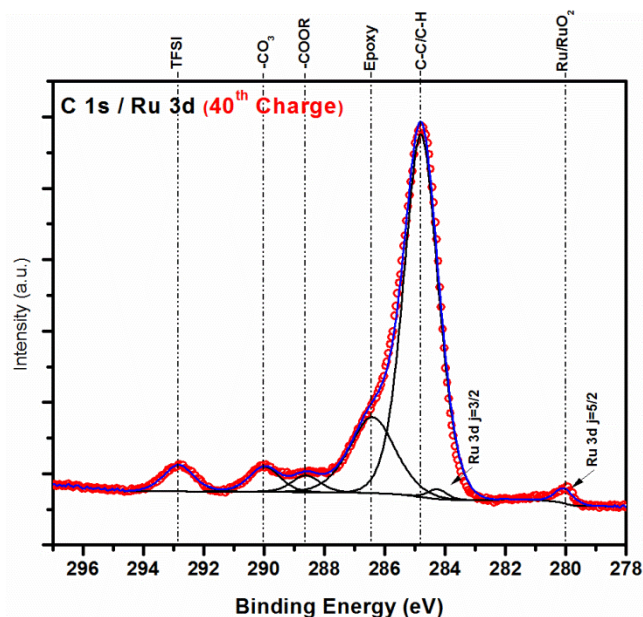


Figure 38: High resolution C 1s / Ru 3d spectrum of a Ru functionalized cathode after the 40th charge cycle (see Figure 34). The charge spectrum from a different cathode after a single charge (Figure 36b) is almost identical. The Ru peaks can no longer be clearly resolved into metallic and oxide components, but the primary Ru 3d j=5/2 intensity centered at 280eV suggests the catalyst is still at least partially metallic.

particles are partially uncovered by the charging reaction or the thickness of any products covering them is thinned. However, the Ru signal is still dramatically suppressed relative to the as-synthesized cathode, suggesting the continuing presence of a thin SEI-type layer. Considering that the fractional Ru photoelectron intensity in Figure 36b is reduced by a factor R of approximately 80 relative to Figure 32c and that the inelastic mean free path λ of Ru 3d photoelectrons in Li, O and C rich materials (using Li_2CO_3 as a model material) is approximately $3.1\text{nm}^{[87]}$, a rough calculation would predict an average overlayer thickness d of $d = \lambda \ln(R) \approx 13\text{nm}^{[88]}$.

This observation is supported by TEM images of MWCNT/Ru cathodes in various stages of cell cycling as presented in **Figure 39** and **Figure 40**. A thin SEI layer (typically 5-15 nm in thickness) with the underlying Ru catalyst still attached to the MWCNT is observed after the 1st discharge (Figure 40), the 1st charge, and even after 40 cycles (Figure 39). Despite this, the low overpotential observed in the charging process (and in all subsequent charging cycles) implies that the Ru particle surface is still available to partake in electrochemical reactions.

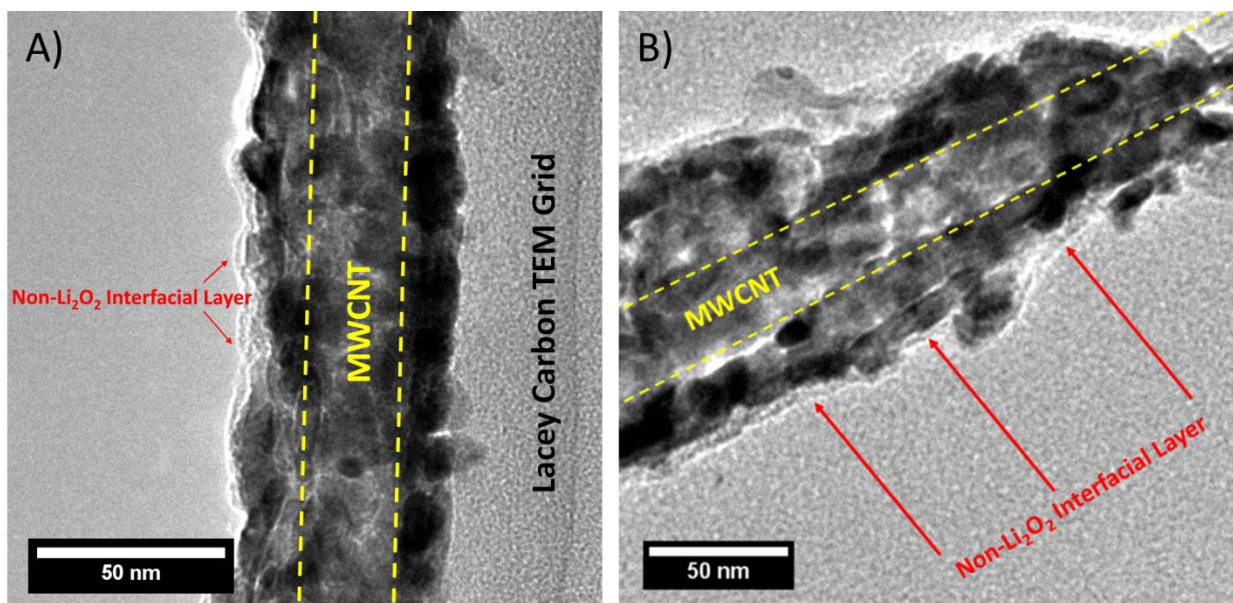


Figure 39: TEM image of the MWCNT-Ru cathode after the 1st charge (left) and the 40th charge cycle (right) showing the surface film remaining on the cathode with underlying and intact Ru catalyst.

Conjugation of the XPS and TEM data strongly suggest that the surface film is permeable or porous, allowing the diffusion of dissolved species to reach the cathode surface during operation while still suppressing the CNT and Ru XPS signals during characterization. The nanoparticles of Li_2O_2 tends to form in the proximity of the Ru particles (Figure 40). The other features of the charged C 1s spectrum are very similar to that of the discharged with the exception of a

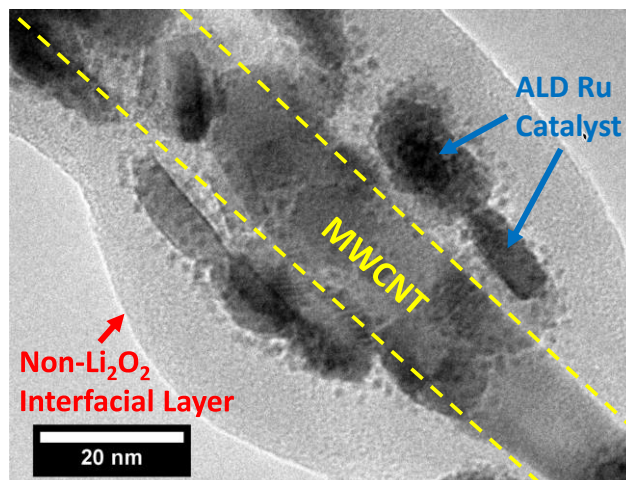


Figure 40: TEM image of MWCNT-Ru cathode after 1st discharge showing interfacial layer and the presence of ~1.5nm spherically shaped deposited particles, mainly on the Ru surface. It seems likely that these particles are primarily composed of Li_2O_2 based on the XPS analysis because the only significant difference between the spectra for charged and discharged cathodes can be attributed to the presence of Li_2O_2 . Though those deposited species disappear upon charging of the cathode (Figure 39b) the amorphous SEI stays on its surface without noticeable change in morphology (e.g. or composition as found by XPS)

moderate increase in epoxy-type groups. Examination of the S 2p and F 1s peak regions (Figure 41) reveals a negligible amount of decomposition of the TFSI anion.

In order to confirm the stability of this surface film, we also examined the cathode from

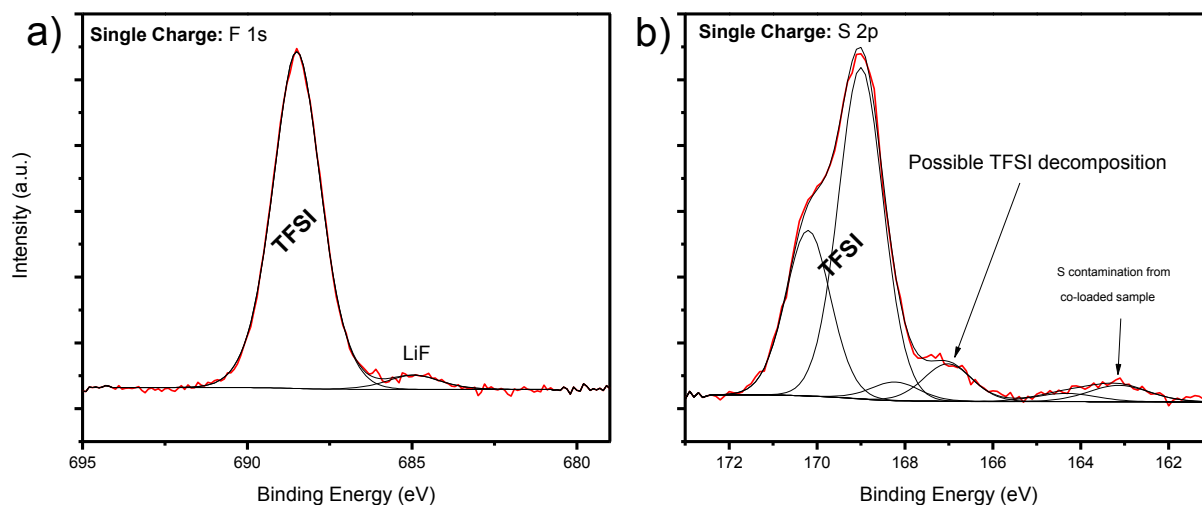


Figure 41: High resolution F 1s and S 2p spectra from a Ru functionalized MWCNT cathode after a single discharge-charge cycle. The F 1s shows a small amount of formed LiF, possibly from TFSI decomposition. This amount of LiF was consistent across essentially all samples tested. The S 2p shows a peak at a slightly lower binding energy than the main TFSI peak, which would nominally be associated with a more reduced sulfur species. This feature is again consistently observed and does not grow after 40 cycles. The S intensity at ~163 eV was a feature observed on all samples loaded into the XPS during a particular time, and has been identified as slight contamination from an unrelated outgassing S loaded sample stored in the same vacuum chamber.

Figure 34(a-b). The high-res C 1s spectrum of this cathode after 40 cycles is shown in Figure 38. It is apparent that the ratio of intensities of the Ru 3d ($j=5/2$) peak to the main C 1s peak is essentially identical to that observed in a cathode after only a single complete cycle (Figure 36b). This implies that the thickness and morphology of the surface layer is essentially unchanged from the first cycle. If the film was progressively growing through the consumption of the electrolyte or the CNT support, one might expect the complete suppression of the Ru signal or a dramatic increase in side products. In fact, the remaining components of the C 1s spectrum are strikingly similar to those after a single cycle, still showing a dominant hydrocarbon/C-C peak at 284.8 eV and a series of small peaks associated with oxygen bonding, including carboxylates at 288.6 eV and carbonates at 290 eV. The amount of carbonate (approx. 4% of all C 1s signal) has increased somewhat relative to the single cycle cathode (approx. 1% of all C 1s signal), but this increase is far below what is typically observed in systems where the electrolyte or cathode is unstable due to either the chemical nature of the carbon or the cycling conditions.^[29,86]

4.5 Conclusions

Starting with a versatile, self-standing and robust multi-walled carbon nanotube sponge substrate, we investigated the catalytic enhancements in OER/ORR activity generated by ALD decoration with nanoparticles of Ru and RuO₂, directly evaluating the two chemistries with the same electrochemical Li-O₂ test platform. Initial electrochemical characterization revealed that ruthenium metal ALD yielded the more active electrocatalyst, reducing OER/ORR overpotentials and significantly improving cyclability, even at high capacities. Cycling studies of the MWCNT/Ru system showed excellent stability over long discharge/charge durations and cell failure was found to be related to other cell components. In-situ XPS characterization, and HRTEM images indicate that these composite cathodes exhibit formation of a stable SEI on the

cathode, primarily occurring during the first few cycles and without significant evolution after long term cycling. This work also emphasizes the generally unexploited promise of ALD for selective passivation and catalysis in next generation battery electrodes.

Chapter 5: Dimethyl Sulfoxide as a Stable Electrolyte Solvent for Li-O₂ Research

5.1 Introduction

Both experimental and theoretical works surveying various solvent candidates for Li-O₂ electrolytes have struggled to find an appropriate solvent for the study and development of rechargeable Li-O₂ batteries. Carbonate-based electrolytes used in early Li-O₂ works were later found to be unstable against ORR reaction intermediates and form Li-carbonate species instead of the lithium peroxides or oxides expected for healthy ORR.^[15,34,89,90] Polyether solvents were reported to degrade in the presence of O₂, Li⁺ and reduced oxygen either by auto-oxidation^[91], or electro-oxidation.^[91-93] One of the other widely used electrolyte solvents for Li-O₂ battery research is dimethyl sulfoxide (DMSO); however, due to multiple contradicting reports regarding its chemical stability on the surface of Li-O₂ cathodes, there was a strong need to carefully assess its stability, despite our previous success with Ru-based cathodes in DMSO-based electrolyte, before continuing to use it in our Li-O₂ R&D.

Extensive research has focused on the stability of DMSO as a medium for oxygen electrochemistry. Laoire et al. examined DMSO for Li-O₂ batteries, suggesting it as a promising solvent for stabilization of reduced oxygen species during ORR.^[90] Various groups then demonstrated cells operating with DMSO-based electrolytes, leading to improvements in cycle life^[90] and the stability of the cathode^[82]; however, recent publications suggested a mechanism for chemical or anodic oxidation of DMSO in Li-O₂ operating cells under certain conditions that

can cause detectable solvent decomposition.^[21,94] Furthermore, two separate reports suggested either spontaneous chemical degradation of Li_2O_2 into carbonate when in contact with DMSO (monitored by XPS)^[95], or complete decomposition of Li_2O_2 to LiOH conjugated with extensive oxidation of DMSO to dimethyl sulfone (DMSO_2 detected by FTIR)^[76], and concluded that DMSO is not an appropriate solvent for studying Li-O_2 batteries with long discharge durations due to its chemical instability on the surface of Li_2O_2 , bringing into question the relevancy of earlier reports involving more practical systems. We will further address the conditions presented in these two reports and present contradicting results under robust conditions for monitoring Li_2O_2 degradation or DMSO oxidation.

Indeed, concerns regarding DMSO stability in the presence of superoxide ions goes back to reports published by Sawyer and coworkers^[96,97], suggesting possible oxidation of DMSO to DMSO_2 in a solution containing tetraethylammonium perchlorate (TEAP) salt. However, this oxidation was not suggested to involve hydrogen abstraction from DMSO or a direct nucleophilic attack by O_2^- on the sulfur atom of the S=O bond, but rather involved an initial hydrogen abstraction from the alkylammonium ion and was tested in relatively high water content ($>500\text{ppm H}_2\text{O}$), which can also serve as a possible source of protons. The nucleophilic attack suggested by Sawyer and coworkers therefore occurs by hydroperoxy ions and not O_2^- . Anodic oxidation of DMSO to DMSO_2 was also found possible by Krtil et al.^[98] using Li salts in DMSO, but with an extremely high concentration of water ($\sim 0.04\text{M}$) compared to properly dehydrated Li-O_2 systems. This work was recently validated in more controlled environment by Calvo and coworkers^[94], reporting appearance of DMSO_2 at potentials above 4.2 Vs $\text{Li}\backslash\text{Li}^+$ via processes also hypothesized to involve in consumption of trace water from the electrolyte.

All of the above work used FTIR for characterization, and the peak of the symmetric SO_2 stretch ($\nu_s\text{SO}_2$) at 1142 cm^{-1} was considered a marker for the presence of DMSO_2 . The limit of detection (LOD) of the FTIR system for the presence of DMSO_2 in the solvent has not been reported in these works, making it difficult to quantitatively evaluate the extent of the reported oxidation. This calibration is critical to determine if the observed peaks indicate continuous oxidation of the solvent or only a minor parasitic reaction that may stop (i.e. after ppm level H_2O is fully consumed), having no significant effect on cell performance and cyclability. Furthermore, the observed peaks in the $1140\text{-}1145\text{cm}^{-1}$ range are not exclusively indicative of DMSO_2 , as shown in recent works done with in-operando Raman spectroscopy^[99] and surface enhanced Raman^[100] (SERS), which attribute the peak at $\sim 1140\text{ cm}^{-1}$ to the formation of LiO_2 on the surface of the cathode rather than the oxidation of DMSO to DMSO_2 . Indeed, these Raman experiments did not suggest DMSO oxidation; however, the exposure time of DMSO to Li_2O_2 and superoxide ions in these reports was relatively short.^[76]

In order to deconvolute the question of DMSO stability on the Li_2O_2 surface in operating Li- O_2 battery, our collaborators demonstrate a computational exploration of the chemical stability of the $\text{Li}_2\text{O}_2/\text{DMSO}$ interface using density functional theory (DFT), and propose a novel reaction pathway supported by calculated activation energies. Furthermore, we carefully address the previously reported conditions for chemical decomposition of DMSO by using a specialized UHV integrated system for sample preparation and transfer to XPS without exposure to air or moisture for analysis of Li_2O_2 aged in DMSO. FTIR and Raman spectra were collected for each chemical species in our report and previous reports, in addition to the limit of detection (LOD) of our FTIR and Raman systems for the detection of DMSO_2 . We also investigate DMSO stability against oxidation during ORR or anodic oxidation under operating Li- O_2 battery

conditions. The Li_2O_2 aged in DMSO showed no definitive chemical changes with time, and DMSO_2 could not be detected with FTIR, even after 7 months. Furthermore, mesoporous core-shell CNT@Pt cathodes synthesized via atomic layer deposition enabled us to demonstrate the stability of DMSO during cycling for over 4 months of cell operation, with a round-trip cycle duration of 80 hours and with more than 45 cycles before disassembling the cell for spectroscopic characterization.

Through a collaborative effort with our colleagues Dr. Kevin Leung and Dr. Nitin Kumar at Sandia National Labs in Albuquerque, NM, we find that DMSO is highly stable on the surface of Li_2O_2 , both theoretically and experimentally, as will be discussed in subsequent sections.

5.2 Experimental Methods

DMSO₂ as a Marker of DMSO Oxidation

Previous reports used FTIR for detection of SO_2 stretching, suggesting this stretching indicates the oxidation of DMSO. It has become accepted to use KO_2 as a source for superoxide in DMSO, and to chemically monitor the degree of oxidation of the solvent, as indicated by the appearance of stretching peak at 1142cm^{-1} using Raman or FTIR. However, as presented in Figure 42, the Raman spectrum of pristine KO_2 shows a strong peak at 1142cm^{-1} (which can be attributed to $\text{O}=\text{O}$ stretching), strongly implying that KO_2 is not a suitable source of superoxide in a solution where DMSO_2 is to be measured at any concentration. This observation agrees well with FTIR reports of pristine KO_2 and the literature value of $\nu_{\text{O}=\text{O}}=1145\text{ cm}^{-1}$.^[99-101] It seems like the only appropriate way to use KO_2 in order to test oxidation of DMSO to DMSO_2 by stretching spectroscopy is to use K^{18}O_2 in which the $\nu_{\text{O}=\text{O}}$ is shifted to 1118 cm^{-1} .^[101] The decomposition of KO_2 under the laser also manifested additional peaks suggesting that the O-H peak previously reported by others as LiOH ^[76] could be attributed to decomposition of KO_2 to KOH and not

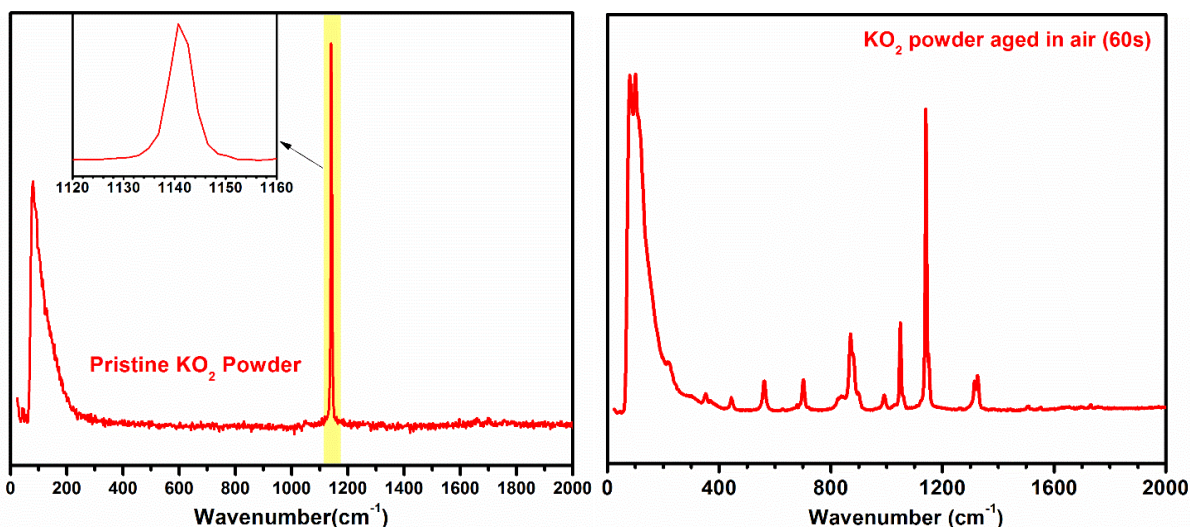


Figure 42: Raman spectrum of pristine KO_2 powder (left) showing strong peak at 1142cm^{-1} which can be attributed to the O=O stretch. KO_2 powder aged in air shows evolution of multiple peaks.

necessarily to Li_2O_2 decomposition to LiOH . We first calibrated the FTIR to determine the limit of detection (LOD) for DMSO_2 in DMSO. **Figure 43** shows that the SO_2 peak will manifest itself even at concentration below 500ppm, implying that FTIR will sense the presence of SO_2 at very low concentrations ($\text{LOD} < 7\text{mM}$). Figure 43 also shows the same calibration process

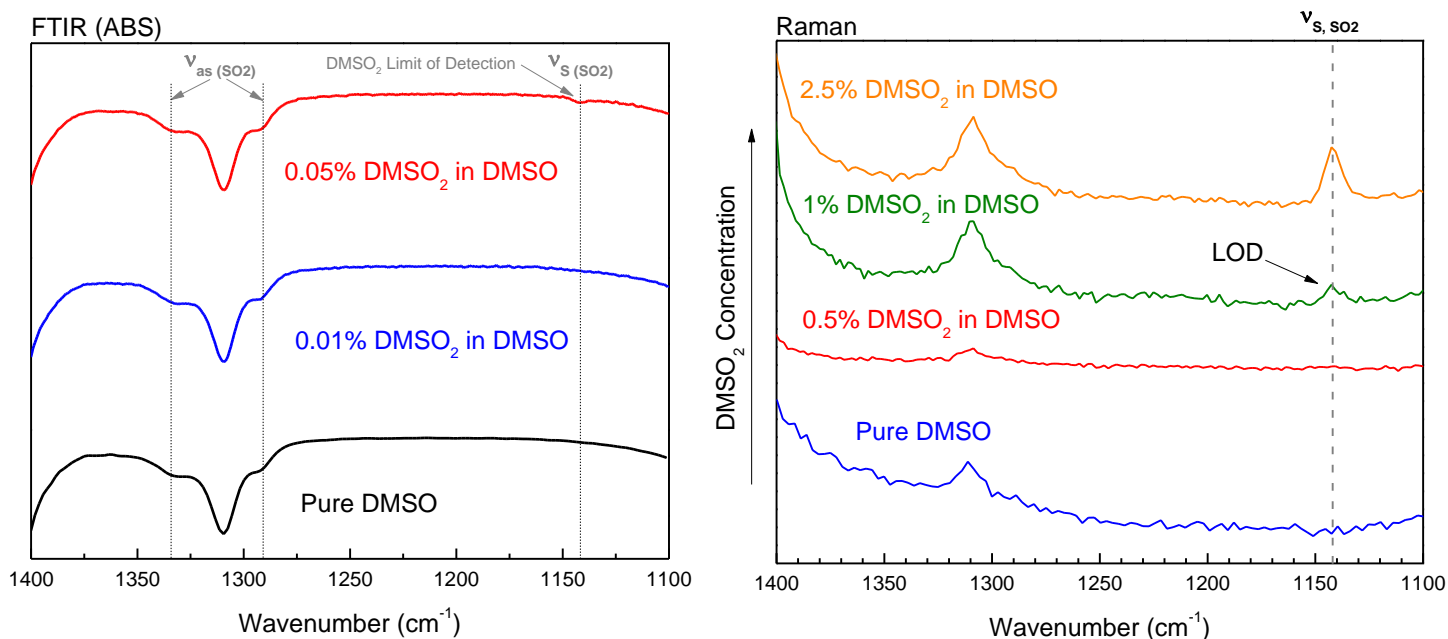


Figure 43: FTIR and Raman spectra for limit of detection of mol% DMSO_2 in DMSO. The measured limit of detection is ~ 0.05 mol% for FTIR and 1% for Raman as indicated by the onset of the symmetric SO_2 stretch at 1142cm^{-1} .

performed with Raman, showing that the LOD of Raman is higher at about 1% (140mM), suggesting that Raman can confirm or rule out extensive oxidation of DMSO to DMSO₂.

To test possible oxidation of DMSO in an operating Li-O₂ cell, we discharged a MWCNT cathode to 3000mAhg⁻¹ at 100mA g⁻¹, let it rest for 14 days inside the

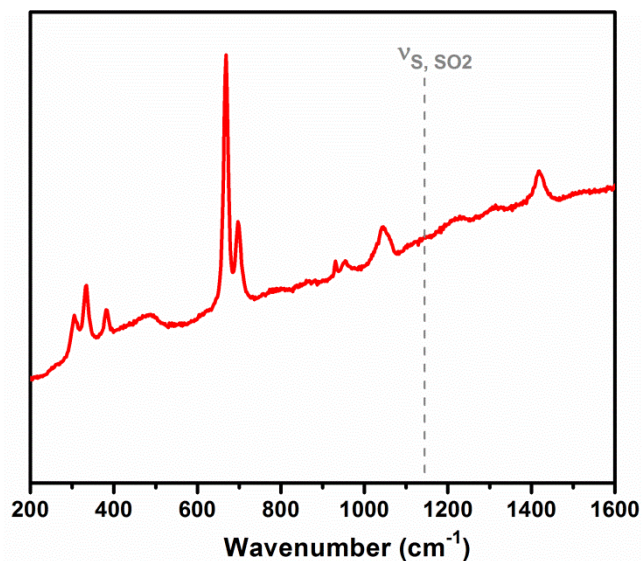


Figure 44: Raman spectrum of electrolyte after 14 days of rest within a discharged cell. No signal at 1142 cm⁻¹ suggests oxidation of DMSO is below detection limits or not present.

glove box, and opened the cell inside the glove box to collect a sample of the electrolyte for Raman testing. As presented in **Figure 44**, there is no signal for symmetric SO₂ stretch (1142cm⁻¹) in the electrolyte despite an expected molar concentration >2% according to degradation suggested in previous report.^[76] We tested the solubility of DMSO₂ in DMSO to confirm that this proposed decomposition product should be detected in solution, if present, and found a saturation limit of 20 mol% of DMSO₂ in DMSO.

Long Term Stability of DMSO Against Oxidation in an Operational Li-O₂ Cell

In a practical Li-O₂ cell the stability needs to be tested on a very long term, as pointed out by Shao-Horn and coworkers.^[76] However, the majority of the cathodes used in Li-O₂ reports are either carbon cathodes which demonstrate high gravimetric capacity but limited cycle life^[19] (~15 or fewer high capacity cycles due to chemical and electrochemical instability of the carbon), or porous cathodes made of gold or TiC that undergoes discharge processes of relatively short times^[82,102] (less than 2 hours for the reports on the porous gold electrodes by Bruce et al.). Additionally, the anodic instability of DMSO at potential higher than 4-4.3V^[21,94] vs. Li in the

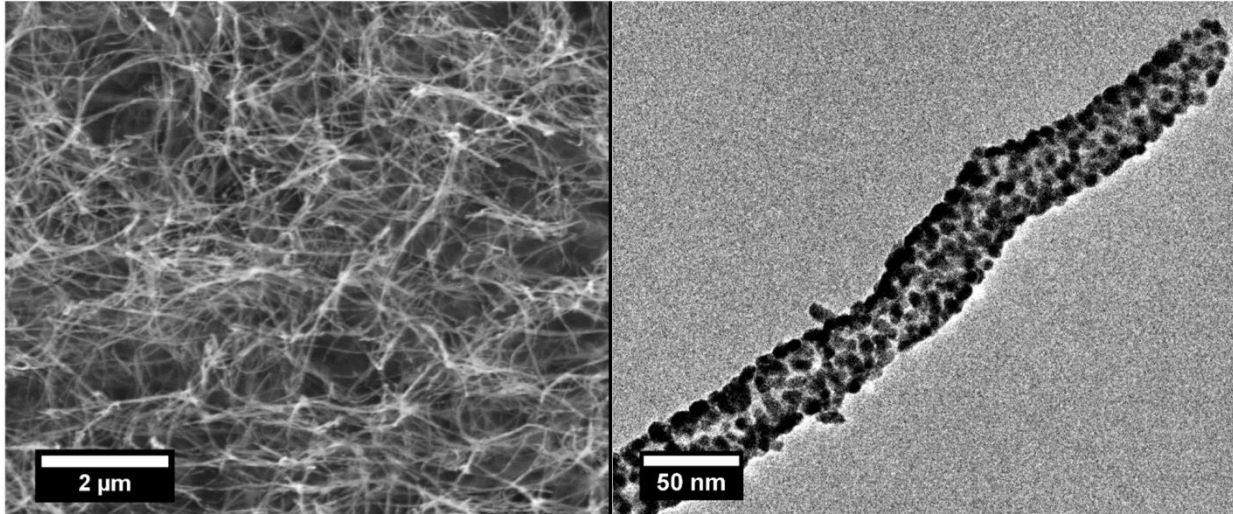


Figure 45: SEM (left) and TEM (right) images of ALD-Pt coated carbon nanotube sponge used as a cathode for extensive cycling to probe DMSO stability over long cycles (80 hrs round trip)

presence of O_2 and H_2O (even trace amounts)^[94] was reported to manifest $DMSO_2$ in the electrolyte upon cycling, making it difficult to isolate whether detected oxidation took place on $Li_2O_2/DMSO$ interface upon prolonged exposure or by anodic oxidation of DMSO at high potentials. In order to fabricate Li- O_2 cathode that will enable both long discharge and extended

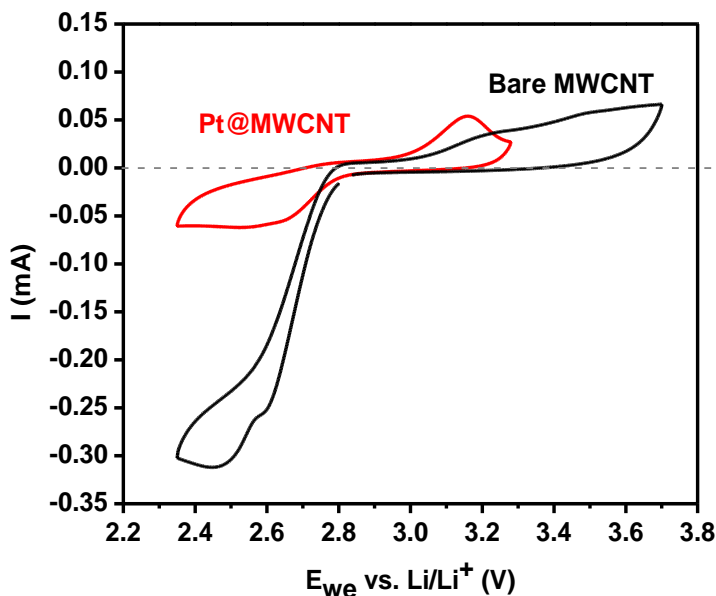


Figure 46: Cyclic voltammetry of pristine sponge cathode (1st cycle shown) compared to CNT@Pt cathode (fourth cycle shown). As obtained, the onset potentials for ORR are higher for the catalyst-loaded cathodes, suggesting enhanced activity which agrees well with the report on catalytic trends for ORR.^[61] The more prominent improvement in activity is observed during the oxygen evolution reaction, with significant increases in current obtained at much lower onset potential as compared to the pristine MWCNT.

cycle life, we synthesized core-shell CNT@Pt cathode by atomic layer deposition of Pt on self-standing CNT. The structure of the CNT@Pt cathode is presented in TEM and SEM images in **Figure 45**.

This cathode enabled us to test the long term stability of DMSO, toward oxidation, in an operating Li- O_2 cell. The cyclic

voltammetry (CV) response of the bare sponge and the Pt decorated MWCNT cathodes are presented in **Figure 46**. The Pt shell enabled pronounced catalytic activity for OER, hence significant amount of the discharge capacity could be recovered upon charge at voltages below the reported value for anodic oxidation of DMSO.^[94,98] Long term cycling stability of this system was tested via galvanostatic cycling with currents of $50 \text{ mA g}^{-1}_{\text{carbon}}$ with fixed discharge capacities of $2,000 \text{ mAh g}^{-1}_{\text{carbon}}$. This translates to a 40 hour discharge followed by a 4V voltage-limited charge step for more than 45 cycles. To our knowledge, this is one of the longest individual cycle durations reported in a study of a rechargeable Li-O₂ cathode. After this duration of cycling the cell was purged with Ar and disassembled inside the glove box, and a sample of electrolyte was taken for Raman and tested for presence of DMSO₂. If DMSO oxidation had taken place on the Li₂O₂ surface as previously suggested, the expected concentration of DMSO₂ should exceed 35 mol% after 4 months of operation. Yet, as presented in **Figure 47**, no DMSO₂ was detected even after these extremely long cycle times, strongly suggesting that the degree of oxidation of DMSO was below 1 mol% and had a negligible effect on battery cycling performance. For a comparison, a Raman spectrum of 20 mol% DMSO₂ in DMSO is also presented. In addition to the standard marker (1142 cm^{-1}), three other peaks which are characteristic of DMSO₂ were also observed (465 , 495 , and 763 cm^{-1}) in this comparison, but are absent from the CNT@Pt electrolyte.^[103]

The lowest potential for ORR in this

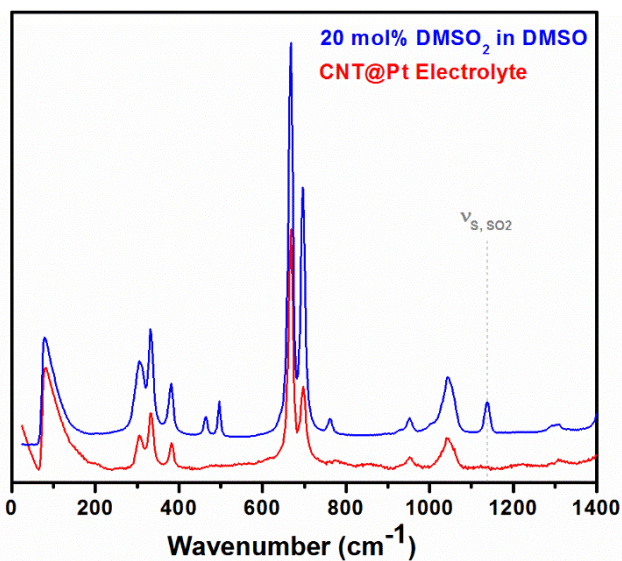


Figure 47: Raman spectrum of electrolyte sample from CNT@Pt showing no detectable levels of DMSO₂ (ν_{s, SO_2}). Shown with 20 mol% DMSO₂ in DMSO for comparison

cell was above 2.65V, higher than the potential reported to decompose DMSO on a microporous carbon cathode^[21], and the CNT@Pt is hypothesized to possess a significantly lower concentration of acidic functional group as compared to microporous carbon; hence, it is less likely to induce formation of the hydroperoxy ion that can oxidize DMSO through nucleophilic attack on sulfur in DMSO.^[21,94,96]

Li₂O₂ Decomposition

We have also examined the surface chemistry of Li₂O₂ in contact with DMSO using XPS, which should detect solid decomposition products even from minor, self-limiting surface reactions. A previous report showed the development of carbonates at the Li₂O₂-DMSO interface after 2 days, although no reaction mechanism was suggested. We soaked commercial Li₂O₂ powder in DMSO for over 2 months inside a glove box before removing a sample of powder, drying it under vacuum, and transferring it without atmospheric exposure to our

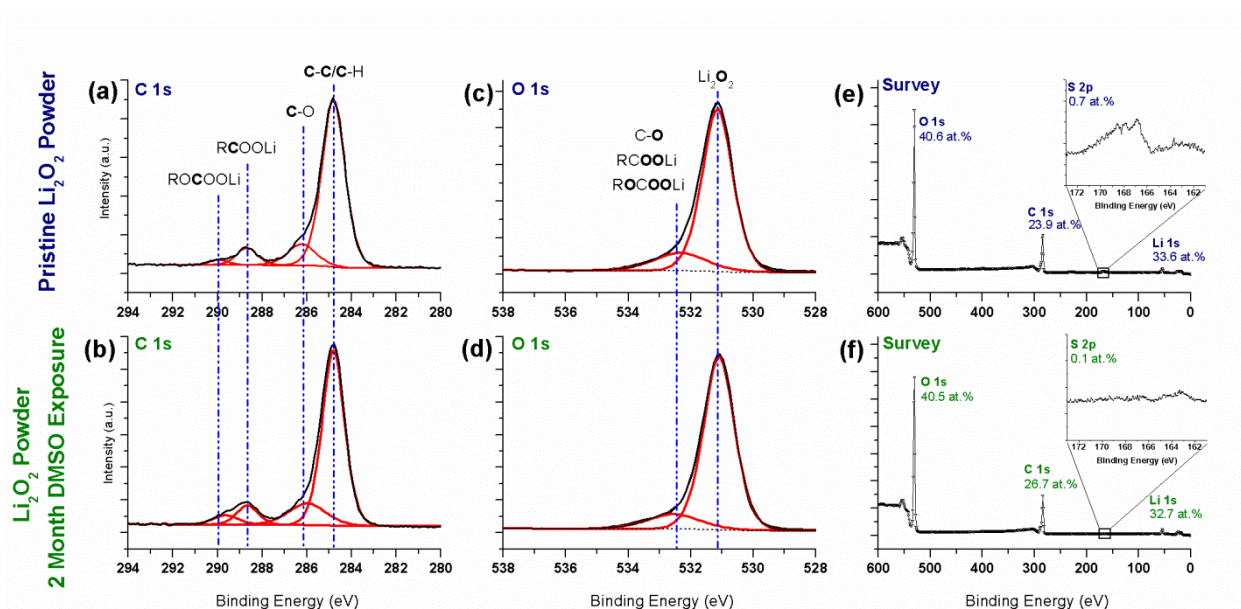


Figure 48: Figure 4. XPS spectra of as-received Li₂O₂ powder (a,c,e) and Li₂O₂ powder immersed in DMSO for over 2 months at room temperature (b,d,f). (a) and (b) compare the C 1s region with peak fitting, and (c) and (d) compare the O 1s region with peak fitting. (e) and (f) show a wide energy region (0- 600eV) which contains the O 1s, C 1s, S 2p, and Li 1s peaks. The numbers next to each peak reflects the calculated atomic percent composition of each sample. The insets show high resolution data from the S 2p regions. The y-scales of all graphs are normalized to approximately the same size to highlight differences in peak shape, except for the insets in (e) and (f) which have the same y-scale to highlight changes in quantity.

integrated XPS (Figure 7) for analysis. **Figure 48** compares the XPS signatures of the soaked powder and pristine (as received) Li_2O_2 powder transferred in the same manner. In general, the XPS results show no significant differences between the pristine and soaked powders, in support of the chemical stability of the Li_2O_2 -DMSO interface. The C 1s spectrum of the pristine powder (Figure 48a) shows the presence of a hydrocarbon layer, as well peaks associated with a small amount of lithium carbonates (290 eV) and carboxylates (288.7 eV), likely due to minor environmental exposure during manufacture or transport.^[104] These features are almost completely unchanged even after more than 2 months of exposure to DMSO except for a slight increase in the carbonate peak intensity. The degree of increase in carbonate intensity is barely at the threshold of significance when fitting errors and sample-to-sample variability are considered, and does not support the idea of a facile reaction between Li_2O_2 and DMSO as was previously reported. Another possibility is the reaction of Li_2O_2 with minute amounts of dissolved CO_2 in the DMSO. The O 1s spectrum of both samples (Figure 48c and 48d) are nearly identical and are consistent with Li_2O_2 , with a primary peak at 531.1 eV^[85] and a high binding energy tail containing contributions from various surface bound carbon-oxygen species.

XPS is unable to differentiate Li_2O_2 and LiOH due to their near-identical binding energies^[85], though subsequent XRD characterization of the soaked powder did not support the presence of LiOH or Li_2CO_3 (**Figure 49**). Another important element to examine for decomposition reactions is

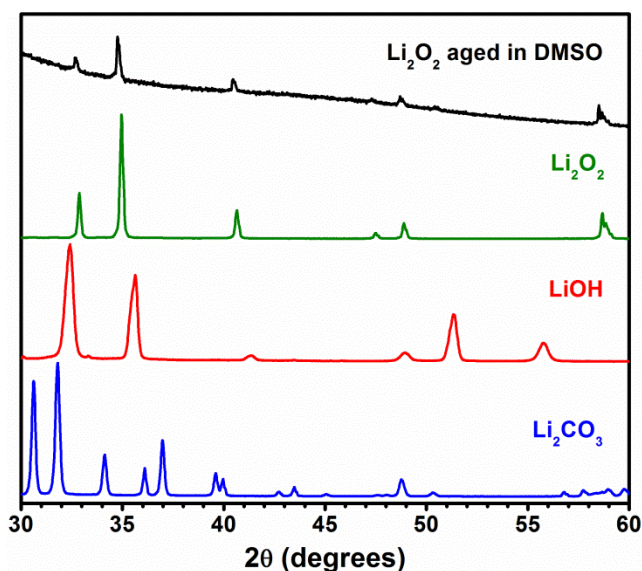


Figure 49: XRD of Li_2O_2 aged in DMSO for two months showing no indication of decomposition to LiOH or Li_2CO_3 .

sulfur (shown in Figure 48e and 48f insets).

The as-received Li_2O_2 powder was contaminated with a small amount of soluble S species (0.7 atomic percent). After 2 months, almost all of this sulfur was removed by soaking in DMSO and no new peaks developed. In particular, we saw no evidence for the formation of DMSO_2 , which would be expected to show a peak at

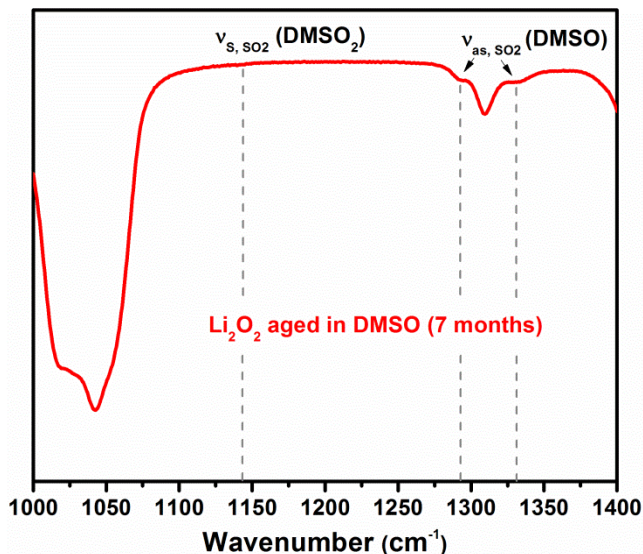


Figure 50: FTIR of Li_2O_2 aged in DMSO for seven months showing no indication of oxidation to DMSO_2 .

approximately 169 eV .^[105] Even if DMSO_2 was dissolved in the supporting DMSO, it would be expected to redeposit on the Li_2O_2 surface during drying. Taken together, these XPS measurements do not show any significant chemical changes which can be attributed to a decomposition reaction. DMSO from the same sample was also tested by FTIR and showed no oxidation even after 7 months, as shown in **Figure 50**.

Additionally, the conversion of Li_2O_2 to LiOH is expected to hinder the performance metrics of a Li-O_2 cell by halving the capacity and requiring a charge potential significantly higher than expected for OER of Li_2O_2 .^[15,34,106] In an attempt to observe these effects, we closed a Li-O_2 cell with CNT cathode, discharged to a capacity of $3,000\text{mAh g}^{-1}$, and let it stand for 100

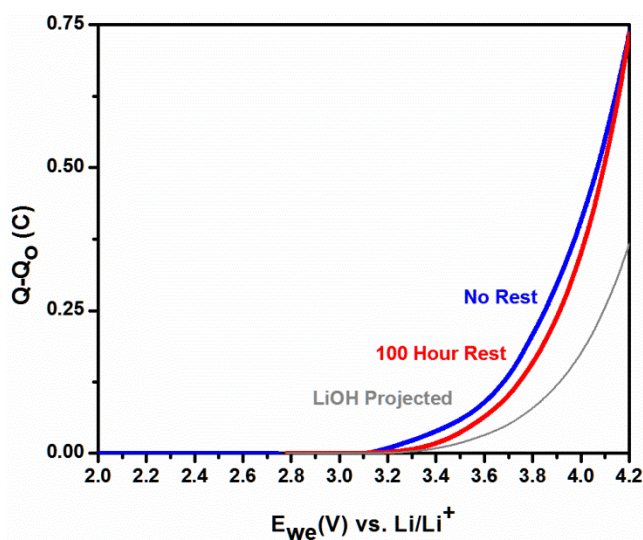


Figure 51: Plot of capacity vs. voltage during linear voltage scan. The blue curve represents a cell that had no rest time between the end of discharge and this charge sweep. The red curve represents a cell that rested for 100 hours before the charge sweep.

hours in DMSO before charging it. If the previously proposed decomposition mechanisms^[21,76] were thermodynamically favorable, a significant difference in the anodic linear scan voltammetry of the cell with and without resting time should be observed, yet the same OER capacity was recovered under 4V, as shown in **Figure 51**. The two charging plots suggest no self-charging by chemical decomposition of the Li_2O_2 to LiOH and recovery of the same capacity by scanning anodically to 4V. This is in good agreement with the following DFT calculations and prior experimental results, showing stability of Li_2O_2 in DMSO.

5.3 Density Functional Theory Study of DMSO/ Li_2O_2 Interfacial Stability

In order to further support our experimental findings regarding the stability of the Li_2O_2 /DMSO interface, through an EFRC collaboration with Dr. Kevin Leung and Dr. Nitin Kumar at Sandia National Laboratories in Albuquerque, NM, we have conducted a theoretical study of this system as well, and report herein thermodynamic and kinetic aspects of DMSO oxidation on peroxide and superoxide-terminated surfaces of Li_2O_2 .

Figure 7 depicts DMSO physisorbed on the superoxide (left) and peroxide (right) terminated surfaces. The $\text{Li}_{\text{surface}}\text{-O}_{\text{DMSO}}$ distances are 1.95 and 2.11 Å on the peroxide-terminated surface, and are larger (2.06 and 2.12 Å) on the superoxide surfaces. These bonds are

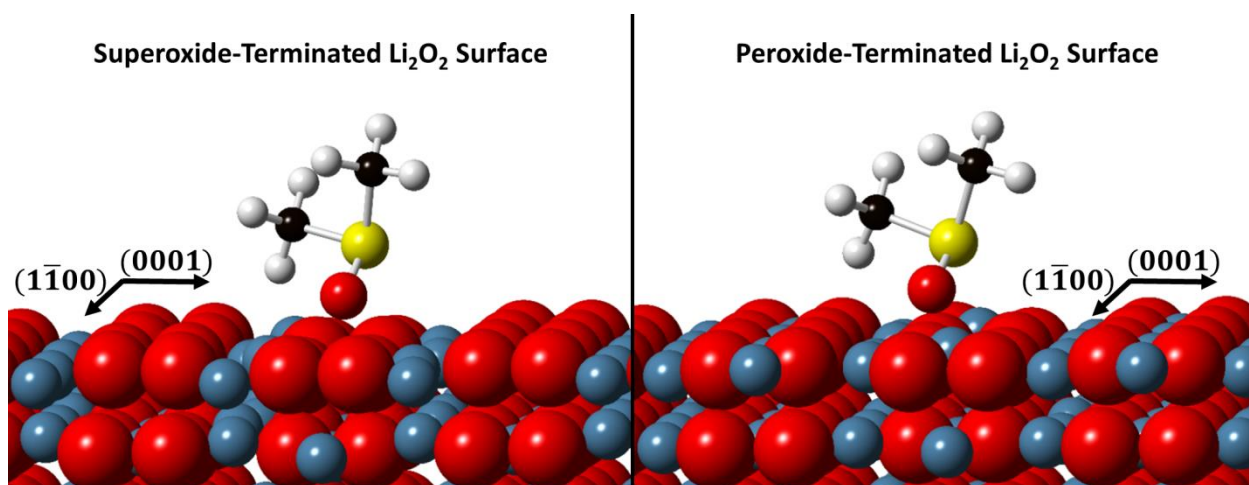


Figure 52: DMSO adsorbed atop superoxide (left) and peroxide (right) terminated Li_2O_2 surfaces.

shorter than Li-O bonds (2.16 Å) in bulk Li_2O_2 . We consider two low-energy terminations with different oxidation states for surface Li_2O_2 surface.^[33] The $(1\bar{1}20)$ stoichiometric surface consists of only peroxides (O_2^{2-}) moieties, and the simulation cell has a total of 160 atoms. The other cell has oxygen rich $(1\bar{1}20)$ Li_2O_2 surfaces decorated exclusively with superoxide (O_2^-) units (144 total atoms). These low energy peroxide (O_2^{2-}) and superoxide (O_2^-) terminations of Li_2O_2 are selected to study the reactivity of different surface oxygen oxidation states towards electrolyte decomposition.

The DMSO decomposition reaction pathway studied in this work proceeds with the splitting of an O_2 dimer on the Li_2O_2 surface near the physisorbed DMSO followed by abstraction of an H atom from DMSO. The abstracted H is transferred to one of the oxygen atoms with a broken bond, forming a hydroxyl on the surface. The other oxygen atom bonds with the sulfur in DMSO, forming a $\text{DMSO}_2\text{-H}$ complex. These steps appear to occur simultaneously and no stable reaction intermediate is observed. Wannier orbital analysis^[107] finds that the $\text{DMSO}_2\text{-H}$ is an anion. The Li_2O_2 slab has therefore gained an H^+ and lost an oxygen atom by the end of the reaction. The energy barrier associated with decomposition determines the reaction kinetics; hence, it is calculated to evaluate the probability of DMSO decomposition on Li_2O_2 by the suggested mechanism on the two different Li_2O_2 surface terminations (peroxide and superoxide).

The DFT/PBE calculations suggest that the DMSO decomposition barrier is lower on peroxide-terminated (0.75 eV) than on superoxide-terminated (1.43 eV) Li_2O_2 surface (**Figure 53**). This indicates that the decomposition is likely to occur on the peroxide-terminated surface. Also, the product of the degradation reaction is more exothermic on the peroxide (-2.08 eV) than on superoxide-terminated (-1.20 eV) Li_2O_2 surface. We repeated this barrier calculation for the

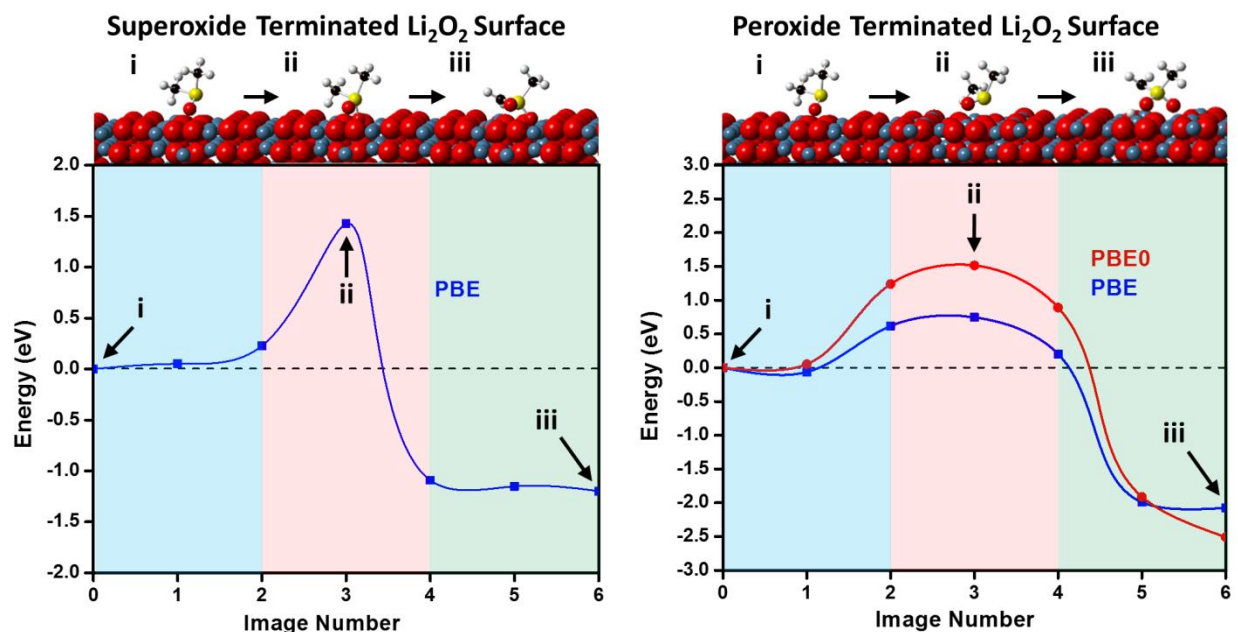


Figure 53: The NEB barrier for DMSO decomposition atop superoxide (a) and peroxide (b) terminated Li_2O_2 surfaces. The high precision PBE0 calculation (■ in (b)) predicts a higher barrier and an exothermicity that is lowered by 0.29eV.

peroxide-terminated surface using a more precise, but computationally expensive, hybrid PBE0 functional. In general, hybrid functionals are known to predict more accurate (and typically larger) reaction barriers than PBE.^[108] PBE0 barrier calculation results are shown in Figure 53b. This clearly shows that the barrier for DMSO decomposition on Li_2O_2 is around double (1.42 eV) the barrier obtained from PBE (0.75 eV). Moreover, the reaction is also found to be more exothermic (-2.51 eV) than that obtained from the PBE calculation (-2.08 eV). We have estimated reaction rate assuming Arrhenius behavior of the reactions with usual molecular vibrational prefactor of 10^{12} /sec at room temperature. A reaction barrier of 1.42 eV translates into a 10^{-5} reaction/month time frame (using the standard expression for reaction rate= $\exp(-\Delta E^*/k_B T)$, where $k_B T$ is the thermal energy at room temperature and κ is a prefactor on the order of 10^{12} /s, a 1.42 eV barrier roughly translates into a 20,000-year reaction time frame). Hence, the PBE0 barrier suggests that the DMSO decomposition is unlikely to occur even on the peroxide terminated surface.

Note that our PBE0-predicted DMSO reaction barrier is much higher than the DMSO (0.74eV)^[109] and TEGMDE (1.1 eV)^[109] decomposition barriers on a different, high surface energy, peroxide-terminated (1 $\bar{1}$ 00) facet of Li₂O₂, also predicted using DFT/PBE0. Our attempt to calculate the surface energy of the previously used facet yielded a surface energy of (1.71 Jm⁻²), more than 3 times higher than the surfaces considered in this work. We believe our calculations to represent the more realistic case, as lower energy surfaces are more likely to be present under the equilibrium or near-equilibrium conditions associated with battery storage or slow cycling.

Assuming that DMSO would undergo degradation following the reaction pathway studied in the present work under certain chemical/electrochemical conditions, we have conducted additional calculations to determine if the process would be self-limiting. The presumably (though unlikely) decomposed DMSO₂-H fragment is expected to have a strong affinity to the Li₂O₂ surface and affect subsequent decomposition reactions. Hence, we have tested the reactivity of a DMSO molecule atop a full monolayer of broken DMSO₂-H covered peroxide-terminated Li₂O₂ surface. **Figure 54** clearly shows that the DMSO decomposition reaction is endothermic (0.73eV) and the barrier for the reaction is

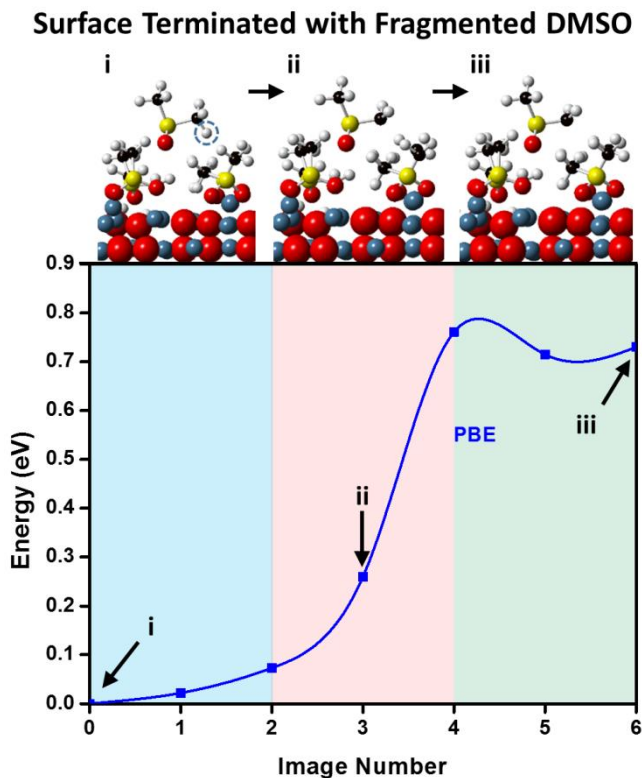


Figure 54: The NEB barrier for DMSO decomposition atop a monolayer of broken DMSO on peroxide terminated Li₂O₂ surface. The H that is abstracted from DMSO and transferred to the broken DMSO fragment is shown with the dashed circle in Image 0 (Frame i).

0.76 eV when using the PBE functional. As mentioned above, the more accurate PBE0 functional should predict an even higher barrier for this reaction. This shows that even if DMSO decomposes under some chemical/electrochemical conditions, further degradation of the electrolyte is unlikely to continue via the reaction pathway presented in this work.

Finally we considered the free energy change associated with the reaction $\text{DMSO} + \text{LiO}_2 \rightarrow \text{DMSO-H}:\text{Li}^+ + \text{HO}_2$ to examine the possibility of proton abstraction from DMSO by LiO_2 . This calculation addresses possible formation of hydroperoxy radical/anion by O_2^- and pure DMSO, as the hydroperoxy ion was previously demonstrated to oxidize DMSO to DMSO_2 . The reaction free energy is predicted to be +1.655 eV (+38.08 kcal mol⁻¹), an endothermic value that strongly suggests this reaction is unlikely to happen. When an explicit DMSO solvent molecule was included for LiO_2 and HO_2 , the free energy change is even more endothermic and the reaction is predicted to be even less likely to occur.

In summary, DMSO decompositions on superoxide, peroxide, and decomposed DMSO fragment-covered Li_2O_2 surfaces are predicted to either occur on time scales beyond battery life or experimental durations, or are thermodynamically unfavorable.

5.4 Discussion

The search for a suitable solvent for rechargeable Li-O₂ battery research, development, and commercialization is challenging, but fundamental and practical studies conducted in electrolytes with metastability under controlled operating conditions can provide insight regarding the desired physicochemical properties of the electrolyte and will drive progress in optimizing other components of the battery such as the cathode scaffold, separator and anode surface.

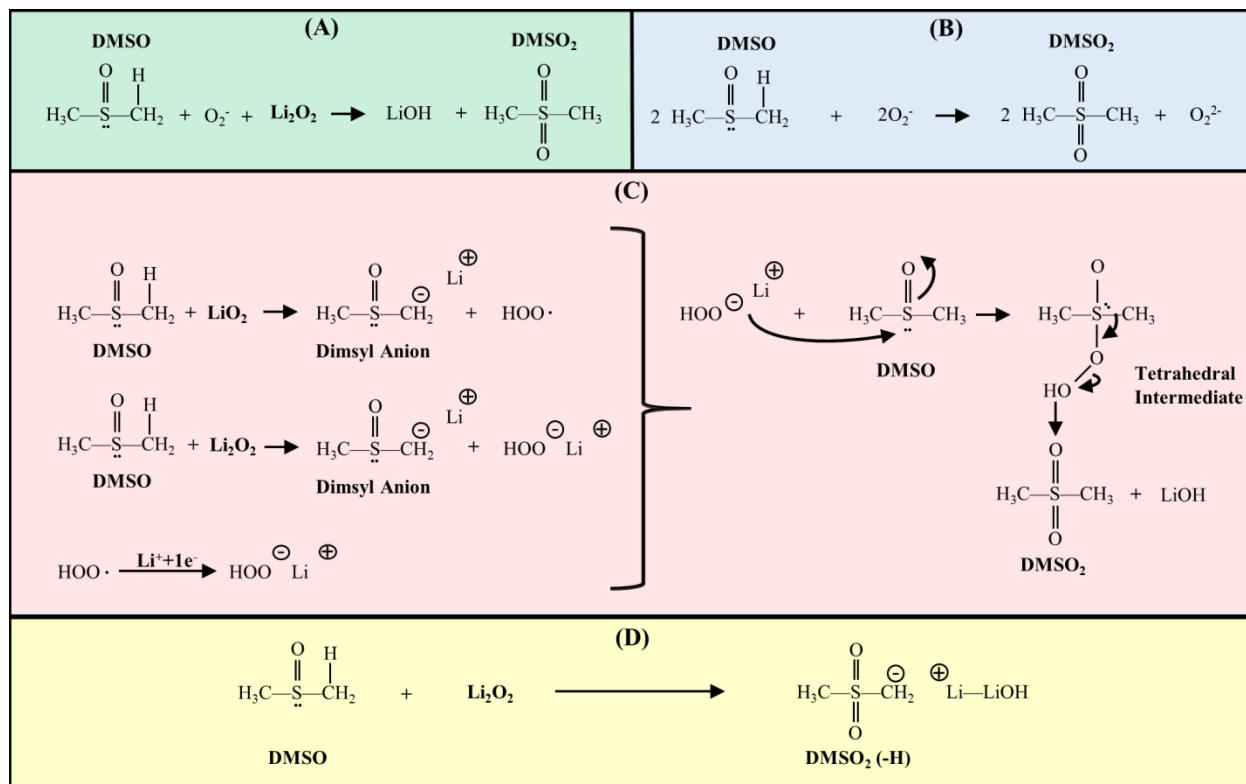
The theoretical work presented herein, supported by the presented comprehensive experimental studies, strongly suggest that oxidation of DMSO on Li_2O_2 is very unlikely to spontaneously occur, and will take place only under certain conditions, and to minor extent when operating at the voltages between 2.65-4V vs Li with environment free of acidic groups in the electrolyte or porous scaffold.

Though recent publications raised some concerns regarding the stability of DMSO under operating Li- O_2 battery, we believe that the results we present herein strongly suggest that under appropriate conditions DMSO can be used as a solvent to study and to gain important understanding of rechargeable Li- O_2 systems. We conjugate theoretical and experimental techniques to address the stability of DMSO/ Li_2O_2 interface and we believe that this is a comprehensive approach to fully understand possible mechanisms for electrolyte decomposition in electrochemical systems.

Previously suggested mechanisms for oxidation of DMSO are presented in **Scheme 2**. The reaction appearing in Scheme 2a suggests conjugated oxidation of DMSO and conversion of Li_2O_2 to LiOH. However, the reaction is unbalanced with respect to both atoms and charge, making it difficult to interpret the suggested mechanism. We found no evidence for the occurrence of this reaction in our system and the use of KO_2 as an oxidant as suggested in the relevant work was demonstrated herein to be inappropriate. Scheme 2b suggest mechanism that involves oxidation of DMSO by O_2^- and the simultaneous reduction of O_2^- to O_2^{2-} , however the electrochemical potential difference between O_2^- and O_2^{2-} reported to be 1.3V in DMSO^[96,97], and it is therefore not clear how the reaction is expected to be spontaneous.

The mechanisms presented in Scheme 2c involve the formation of a hydroperoxy radical and its reduction to hydroperoxy anion. This is with good agreement with the reaction reported

Scheme 2. Suggested Mechanisms for Oxidation of DMSO: (A)^[76], (B)^[94], (C)^[21], and (D), the mechanism proposed/studied in this work



by Sawyer and coworkers. However, we demonstrated herein that the source of the proton is very unlikely to be DMSO, and hence it must be abstracted from other, more acidic components in the system. As suggested by Sawyer and coworkers, if a source of acidic hydrogen is available in any of the cell components it may favor the oxidation of DMSO once reduced oxygen species are produced on the cathode. We suggest that the source of the proton can be in the salt^[96,97], trace H₂O^[94], or the use of activated carbon with acidic functional groups.^[21,110] The pK_a of all of those components are significantly lower than the pK_a of DMSO (>31)^[111], indicating that these components may be a precursor to DMSO oxidation.

Abstraction of a proton by reduced oxygen will induce the formation of a hydroperoxy anion. The strong Lewis acid (Li⁺) can then coordinate with the sulfoxide oxygen of DMSO, leading to nucleophilic attack by hydroperoxy-anion on the sulfur atom of the sulfoxide, and

yielding a central tetrahedral intermediate as previously suggested.^[21] The latter may collapse to the corresponding dimethyl sulfone (DMSO₂) and lithium hydroxide. Again, our work suggests that the acidity of methyl groups from DMSO itself is not strong enough to manifest proton abstraction from the DMSO molecule by Li₂O₂, suggesting that controlled exclusion of other proton sources will provide sufficiently stable conditions to prevent oxidation of DMSO on the cathode side in the potential window above 2.65V and below the potential of anodic oxidation.

Indeed previous reports on oxidation of DMSO used water containing electrolytes^[96,98], alkyl-ammonium based electrolyte^[97], Li-O₂ cell with self-reported leakage^[76], or microporous carbon^[21], all of which could contribute to the presence of acidic functional groups. We demonstrate that avoiding cell leakage, and hence any significant water content, together with the use of CNT@Pt cathode in which the low concentration acidic functional groups was passivated by the ALD process, established possible conditions for rechargeable Li-O₂ system for over 4 months of operation without noticeable oxidation of DMSO.

The operating potential is also hypothesized to affect the concentration of the superoxide and peroxide formed under ORR, with lower potentials leading to increased formation of reduced oxygen species (O₂⁻ or O₂²⁻ strong bases) that can abstract available weak acidic proton and facilitate the oxidation of the solvent.^[94] Cell operation at potentials above 2.65V vs Li and below 4V in the case of the cathodes presented herein will prevent oxidation of the solvent during discharge and will enable formation of rechargeable reduced oxygen species.

Although it is not the main focus of this work and may be further addressed in following studies, the anodic stability of DMSO during charge, in the presence of O₂, is reported to be dependent on the cathode material, and will take place at potentials above 4V on amorphous

microporous carbon^[21], or 4.2V in the case of Au/Pt electrodes.^[21,94] In the cathodes presented herein, anodic oxidation wasn't obtained by Raman for cell operated below 4V.

The porosity of the cathode may also be of great significant, since reduced oxygen in microporous cathodes (pore <2nm) may form locally high concentration of O₂⁻ with relatively low local concentration of DMSO.^[21] Our cathodes are mesoporous, and the mobility of the solvent molecules and reduced oxygen species is not anticipated to form this kind of locally high ratio between O₂⁻ and DMSO.

5.5 Conclusions

We have presented experimental and theoretical evidence for the chemical and electrochemical stability of the DMSO/Li₂O₂ interface under storage and operational conditions of a Li-O₂ battery. Experimentally, we demonstrated no surface change of Li₂O₂ aged in DMSO, and no oxidation of DMSO even after 7 months of storage. We synthesized core shell CNT@Pt Li-O₂ cathode via ALD and used it to further demonstrate long term operation of a Li-O₂ rechargeable battery with DMSO as the solvent for more than 4 months of continuous cycling, with a round trip cycle length of 80 hours when operated within a voltage range of 2.65-4V vs. Li/Li⁺. We show that presence of DMSO₂ cannot be measured effectively in the presence of K¹⁶O₂/Li¹⁶O₂ by Raman/FTIR due to the overlap between KO₂ and DMSO₂ in Raman and IR. Our theoretical models predict that DMSO decomposition on superoxide, peroxide, and decomposed DMSO fragment-covered Li₂O₂ surfaces will either occur on time scales beyond experimental durations, or are thermodynamically unfavorable. All of these findings strongly suggest that DMSO is a stable solvent for Li-O₂ cathode testing within a potential window of 2.65-4V, implying that DMSO is suitable for fundamental studies of Li-O₂ cells.

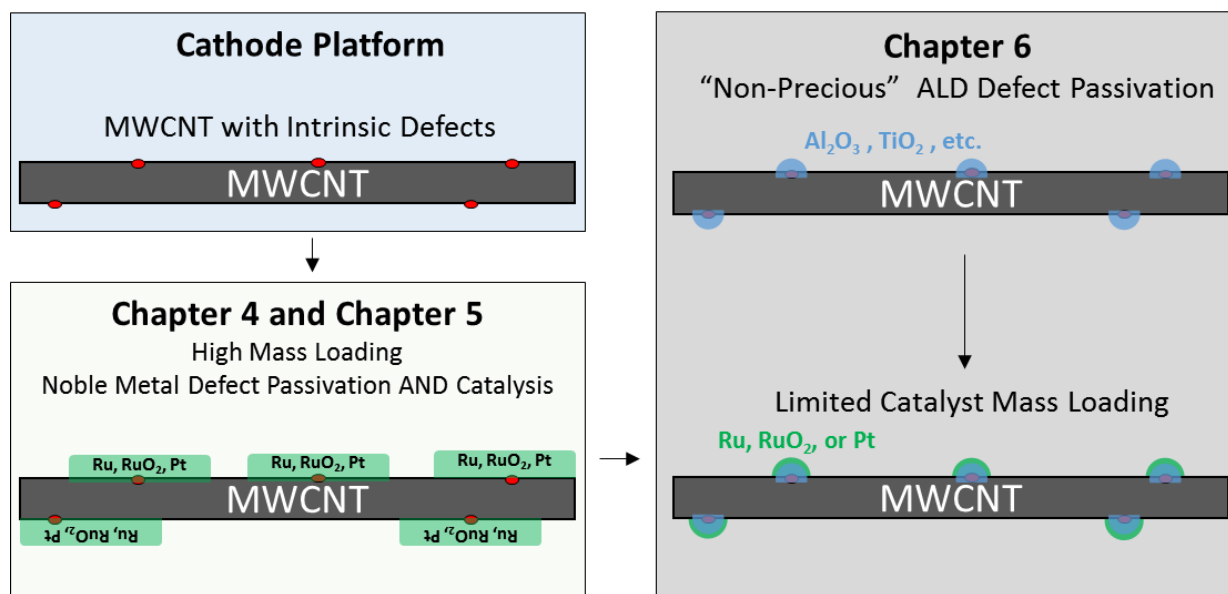
Chapter 6: Investigating the Interplay of ALD Defect Passivation and Catalysis for Practical Secondary Li-O₂ Cathodes

6.1 Introduction

The Li-O₂ literature and the previous chapters of this dissertation point toward two modes of improving the stability of carbon-based Li-O₂ cathodes—defect passivation and OER/ORR catalysis. The success of achieving both of these modes was demonstrated with core-shell structures deposited by atomic layer deposition of CNT@Ru in Chapter 4 and CNT@Pt in Chapter 5 of this dissertation. The concern is that the loading amounts of the ALD catalyst are a factor of one to three times the mass of the carbon scaffold in these cathodes, which essentially reverts back to the use of pure noble metal cathodes.^[102] This is a highly impractical vision for the continued development of Li-O₂ batteries based on the fact that these noble-metal based materials are notoriously scarce and expensive (according to *BASF Corp.* Pt: \$1188/oz and Ru: \$56.00/oz). The incorporation of a significant mass of heavy metal catalyst also jeopardizes the energy density of Li-O₂ batteries, which is its major advantage over the currently widespread lithium-ion technology. While their utility in improving OER/ORR performance is undeniable, these factors are a huge deterrent to further development and ultimate commercialization of the technology if a less expensive catalyst system is not made available.

Indeed, atomic layer deposition is certainly not the ideal discovery platform for new OER/ORR catalyst chemistries—a research avenue that is outside the scope of this project; however, this technique is extremely useful for optimizing material utilization and mass loading as a result of its selectivity and self-limiting mechanism. The oversight in Chapter 4 and 5 was employing the expensive noble metal ALD chemistry for both defect passivation AND catalysis. In reality, a non-precious, inexpensive baselayer (Al₂O₃, TiO₂) should perform just as well the

Scheme 3. Strategy for optimizing ALD functionalization of MWCNT scaffold as a practical route to long term cyclability



precious metal ALD chemistry at carbon defect passivation. This baselayer can then be superficially functionalized with a well-controlled, low mass loading of heterogenous ALD catalyst such as Ru, RuO₂, or Pt, as shown in **Scheme 3**.

A similar approach was attempted recently, using three cycles of ALD Al₂O₃ as a protective coating for a carbon black cathode scaffold followed by three cycles of ALD Pd.^[112] The authors claim some success with a significant reduction in overpotential and show 10 stable cycles to 500mAh g⁻¹. Unfortunately, they neglect to test (or share the results) the cyclability of the bare Super P carbon, which may exhibit similar cyclability at that capacity. They also show a significant increase in the first discharge overpotential after only 3 cycles of Al₂O₃ as compared to the bare Super P carbon. This seems unlikely as the defects they are passivating would provide energetically favorable sites for ORR (or a parasitic side reaction)^[19] and a noncontinuous layer of ~3Å of Al₂O₃ seems far from the amount required to generate such a significant voltage shift in ORR. Unlike the MWCNT sponge scaffold used in this work, the Super P carbon black is amorphous carbon with a very high intrinsic defect density. The authors also only report one

permutation of ALD cycles for Al₂O₃/Pd with little justification. As such, this system can still be significantly optimized in an effort to realize a stable, practical, Li-O₂ cathode.

6.2 Approach

For this study, we selected TiO₂ as the “non-precious” defect passivation ALD chemistry and Pt as the ALD catalyst. The processes, precursors, and conditions are all discussed in Chapter 7. Once again, the MWCNT sponge was used as the cathode scaffold based on our success with long term cycling stability and integration of ALD functionalities. Based on previous experience with long term cycling studies (one of the Ru cells ran continuously for over 4 months!), limited resources (cells/test channels) and the plan to try different combinations of interlayer thickness and catalyst loadings, there was a need for a quicker diagnostic of long term stability. Hence, we adopted higher rate galvanostatic cycling at reduced capacity as an accelerated test bed for cycling stability. We also placed a voltage limit window for cycling of 2-4.1V vs. Li/Li⁺ to keep the electrodes within the electrolyte stability window. For comparison, we cycled the pristine sponge, sponges with TiO₂ only, and sponges with TiO₂ and Pt to determine the relative enhancements in stability offered by each functionalization.

6.3 Results and Discussion

We first tested the cycling stability of the pristine sponge under the accelerated conditions (100 mA_g⁻¹ to 300 mA_h⁻¹). As shown in **Figure 55**, the untreated sponge was capable of delivering the requested

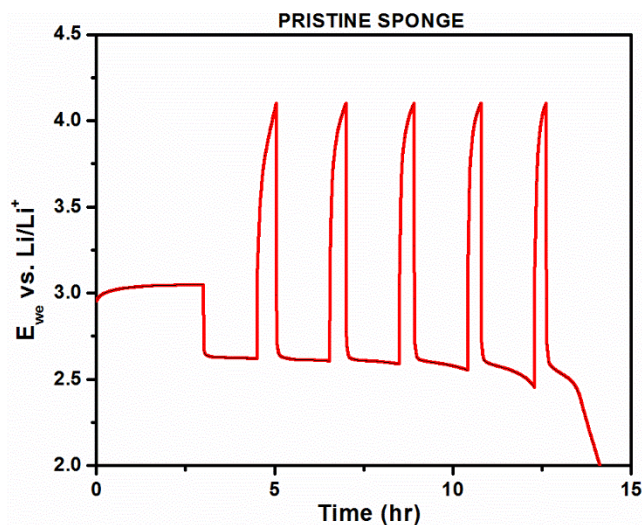


Figure 55: Galvanostatic cycling profile (300mA_g⁻¹ to 300mA_h⁻¹) to failure (2V lower limit) for the pristine MWCNT sponge.

discharge capacity for ~5 cycles. It is important to note that with constant current and a charge duration (voltage limited) that is only a fraction of the previous discharge duration (capacity limited), there will naturally be accumulation of reduction products over time, which is most likely the

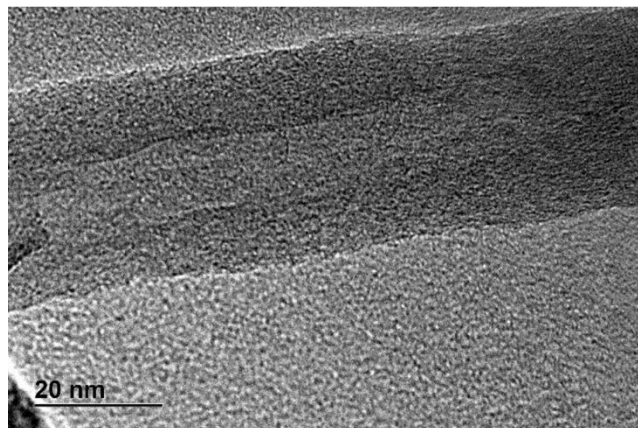


Figure 56: TEM image of MWCNT sponge after accelerated GV cycling test showing loss of crystallinity.

cause of failure on the 6th discharge. TEM characterization of this cathode after cycling, as shown in **Figure 56**, revealed that at least a significant number of the tubes had lost their crystallinity, most likely due to oxidation. Despite previous results suggesting that sp²-hybridized carbon was generally stable under the electrochemical conditions in a Li-O₂ cell^[19,29], this result held major implications regarding the original plan for functionalization, suggesting that partial coverage of the carbon surface may not be sufficient. Thus, rather than nucleation-based defect passivation and catalyst functionalization, we first shifted toward core-shell architectures of

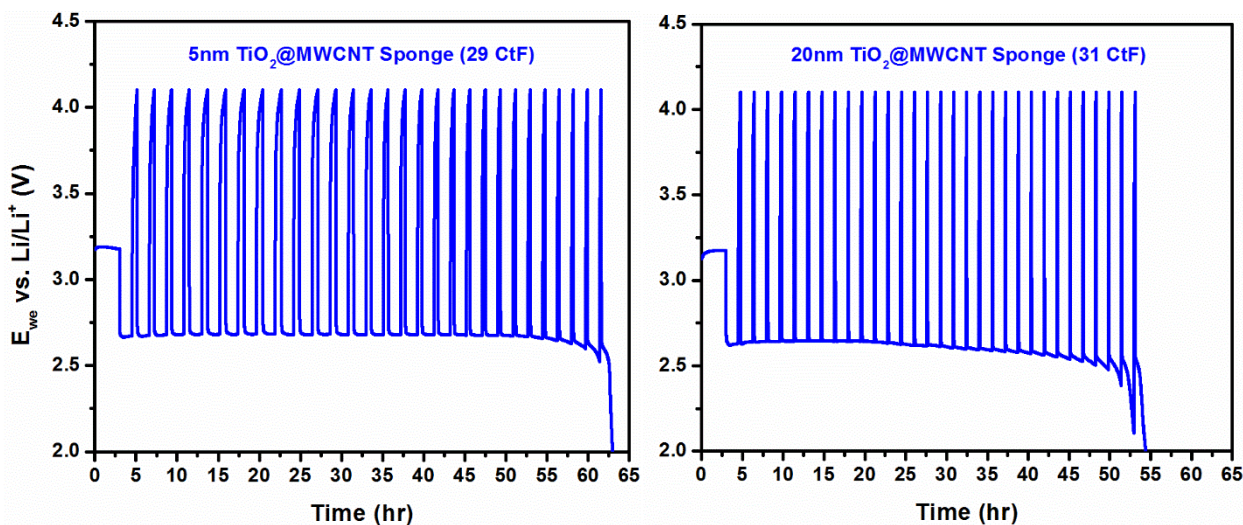


Figure 57: Galvanostatic cycling profile (300mA_g⁻¹ to 300MA_h⁻¹) of MWCNT sponge coated with two different thicknesses of ALD TiO₂. Despite a similar number of total cycles to failure (CtF), the cathode with the thinner TiO₂ layer exhibited slightly longer charge durations.

conformal protection layers (TiO_2). This displaces the carbon surface away from the electrochemically active interface to avoid these stability issues, but still realizes the advantages of the high surface area, mesoporous, and lightweight current collector. Galvanostatic cycling profiles of

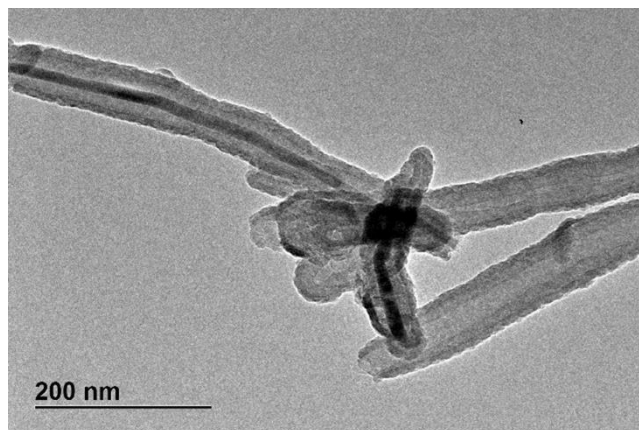


Figure 58: TEM image showing 100 cycles (~5nm) core-shell coating of ALD TiO_2 on MWCNT.

MWCNT sponges with two different thicknesses of ALD TiO_2 (5nm and 20nm) are shown in **Figure 57**. Both TiO_2 film thicknesses show a 5x enhancement in the total number of galvanostatic cycles as compared to the pristine sponge under the same conditions (Figure 55). The TEM image in **Figure 58** shows that the ALD process results in a MWCNT@ TiO_2 core-shell structure which is significantly more resistant to oxidation than the underlying carbon. Despite this surprising improvement, these structures are still plagued by considerable irreversibility, as indicated by the substantial discrepancy between the long discharge and subsequent, short charge durations. This indicates that the TiO_2 surface does not show sufficient OER activity to satisfy the preset galvanostatic rate within this potential window.

In an effort to improve reversibility, we then functionalized these MWCNT@ TiO_2 core-shell structures with atomic layer deposited platinum, which we have previously shown to exhibit significant enhancements in OER behavior (see Chapter 5). Due to the oxide surface, platinum deposition on the MWCNT@ TiO_2 core shell structure is significantly more conformal as compared to deposition directly on the pristine sponge, as shown in **Figure 59**. These TEM images show 75 cycles of ALD platinum on a pristine sponge (left) and a 5nm MWCNT@ TiO_2 coated sponge, respectively. This growth sequence allows for significantly improved control

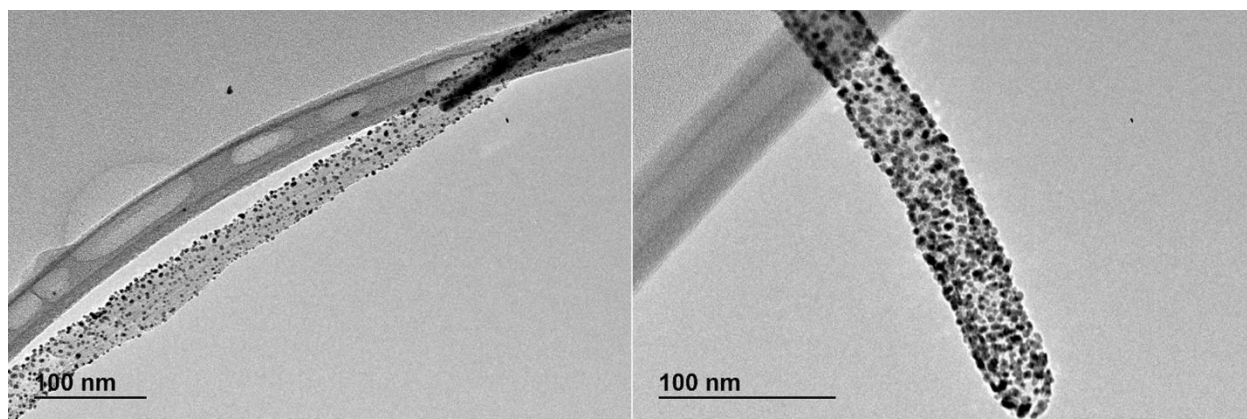


Figure 59: TEM images of 75 cycles of ALD Pt on pristine MWCNT sponge (left) and a 5nm MWCNT@TiO₂ core shell.

over lowering the mass loading while maintaining or increasing the effective surface area of the exposed catalyst, which dictates some of the kinetic limitations of OER/ORR catalysis.^[22,61]

Figure 60 shows the galvanostatic cycling performance of core-shell sponges with MWCNT@400cycTiO₂@75cycPt and MWCNT@100cycTiO₂@75cycPt. The double core-shell structure with the thinner TiO₂ interlayer exhibits slightly enhanced long term stability (because of enhanced reversibility, shown later). The addition of a Pt functionalization in both cases results in a ~5x improvement in cyclability as compared to the single core-shell MWCNT@TiO₂

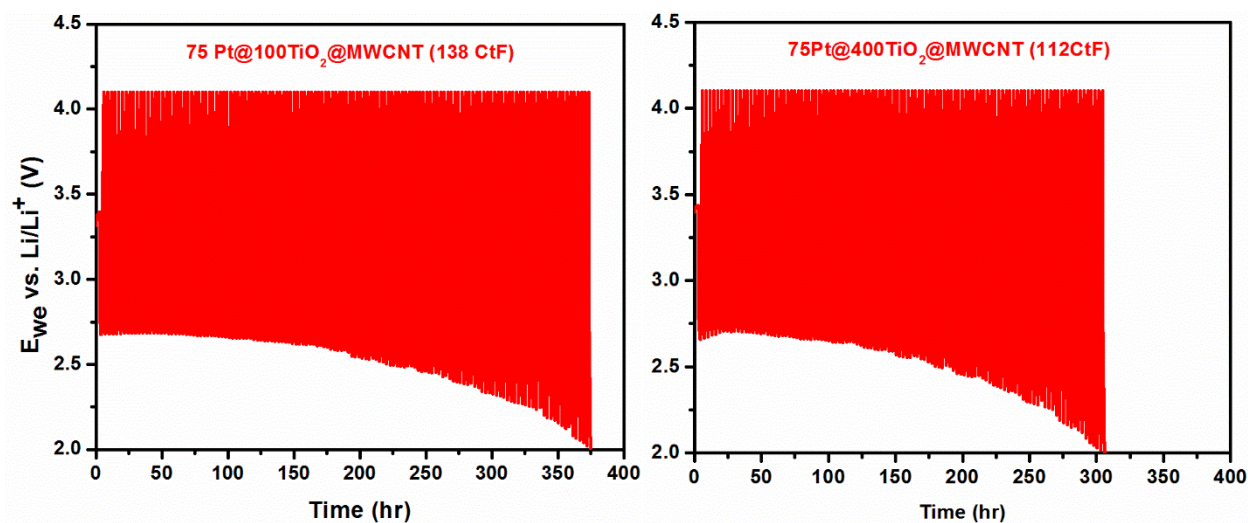


Figure 60: Galvanostatic cycling data under accelerated testing conditions (100mA_g⁻¹ to 300mA_h⁻¹) of TiO₂@Pt core shell cathodes with two different TiO₂ interlayer thicknesses (~5nm and 20nm). This data shows a slight enhancement in reversibility of the thinner TiO₂ layer. Both curves show a 5X improvement in cyclability as compared to MWCNT@TiO₂ and a 25X improvement as compared to the pristine sponge.

structures in Figure 57, and a $\sim 25\times$ improvement over the bare MWCNT sponge (Figure 55).

While these enhancements in performance are evident from the galvanostatic cycling plots, the reason for improved cyclability is not as obvious.

Figure 61 shows the first discharge and charge profile in the galvanostatic cycling

curves for each cathode. From this plot it is apparent that each of the cathodes discharge to the full capacity (300mAh_c), although the double core-shell cathodes functionalized with Pt do exhibit a higher ORR voltage for a significant fraction of discharge. This is favorable from a device perspective but most likely has no effect on long term stability. However, there are major differences in the charge capacity exhibited by these cells under the 4V upper limit. Under the same carbon mass-normalized current density (100mA_c), the order in recovered charge capacity is $20\text{nmTiO}_2 < \text{MWCNT} < 5\text{nmTiO}_2 < \text{MWCNT}@TiO_2@Pt$. This is generally the same trend observed for the long term cycling stability, indicating that the short term reversibility is a strong indicator for long term cyclability. This is expected since accumulation of discharge products is a known cause of failure in these cathodes.^[34]

Based on these trends, further efforts to optimize this structure included deposition of a thinner TiO_2 layer (40cycles for $\sim 2\text{nm}$) and reduced platinum loading (~ 25 cycles vs. 75 cycles) to determine if these thinner shell layers, as shown in **Figure 62**, can achieve similar improvements in stability. These cathodes were fabricated and cycled galvanostatically

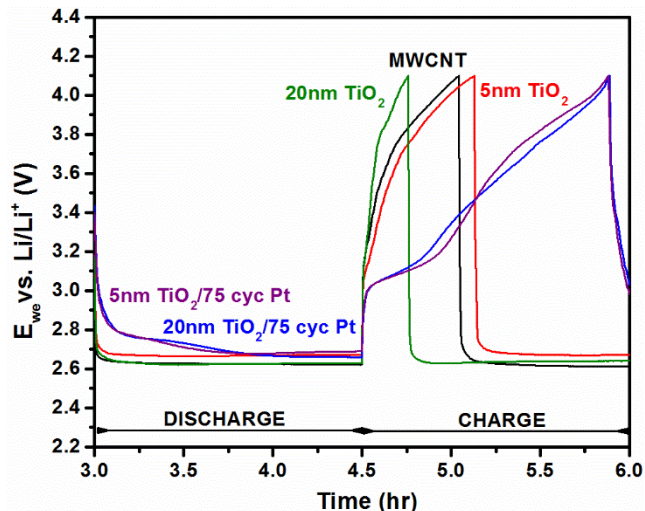


Figure 61: Profile of 1st discharge and charge under the accelerated galvanostatic cycling conditions. All cathodes discharge to the full capacity but there is a large discrepancy in charge capacity under the 4V upper limit as a result of the different surface functionalizations.

according to the same parameters. Accelerated galvanostatic cycling profiles for MWCNT@40TiO₂@25Pt and MWCNT@40TiO₂@75Pt are shown in **Figure 63**. In the case of left plot, 0.5:1 Pt:C loading results in an almost 3x boost in total cycles over structures cycled with no Pt catalyst (Figure 57). When the platinum

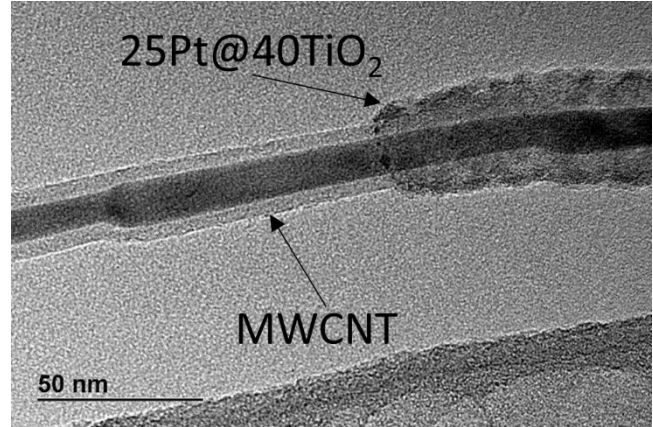


Figure 62: TEM image of MWCNT@TiO₂@Pt MWCNT double core shell structure with reduced ALD cycle counts (25 Pt and 40TiO₂) showing a conformal but thinner shell.

loading is increased to 4.5:1 Pt:C, as is the case with the second plot in Figure 63, the number of cycles roughly doubles (despite 9x the Pt loading), indicating that there are diminished returns in loading amounts beyond a surface layer of platinum.

6.4 Conclusions

At this point it is clear that the presented configurations of double core-shell structures are not completely optimized, but a few observed performance boosting trends are clear,

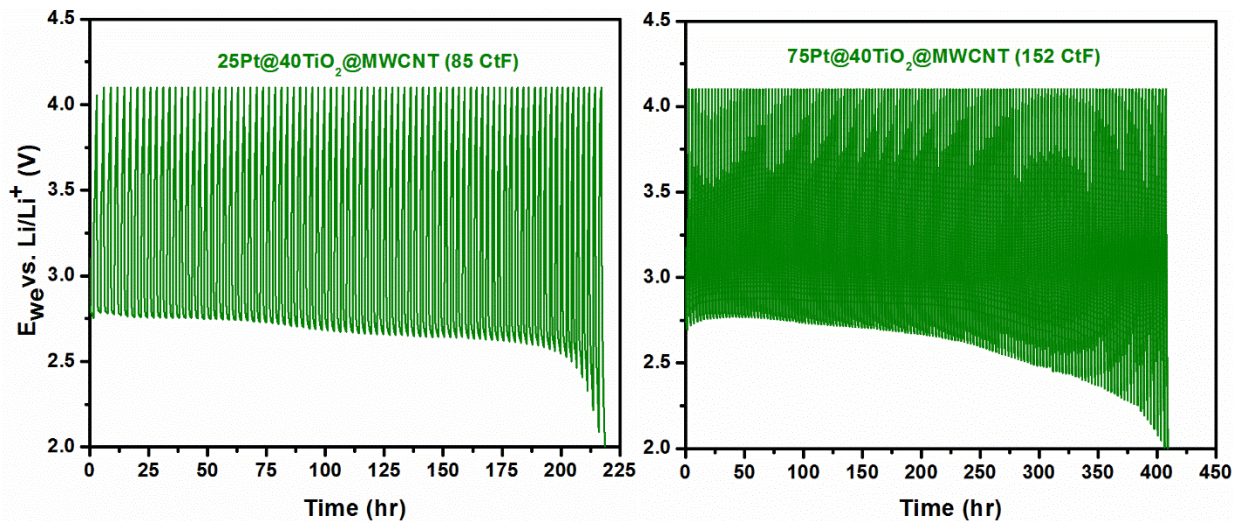


Figure 63: Galvanostatic cycling of cathodes with reduced Pt and TiO₂ loading. 25 ALD cycles of Pt shows a 3x improvement over the MWCNT@TiO₂ in Figure 57 and 75 cycles shows a significant improvement over the analogous structure with 100TiO₂ (Figure 60).

including thinning the TiO₂ layer while keeping it conformal to improve reversibility and limited but sufficient Pt mass loading for a conformal surface layer. Significant enhancements in accelerated galvanostatic cyclability have been linked to protection of the carbon (TiO₂) and functionalization with a OER/ORR catalyst, resulting in improved reversibility. Previous core shell structures of MWCNT@Ru, MWCNT@RuO₂, and MWCNT@Pt have been shown to greatly enhance performance but at the cost of a significant loading amount (~>3:1 catalyst:carbon) mass loading. In this regard, with improvements demonstrated for loadings as low as 0.5:1, these double core-shell cathode architectures are a promising option for significantly reducing the required loading of noble metal catalysts without compromising long term cyclability.

6.5 Future Work

The next step in studying the reversibility of these cathodes is an investigation of the surface chemistry of these cathodes after a single high capacity discharge and then again after charging under the same conditions (100mA_g⁻¹_c to 3,000mA_h⁻¹_c, voltage limited 2-4V vs. Li/Li⁺). Information regarding the static chemical state on the surface after a deep discharge and the surface recovery after a long charge will most likely help elucidate the respective cause of failure or mechanism for stable cycling in each structure, as we've shown previously (see Chapter 4). We are also in the process of running electrochemical tests on important comparison structures including a complete MWCNT@Pt core shell cathode for the accelerated, low capacity galvanostatic cycling and for a high capacity discharge and charge to study the voltage profile as compared to the structures presented herein. We are also testing a MWCNT@75cycPt without the TiO₂ stabilization layer to confirm a lack of stability with TiO₂ stabilization due to exposed carbon surface under the accelerated conditions.

In terms of future work over the long term, a variety of ALD materials can be tested within the framework of this architecture. One option is a more conductive interlayer to mitigate any voltage drop associated with the poor electronic conductivity of the amorphous ALD TiO₂.^[113] Along these lines, very recently (within the past month: Feb 10th, 2015), another study has investigated ALD FeO_x coatings on porous amorphous carbon decorated with palladium nanoparticles, showing an improvement in cyclability.^[114] The ALD FeO_x is electronically conductive and palladium is a known ORR catalyst.^[61] While TiN is an attractive option due to its excellent electronic conductivity, its susceptibility to oxidation and resulting loss of conductivity makes it inappropriate for this system.^[49] Incorporation of other catalyst systems or combinations of ALD catalysts (ORR and OER) via atomic doping and optimization of mass loading are also attractive options for future studies. In-situ TEM studies of ORR and OER behavior with respect to local catalyst proximity would also be extremely interesting.

6.6 Closing Perspectives

The nonaqueous Li-O₂ battery system is still less than 20 years old, and the challenges in developing working platforms for this technology can be traced back to each interface of the device. Pure lithium metal anodes are plagued by instability with respect to CO₂ and H₂O in open systems and the anode-electrolyte interface even in the presence of a pure O₂ source. Electrolyte stability is extremely sensitive at both electrode interfaces, and is highly dependent on a variety of factors including cell operating conditions, electrode composition, salt, and loading amount. Even research showing major improvements in cathode stability, such as the case studies presented herein, still show artifacts of setbacks in other device components (Chapter 4). In this regard, there is a great deal of fundamental research that must focus on stabilizing the dynamics of this chemistry at each component's interfaces (anode, solvent, salt,

cathode, and cell). This will gradually be accomplished with the types of approaches presented herein. Electrochemical testing, spectroscopic surface analysis, fundamental modeling studies and atomistic simulations complemented by empirical studies will all pave the way toward more stable devices.

Progress in the field is greatly hindered by the lack of metrics for standardization. Because of previously mentioned challenges in each device component and the field's nascence, there is no standard test cell, standard cathode for anode studies, standard anode for cathode studies, or electrolyte for electrode studies. Thus, each published system is essentially a unique representation of that particular group's beliefs regarding what may work best. This makes comparisons between even highly similar systems difficult. Thus, the field would greatly benefit from a collaborative effort to identify platforms for research based on the established literature.

Chapter 7: Appendix

7.1 Experimental Methods

This section describes the details of material preparation, instruments, and characterization methods not discussed in detail in the main text.

1. Material Preparation

MWCNT Sponge Synthesis^[72]: MWCNT sponges were synthesized by chemical vapor deposition (CVD) using 1,2-dichlorobenzene as the carbon source and ferrocene as the catalyst. Ferrocene powder was dissolved into 1,2-dichlorobenzene to make a solution with concentration of 0.06 g/mL. Then the source solution was injected into a 2-inch quartz tube housed in a CVD furnace by a syringe pump at a constant feeding rate of 0.13 mL/min. The carrying gas is a mixture of Ar and H₂, at a flowing rate of 2000 and 300 mL/min, respectively. Quartz slides were used as the growth substrate to deposit nanotubes in the center of furnace at a set reaction temperature of 860 °C. Typically we set the growth time to be 4 hours to obtain bulk sponge samples with thicknesses of about 8-10 mm. The sponge was then cut into 1/4" diameter discs before testing or coating with ALD.

Ru^[77] **and RuO₂ ALD**^[78]: A custom built cross-flow reactor with a base pressure of 10 mTorr was used to develop the Ru and RuO₂ ALD processes. The metalorganic Ru precursor, bis(2,6,6-trimethyl-cyclohexadienyl)-ruthenium, Ru(C₉H₁₃)₂ (or "Cyprus", Air Liquide), was loaded into a Strem electropolished stainless-steel bubbler and maintained at 80 °C. Ar (99.99%, Praxair) was flowed through the bubbler at 100 sccm. Research grade O₂ (99.999%, Praxair) was used as the oxidant and was flowed at 400 sccm. Timed Swagelok ALD valves controlled the dose for both precursors. One optimized ALD cycle consisted of the following pulse/purge sequence: 10 s

Ru(C₉H₁₃)₂ pulse, 5 s Ar purge, 5 s O₂ pulse (for Ru metal) or 30 s O₂ pulse for RuO₂ , 5 s Ar purge.

MnO ALD: The Ultratech FIJI F200 was outfitted with a bubbler with Bis(cyclopentadienyl)manganese(II) (a.k.a. Mn(EtCp)₂) held at 85°C. The reactor temperature for deposition was held at 170°C. A pulse structure of 0.5s-20s-0.06s-20s (Mn(EtCp)₂-wait-H₂O-wait) was used for the growth. Test films were characterized with XRD and XPS and determined to be MnO.

Pt ALD: Platinum ALD processes were performed with the Ultratech FIJI F200 with (Trimethyl)methylcyclopentadienylplatinum (IV) and oxygen. The Pt precursor was kept at 80°C and the reactor temperature was set to 270°C with pulse structure (2s Pt pulse, 30s exposure, 30s purge, O₂ exposure of 20sccm for 30s, 30s purge). Exposure processes involve closing the downstream butterfly valve and isolating the chamber from the pump to increase the residence time of the precursor and the conformality of deposition.

TiO₂ ALD: Atomic layer deposition of TiO₂ was performed in the University Fablab's *Beneq TFS 500* system with TDMAT (Tetrakis(dimethylamido)titanium) and water. The process temperature was 160°C with pulse structure (0.5s-1.5s-0.25s-0.25ms)

Sputtering: Sputtering of CVD growth catalysts (Ni, Fe) was performed with the Fablab's *AJA ATC 1800V* Sputtering System using a 200W Ar plasma stabilized at low pressure (4x10⁻³ torr). The samples were rotated on a chuck during the deposition for conformal growth.





Chemical Vapor Deposition: All carbon growth for the VACNT project was performed using the Fablab's Atomate Corporation's Low Pressure Chemical Vapor Deposition system. Ethylene and H_2 were used for the majority of growth processes, as outline in Chapter 3.



Electrolytes and Karl Fischer Coulometer: Electrolytes were prepared with anhydrous solvents from Sigma Aldrich (dimethyl sulfoxide (anhydrous, >99.9%), 1,2 dimethoxyethane (99.5%), diethylene glycol dimethyl ether (anhydrous diglyme, 99.5%), 1,3 dioxolane (anhydrous DOL, 99.8%)). These solvents were opened and stored in the glove box. The water impurity levels in the solvents were measured with a Metrohm 899 Coulometer, and were only used with values below 20ppm H_2O .



Salts (lithium perchlorate (LiClO_4), lithium bis(trifluoromethane)sulfonamide (LiTFSI)) were also acquired from Sigma-Aldrich and were baked in a vacuum oven for at least 24 hours at $T > 100^\circ\text{C}$ before loading into the glove box.

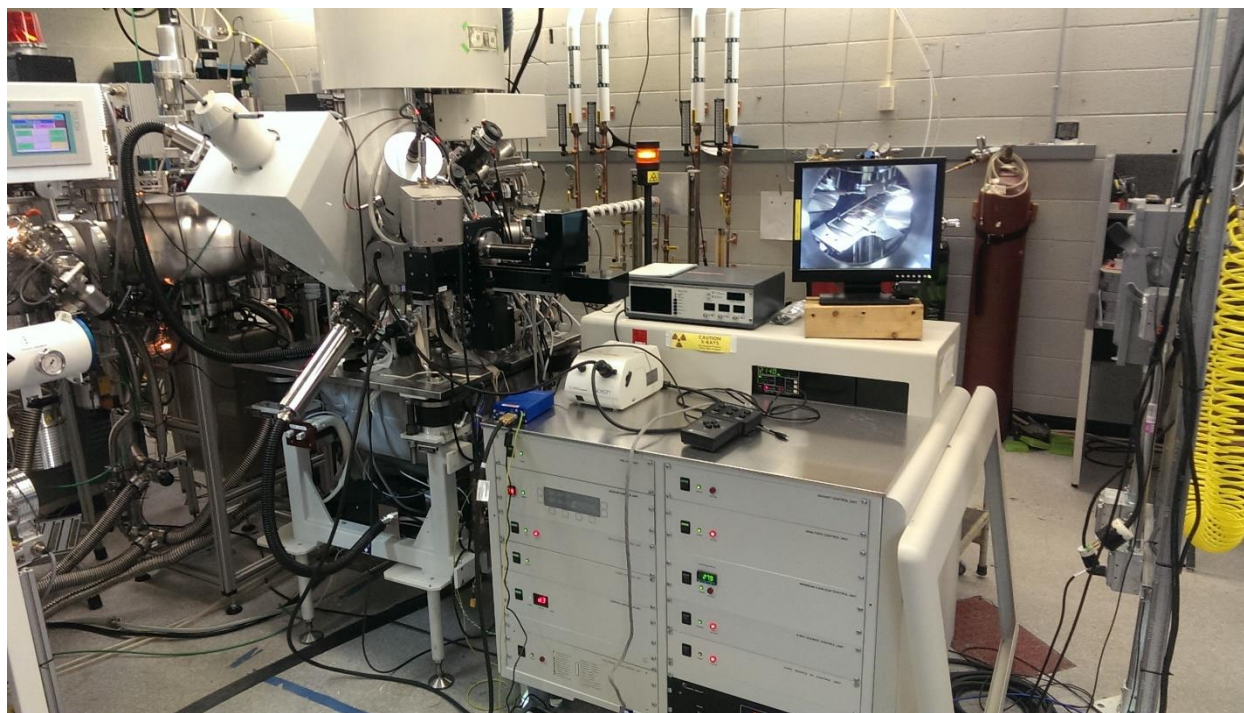
4. Characterization Tools

FTIR: All FTIR measurements were performed with a *Thermo Nicolet NEXUS 670* system with an Endurace Diamond ATR accessory.



Raman: Raman measurements were taken with a Horiba Jobin Yvon LabRam ARAMIS system with a 633nm laser. A 600gr/mm spatial resolution grating was used with 10x objective lens.

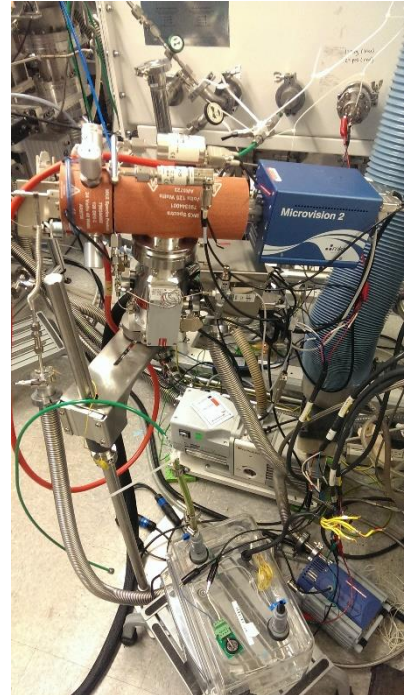




X-ray Photoelectron Spectroscopy (XPS): All XPS measurements featured in this work were taken with the Kratos Axis Ultra DLD in the Rubloff group's ANSLab. More typical measurements included analysis of charged and discharged cathodes to help determine the steady state chemistry developed under different cycling conditions. Samples from batteries were loaded directly from the integrated system's MBraun Ar-filled glove box to the XPS with the integrated high-vacuum transfer system, so the surface chemistry is generally considered unaltered. Characteristic measurements were taken using monochromated Al $K\alpha$ x-rays as the excitation source and with the instrument in hybrid (magnetic immersion) mode using the slot aperture. Survey spectra were taken with a step size of 1 eV and pass energy of 160eV. Individual high resolution spectra were collected using pass energy 20eV and a 0.1 or 0.05 eV step size. Samples which were anticipated to contain insulating products were electronically floated (isolated from the instrument ground) and charge compensation was provided entirely with the Kratos charge neutralization system in order to eliminate differential charging between

the products and the conductive scaffold. Peak fitting was performed using CasaXPS, using 50/50 Gaussian/Lorentzian lineshapes on a Shirley background.

Mass Spectroscopy: Mass spectroscopy of cell headspaces was tested using an MKS Microvision 2 residual gas analyzer (RGA) with differentially pumped atmospheric sampling adaptor.



Ellipsometer: The J.A. Woollam M-2000D spectroscopic ellipsometer was instrumental in characterizing ALD film thicknesses for determination of sample growth rates and process development.



7.2 Hendricks Energy Research Fellowship Proposal

12th December 2011

ABSTRACT

The ultimate goal of this project is to successfully fabricate a 3-dimensional, high-aspect ratio, all-solid-state, lithium- O_2 battery. This goal will be achieved upon successful completion and integration of three research stages. Before a complete lithium- O_2 battery can be fabricated, component processing must be qualified and optimized. The first stage will focus on optimizing the processing of the anode, cathode, and electrolyte, as well as characterizing these device components. Once each of these parts has been successfully fabricated and characterized separately, the second research stage will concentrate on component integration and battery testing in the form of a planar, thin-film $Li - O_2$ battery test-structure. Successful fabrication and testing of this simple device design will warrant shifting towards the final stage of this project, fabrication and testing of the 3-dimensional, high-aspect ratio, all-solid-state, lithium-air battery design shown in Figure 5.

BACKGROUND

Energy storage has rapidly become one of the prime technological challenges of the 21st century. The recent proliferation of portable electronics and the search for cleaner alternatives to a fossil fuel dominated energy infrastructure have motivated tremendous efforts in a variety of potential outlets, but in battery research in particular. Recent trends in battery applications have included miniaturization, increased functionality, and growing power demands. This challenge is further convoluted by consumer expectations for increased battery life, compact size, room temperature operation, durability and safety. While lithium-ion battery technology has been fairly successful in accommodating these trends up to this point, the material systems involved are approaching their limits. It is time for battery science to catch up with its new prospective applications, namely hybrid/electric vehicles and storage of renewable energies, by shifting research efforts toward a new paradigm with a greater performance potential—the lithium- O_2 battery.

Conventionally, lithium- O_2 batteries consist of a pure lithium metal anode, an electrolyte that conducts lithium ions but is electronically resistive, and a porous carbon cathode designed to promote diffusion and reduction of oxygen, as shown in Figure 1. One of the unique features of this system (and other metal-air chemistries) is that the cathode oxidant, oxygen, is readily obtained from the surrounding environment rather than being stored in the electrode like most other battery technologies. The benefits of using lithium include its low atomic mass and high electropositivity, which lead to a greater energy density and higher cell voltage, respectively. The specifics of the $Li-O_2$ cell operation and the current research challenges facing this technology are available in the literature.¹

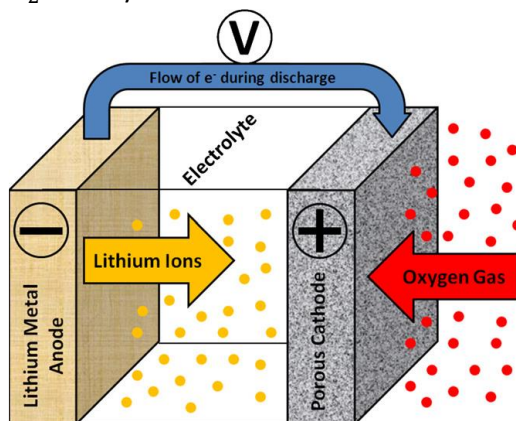


Figure 1: Schematic of a Lithium- O_2 battery.¹

As shown in Figure 2, the lithium- O_2 battery chemistry grants the possibility of an energy density that is 5 – 10 times greater than that of current lithium-ion batteries, and is theoretically comparable to gasoline—a requirement if this technology will one day replace hydrocarbons as the energy source for automobiles. Power density is also a very important factor to consider—the amount of stored energy is insignificant if it cannot be released according to the demands of the application. Figure 3 shows a comparison of practical (experimentally achievable) power and energy densities. Despite the fact that research of this electrochemical system is in its infancy, the lithium-air battery already shows promise toward exceeding the current standard, the lithium-ion battery.

The material systems that have been chosen for this project are motivated by functionality, the existing equipment available for fabrication, and by the ultimate goal to fabricate a 3D, thin film, all-solid state battery. The solid state electrolyte, $LiAlO_2$, has a high room-temperature ionic conductivity ($1.3E - 4 S cm^{-1}$), low electronic conductivity and can be deposited as a conformal thin-film with a well-controlled thickness using a process called atomic layer deposition². The lithium metal anode is the standard for this battery chemistry. The cathode is the most complex component of this material system. I have elected to explore mesoporous carbon as a possibility because the porous structure is conducive to oxygen diffusion to the electrolyte interface, it exhibits good electrical conductivity and dimensional stability over charge/discharge cycling, can potentially catalyze the reduction reaction.³ Mesoporous carbon is commercially available and can also be deposited using chemical vapor deposition or wet chemical processes.

RESEARCH PLAN

The research for this project will take place in three major stages. The first stage will focus on the qualification of the component (cathode, anode, and solid-state electrolyte) fabrication processes and subsequent characterization of these material systems to ensure that they are suitable for the device. Regarding optimization of the $LiAlO_2$ process, the Rubloff group is already very familiar with atomic layer deposition. We have an existing furnace reactor that will be used to process these films and have recently acquired the necessary precursors for another project. Characterization of this film will require electrochemical impedance spectroscopy (EIS), in order to measure the Li^+ ionic conductivity,

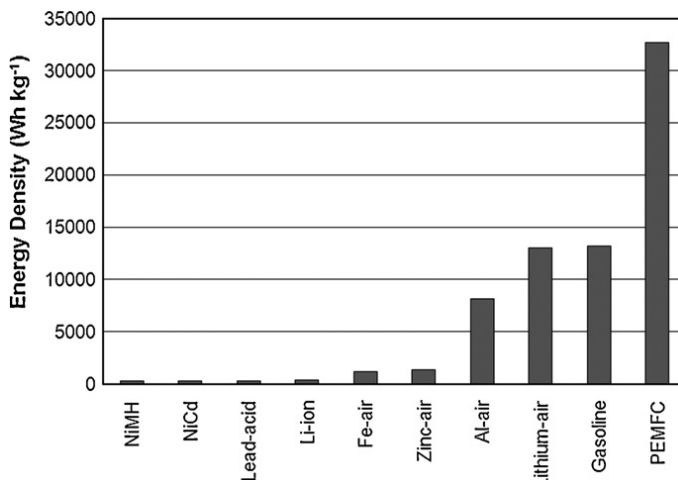


Figure 2: Comparison of theoretical energy densities of current and developing energy storage technologies.¹

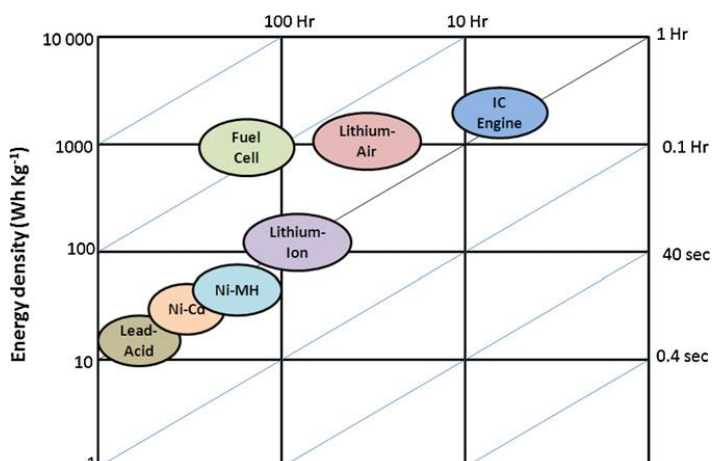


Figure 3: Practical power and energy densities of current energy storage technologies.¹

and basic electrical characterization to ensure that the electrolyte will not short the battery. In order to safely work with lithium metal as the anode material, we will need to purchase and install a glove box on the ALD system as a result of Lithium's extreme reactivity with ambient moisture. With a glove box, it will be possible to perform electrochemical deposition and thermal evaporation of lithium metal films in a safe, clean environment. Finally, the carbon cathode will be deposited using the *Atomate* chemical vapor deposition reactor in the clean room of the Kim Engineering building. This process has already been explored by other group members and will only need to be tuned for this application.

Once the materials have been successfully fabricated and characterized individually, it will be appropriate to move on to the second stage of research, component integration, by building the test-structure shown in Figure 4. The purpose of this planar, thin-film structure is to begin addressing any potential problems with the layer interfaces, film thicknesses, and general device performance in the simplest way possible.

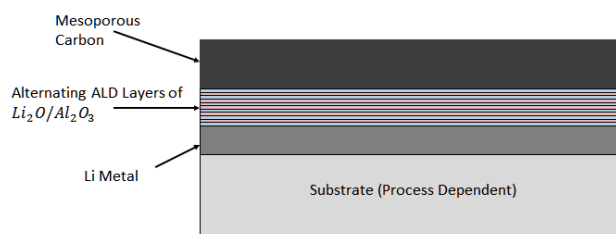


Figure 4: Planar Li-O₂ test-structure (Research Stage II)

The final research stage will be to fabricate the 3-dimensional, high-aspect ratio, all-solid-state, lithium-air battery shown in Figure 5. Using a commercial anodized aluminum oxide membrane as a high aspect ratio template, I will then electroplate or evaporate a thin layer of lithium metal. The solid state electrolyte, $LiAlO_2$, will then be fabricated by depositing ALD monolayers of lithium oxide and aluminum oxide and then annealing at $370^\circ C$.² Finally, using the previously discussed CVD process, we can deposit the mesoporous cathode. Pending any major issues with fabrication, it will then be appropriate to characterize this new battery structure. Metrics of particular interest will be power and energy density measurements, cyclability, charge retention, charging efficiency, overpotentials, and cell voltage.

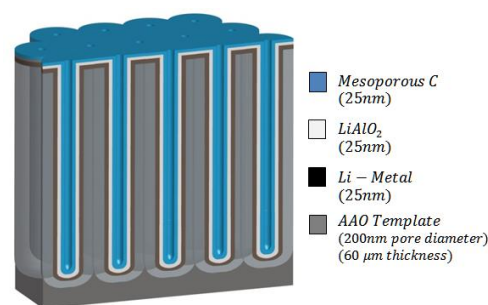


Figure 5: 3D drawing of the proposed high aspect ratio Li-Air Battery.

RESULTS AND FUTURE FUNDING

This project incorporates multiple proposed paradigm shifts in battery design that could potentially pave the way to future technologies. The all-solid-state, 3D, high aspect ratio, thin-film architecture combined with the relatively young nature of the $Li-O_2$ electrochemical energy conversion process promises to provide some interesting results if a prototype can be successfully fabricated. The use of ALD for the deposition of a solid-state electrolyte in an all-solid-state, thin film battery is also a relatively novel concept, and is sure to draw the attention of the ALD community. If the research presents the interesting results it potentially promises, I would certainly look to the DOE, the NSF, and other energy related funding agencies to continue the project.

Sources

- Padbury, R., and X. Zhang. "Lithium-Oxygen Batteries--limiting Factors That Affect Performance." *Journal of Power Sources* (2011).
 Kinoshita, K., J. W. Sim, and J. P. Ackerman. "Preparation and Characterization of Lithium Aluminate." *Materials Research Bulletin* 13.5 (1978): 445-455.
 Winter, M., et al. "Insertion Electrode Materials for Rechargeable Lithium Batteries." *Advanced Materials* 10.10 (1998): 725-763

References

- [1] I. E. A. (Iea), **2014**, DOI 10.1787/weo-2014-en.
- [2] P. Denholm, E. Ela, B. Kirby, M. Milligan, *Nrel* **2010**, 1.
- [3] N. Imanishi, A. Luntz, P. Bruce, *The Lithium Air Battery*, Springer Science & Business Media, **2014**.
- [4] E. L. Littauer, *J. Electrochem. Soc.* **1977**, *124*, 850.
- [5] E. L. Littauer, *J. Electrochem. Soc.* **1976**, *123*, 964.
- [6] K. M. Abraham, in *ECS Trans.*, ECS, **2008**, pp. 67–71.
- [7] K. M. Abraham, *J. Electrochem. Soc.* **1996**, *143*, 1.
- [8] S. Kuzhikalail M. Abraham, Needham; Zhiping Jiang, **1996**, 9.
- [9] R. Padbury, X. Zhang, *J. Power Sources* **2011**, *196*, 4436.
- [10] C. O. Laoire, S. Mukerjee, E. J. Plichta, M. a. Hendrickson, K. M. Abraham, *J. Electrochem. Soc.* **2011**, *158*, A302.
- [11] C. O. Laoire, S. Mukerjee, K. M. Abraham, E. J. Plichta, M. a. Hendrickson, *J. Phys. Chem. C* **2009**, *113*, 20127.
- [12] J. Hassoun, F. Croce, M. Armand, B. Scrosati, *Angew. Chemie - Int. Ed.* **2011**, *50*, 2999.
- [13] Z. Peng, S. a. Freunberger, L. J. Hardwick, Y. Chen, V. Giordani, F. Bardé, P. Novák, D. Graham, J. M. Tarascon, P. G. Bruce, *Angew. Chemie - Int. Ed.* **2011**, *50*, 6351.
- [14] P. G. Bruce, S. a. Freunberger, L. J. Hardwick, J.-M. Tarascon, *Nat. Mater.* **2011**, *11*, 172.
- [15] B. D. McCloskey, D. S. Bethune, R. M. Shelby, G. Girishkumar, a. C. Luntz, *J. Phys. Chem. Lett.* **2011**, *2*, 1161.
- [16] B. D. McCloskey, a. Speidel, R. Scheffler, D. C. Miller, V. Viswanathan, J. S. Hummelshøj, J. K. Nørskov, a. C. Luntz, *J. Phys. Chem. Lett.* **2012**, *3*, 997.
- [17] W. Xu, V. V. Viswanathan, D. Wang, S. a. Towne, J. Xiao, Z. Nie, D. Hu, J. G. Zhang, *J. Power Sources* **2011**, *196*, 3894.
- [18] B. M. Gallant, R. R. Mitchell, D. G. Kwabi, J. Zhou, L. Zuin, C. V. Thompson, Y. Shao-Horn, *J. Phys. Chem. C* **2012**, *116*, 20800.

- [19] M. M. Ottakam Thotiyl, S. a. Freunberger, Z. Peng, P. G. Bruce, *J. Am. Chem. Soc.* **2013**, *135*, 494.
- [20] S. Meini, M. Piana, N. Tsiouvaras, A. Garsuch, H. a. Gasteiger, *Electrochem. Solid-State Lett.* **2012**, *15*, A45.
- [21] D. Sharon, M. Afri, M. Noked, A. Garsuch, A. a. Frimer, D. Aurbach, *J. Phys. Chem. Lett.* **2013**, *4*, 3115.
- [22] Y.-C. Lu, H. a. Gasteiger, M. C. Parent, V. Chiloyan, Y. Shao-Horn, *Electrochem. Solid-State Lett.* **2010**, *13*, A69.
- [23] T. Suntola, J. Autson, *U.S. Pat. Trademark Off.* **1977**.
- [24] M. Leskelä, M. Ritala, *Thin Solid Films* **2002**, *409*, 138.
- [25] S. M. George, *Chem. Rev.* **2010**, *110*, 111.
- [26] R. W. Johnson, A. Hultqvist, S. F. Bent, *Mater. Today* **2014**, *17*, 236.
- [27] Z. Guo, D. Zhou, X. Dong, Z. Qiu, Y. Wang, Y. Xia, *Adv. Mater.* **2013**, *25*, 5668.
- [28] R. R. Mitchell, B. M. Gallant, C. V. Thompson, Y. Shao-Horn, *Energy Environ. Sci.* **2011**, *4*, 2952.
- [29] D. M. Itkis, D. a. Semenenko, E. Y. Kataev, A. I. Belova, V. S. Neudachina, A. P. Siroтина, M. Hävecker, D. Teschner, A. Knop-Gericke, P. Dudin, A. Barinov, E. a. Goodilin, Y. Shao-Horn, L. V. Yashina, *Nano Lett.* **2013**, *13*, 4697.
- [30] P. Albertus, G. Girishkumar, B. McCloskey, R. S. Sánchez-Carrera, B. Kozinsky, J. Christensen, a. C. Luntz, *J. Electrochem. Soc.* **2011**, *158*, A343.
- [31] J. S. Hummelshøj, J. Blomqvist, S. Datta, T. Vegge, J. Rossmeisl, K. S. Thygesen, a. C. Luntz, K. W. Jacobsen, J. K. Nørskov, *J. Chem. Phys.* **2010**, *132*, 071101.
- [32] S. P. Ong, Y. Mo, G. Ceder, *Phys. Rev. B - Condens. Matter Mater. Phys.* **2012**, *85*, DOI 10.1103/PhysRevB.85.081105.
- [33] M. D. Radin, J. F. Rodriguez, F. Tian, D. J. Siegel, *J. Am. Chem. Soc.* **2012**, *134*, 1093.
- [34] A. Kraysberg, Y. Ein-Eli, *J. Power Sources* **2011**, *196*, 886.
- [35] X. H. Yang, P. He, Y. Y. Xia, *Electrochem. commun.* **2009**, *11*, 1127.
- [36] C. Tran, X. Q. Yang, D. Qu, *J. Power Sources* **2010**, *195*, 2057.

- [37] T. Kuboki, T. Okuyama, T. Ohsaki, N. Takami, *J. Power Sources* **2005**, *146*, 766.
- [38] L. Camilli, M. Scarselli, S. Del Gobbo, P. Castrucci, F. Nanni, E. Gautron, S. Lefrant, M. De Crescenzi, *Carbon N. Y.* **2011**, *49*, 3307.
- [39] M. Karwa, Z. Iqbal, S. Mitra, *Carbon N. Y.* **2006**, *44*, 1235.
- [40] D. Park, Y. H. Kim, J. K. Lee, *J. Mater. Sci.* **2003**, *38*, 4933.
- [41] Y. Fu, S. Chen, J. Bielecki, A. Matic, T. Wang, L. L. Ye, J. Liu, *Mater. Lett.* **2012**, *72*, 78.
- [42] P. M. Parthangal, R. E. Cavicchi, M. R. Zachariah, *Nanotechnology* **2007**, *18*, 185605.
- [43] E. Teblum, M. Noked, J. Grinblat, A. Kremen, M. Muallem, Y. Flegler, Y. R. Tischler, D. Aurbach, G. D. Nessim, *J. Phys. Chem. C* **2014**, *118*, 140721161954004.
- [44] W. Lin, R. Zhang, K. S. Moon, C. P. Wong, *IEEE Trans. Adv. Packag.* **2010**, *33*, 370.
- [45] K. a. Wepasnick, B. a. Smith, J. L. Bitter, D. Howard Fairbrother, *Anal. Bioanal. Chem.* **2010**, *396*, 1003.
- [46] B. M. Gallant, D. G. Kwabi, R. R. Mitchell, J. Zhou, C. V Thompson, Y. Shao-Horn, *Energy Environ. Sci.* **2013**, *6*, 2518.
- [47] M. C. Guenette, M. D. Tucker, M. Ionescu, M. M. M. Bilek, D. R. McKenzie, *J. Appl. Phys.* **2011**, *109*, 083503.
- [48] J. Musschoot, Q. Xie, D. Deduytsche, S. Van den Berghe, R. L. Van Meirhaeghe, C. Detavernier, *Microelectron. Eng.* **2009**, *86*, 72.
- [49] J. H. Yun, E. S. Choi, C. M. Jang, C. S. Lee, *Japanese J. Appl. Physics, Part 2 Lett.* **2002**, *41*, L418.
- [50] C. R. Oliver, E. S. Polsen, E. R. Meshot, S. Tawfick, S. J. Park, M. Bedewy, a. J. Hart, *ACS Nano* **2013**, *7*, 3565.
- [51] J. Q. Huang, Q. Zhang, M. Q. Zhao, F. Wei, *Carbon N. Y.* **2010**, *48*, 1441.
- [52] M. Wang, T. Li, Y. Yao, H. Lu, Q. Li, M. Chen, Q. Li, *J. Am. Chem. Soc.* **2014**, *136*, 18156.
- [53] N. Dementev, S. Osswald, Y. Gogotsi, E. Borguet, *J. Mater. Chem.* **2009**, *19*, 7904.
- [54] P. X. Hou, C. Liu, H. M. Cheng, *Carbon N. Y.* **2008**, *46*, 2003.
- [55] A. Cao, X. Zhang, C. Xu, J. Liang, D. Wu, B. Wei, *J. Mater. Res.* **2001**, *16*, 3107.

- [56] S. Evers, L. F. Nazar, *Acc. Chem. Res.* **2013**, *46*, 1135.
- [57] R. Cao, J. S. Lee, M. Liu, J. Cho, *Adv. Energy Mater.* **2012**, *2*, 816.
- [58] S. H. Oh, L. F. Nazar, *Adv. Energy Mater.* **2012**, *2*, 903.
- [59] Z.-L. Wang, D. Xu, J.-J. Xu, X.-B. Zhang, *Chem. Soc. Rev.* **2013**, 10.1039/c3cs60248f.
- [60] F. S. Gittleston, R. C. Sekol, G. Doubek, M. Linardi, A. D. Taylor, *Phys. Chem. Chem. Phys.* **2014**, *16*, 3230.
- [61] Y. C. Lu, H. a. Gasteiger, Y. Shao-Horn, *J. Am. Chem. Soc.* **2011**, *133*, 19048.
- [62] N. Garcia-Araez, P. Novák, *J. Solid State Electrochem.* **2013**, *17*, 1793.
- [63] J. An, Y.-B. Kim, F. B. Prinz, *Phys. Chem. Chem. Phys.* **2013**, *15*, 7520.
- [64] C. C. Chao, M. Motoyama, F. B. Prinz, *Adv. Energy Mater.* **2012**, *2*, 651.
- [65] N. P. Dasgupta, C. Liu, S. Andrews, F. B. Prinz, P. Yang, *J. Am. Chem. Soc.* **2013**, *135*, 12932.
- [66] S. T. Christensen, H. Feng, J. L. Libera, N. Guo, J. T. Miller, P. C. Stair, J. W. Elam, *Nano Lett.* **2010**, *10*, 3047.
- [67] K. L. Pickrahn, S. W. Park, Y. Gorlin, H. B. R. Lee, T. F. Jaramillo, S. F. Bent, *Adv. Energy Mater.* **2012**, *2*, 1269.
- [68] Y. Lei, J. Lu, X. Luo, T. Wu, P. Du, X. Zhang, Y. Ren, J. Wen, D. J. Miller, J. T. Miller, Y. K. Sun, J. W. Elam, K. Amine, *Nano Lett.* **2013**, *13*, 4182.
- [69] J. Lu, L. Cheng, K. C. Lau, E. Tyo, X. Luo, J. Wen, D. Miller, R. S. Assary, H.-H. Wang, P. Redfern, H. Wu, J.-B. Park, Y.-K. Sun, S. Vajda, K. Amine, L. a. Curtiss, *Nat. Commun.* **2014**, *5*, 4895.
- [70] H. D. Lim, H. Song, J. Kim, H. Gwon, Y. Bae, K. Y. Park, J. Hong, H. Kim, T. Kim, Y. H. Kim, X. Leprö, R. Ovalle-Robles, R. H. Baughman, K. Kang, *Angew. Chemie - Int. Ed.* **2014**, *53*, 3926.
- [71] R. Younesi, M. Hahlin, M. Roberts, K. Edström, *J. Power Sources* **2013**, *225*, 40.
- [72] X. Gui, J. Wei, K. Wang, A. Cao, H. Zhu, Y. Jia, Q. Shu, D. Wu, *Adv. Mater.* **2010**, *22*, 617.
- [73] Z. Jian, P. Liu, F. Li, P. He, X. Guo, M. Chen, H. Zhou, *Angew. Chemie - Int. Ed.* **2014**, *53*, 442.

- [74] H. G. Jung, Y. S. Jeong, J. B. Park, Y. K. Sun, B. Scrosati, Y. J. Lee, *ACS Nano* **2013**, *7*, 3532.
- [75] B. Sun, P. Munroe, G. Wang, *Sci. Rep.* **2013**, *3*, 2247.
- [76] D. G. Kwabi, T. P. Batcho, C. V. Amanchukwu, N. Ortiz-Vitoriano, P. Hammond, C. V. Thompson, Y. Shao-Horn, *J. Phys. Chem. Lett.* **2014**, *5*, 2850.
- [77] K. Gregorczyk, L. Henn-Lecordier, J. Gatineau, C. Dussarrat, G. Rubloff, *Chem. Mater.* **2011**, *23*, 2650.
- [78] K. E. Gregorczyk, A. C. Kozen, X. Chen, M. a. Schroeder, M. Noked, A. Cao, L. Hu, G. W. Rubloff, *ACS Nano* **2015**, *9*, 464.
- [79] Y. Xuan, Y. Q. Wu, T. Shen, M. Qi, M. a. Capano, J. a. Cooper, P. D. Ye, *Appl. Phys. Lett.* **2008**, *92*, 013101.
- [80] X. Wang, S. M. Tabakman, H. Dai, *J. Am. Chem. Soc.* **2008**, *130*, 8152.
- [81] E. Yilmaz, C. Yogi, K. Yamanaka, T. Ohta, H. R. Byon, *Nano Lett.* **2013**, *13*, 4679.
- [82] M. M. Ottakam Thotiyil, S. a Freunberger, Z. Peng, Y. Chen, Z. Liu, P. G. Bruce, *Nat. Mater.* **2013**, *12*, 1050.
- [83] D. G. Kwabi, T. P. Batcho, C. V. Amanchukwu, N. Ortiz-Vitoriano, P. Hammond, C. V. Thompson, Y. Shao-Horn, *J. Phys. Chem. Lett.* **2014**, *5*, 2850.
- [84] S. a. Freunberger, Y. Chen, Z. Peng, J. M. Griffin, L. J. Hardwick, F. Bardé, P. Novák, P. G. Bruce, *J. Am. Chem. Soc.* **2011**, *133*, 8040.
- [85] K. P. C. Yao, D. G. Kwabi, R. a. Quinlan, a. N. Mansour, a. Grimaud, Y.-L. Lee, Y.-C. Lu, Y. Shao-Horn, *J. Electrochem. Soc.* **2013**, *160*, A824.
- [86] E. N. Nasybulin, W. Xu, B. L. Mehdi, E. Thomsen, M. H. Engelhard, R. C. Massé, M. Gu, W. Bennett, Z. Nie, C. Wang, N. D. Browning, J. Zhang, P. Bhattacharya, *ACS Appl. Mater. Interfaces* **2014**, *6*, 14141.
- [87] S. Tanuma, C. J. Powell, D. R. Penn, *Surf. Interface Anal.* **2005**, *37*, 1.
- [88] P. L. . Gunter, O. L. . Gijzeman, J. . Niemantsverdriet, *Appl. Surf. Sci.* **1997**, *115*, 342.
- [89] Y.-C. Lu, B. M. Gallant, D. G. Kwabi, J. R. Harding, R. R. Mitchell, M. S. Whittingham, Y. Shao-Horn, *Energy Environ. Sci.* **2013**, *6*, 750.
- [90] C. O. Laoire, S. Mukerjee, K. M. Abraham, E. J. Plichta, M. a. Hendrickson, *J. Phys. Chem. C* **2010**, *114*, 9178.

- [91] K. U. Schwenke, S. Meini, X. Wu, H. a Gasteiger, M. Piana, *Phys. Chem. Chem. Phys.* **2013**, *15*, 11830.
- [92] D. Sharon, V. Etacheri, A. Garsuch, M. Afri, A. a. Frimer, D. Aurbach, *J. Phys. Chem. Lett.* **2013**, *4*, 127.
- [93] S. a. Freunberger, Y. Chen, N. E. Drewett, L. J. Hardwick, F. Bardé, P. G. Bruce, *Angew. Chemie - Int. Ed.* **2011**, *50*, 8609.
- [94] N. Mozhzhukhina, L. P. Méndez De Leo, E. J. Calvo, *J. Phys. Chem. C* **2013**, *117*, 18375.
- [95] R. Younesi, P. Norby, T. Vegge, *ECS Electrochem. Lett.* **2014**, *3*, A15.
- [96] A. D. Goolsby, D. T. Sawyer, *Anal. Chem.* **1968**, *40*, 83.
- [97] M. V. Merritt, D. T. Sawyer, *J. Org. Chem.* **1970**, *35*, 2157.
- [98] P. Krtil, L. Kavan, I. Hoskovcova, K. Kratochvilova, *J. Appl. Electrochem.* **1996**, *26*, 523.
- [99] F. S. Gittleson, W.-H. Ryu, A. D. Taylor, *ACS Appl. Mater. Interfaces* **2014**, *6*, 19017.
- [100] L. Johnson, C. Li, Z. Liu, Y. Chen, S. a. Freunberger, P. C. Ashok, B. B. Praveen, K. Dholakia, J.-M. Tarascon, P. G. Bruce, *Nat. Chem.* **2014**, *6*, 1091.
- [101] K. Duerr, J. Olah, R. Davydov, M. Kleimann, J. Li, N. Lang, R. Puchta, E. Hübner, T. Drewello, J. N. Harvey, N. Jux, I. Ivanović-Burmazović, *Dalton Trans.* **2010**, *39*, 2049.
- [102] Z. Peng, S. a. Freunberger, Y. Chen, P. G. Bruce, *Science (80-.)*. **2012**, *337*, 563.
- [103] L. Legrand, a. Tranchant, R. Messina, F. Romain, a. Lautie, *Inorg. Chem.* **1996**, *35*, 1310.
- [104] M. Herstedt, D. P. Abraham, J. B. Kerr, K. Edström, *Electrochim. Acta* **2004**, *49*, 5097.
- [105] B. J. Lindberg, K. Hamrin, G. Johansson, U. Gelius, a Fahlman, C. Nordling, K. Siegbahn, *Phys. Scr.* **1970**, *1*, 286.
- [106] G. Girishkumar, B. McCloskey, a. C. Luntz, S. Swanson, W. Wilcke, *J. Phys. Chem. Lett.* **2010**, *1*, 2193.
- [107] N. Marzari, D. Vanderbilt, *Phys. Rev. B* **1997**, *56*, 22.
- [108] N. Sai, K. Leung, J. Zádor, G. Henkelman, *Phys. Chem. Chem. Phys.* **2014**, *16*, 8092.
- [109] T. Laino, A. Curioni, *New J. Phys.* **2013**, *15*, 095009.

- [110] C. O. Ania, V. Khomenko, E. Raymundo-Piñero, J. B. Parra, F. Béguin, *Adv. Funct. Mater.* **2007**, *17*, 1828.
- [111] W. S. Matthews, J. E. Bares, J. E. Bartmess, F. G. Bordwell, F. J. Cornforth, G. E. Drucker, Z. Margolin, R. J. McCallum, G. J. McCollum, N. R. Vanier, *J. Am. Chem. Soc.* **1975**, *97*, 7006.
- [112] J. Lu, Y. Lei, K. C. Lau, X. Luo, P. Du, J. Wen, R. S. Assary, U. Das, D. J. Miller, J. W. Elam, H. M. Albishri, D. A. El-Hady, Y.-K. Sun, L. a Curtiss, K. Amine, *Nat. Commun.* **2013**, *4*, 2383.
- [113] S. Hu, M. R. Shaner, J. a Beardslee, M. Lichterman, B. S. Brunshwig, N. S. Lewis, *Science* **2014**, *344*, 1005.
- [114] J. Xie, X. Yao, Q. Cheng, I. P. Madden, P. Dornath, C.-C. Chang, W. Fan, D. Wang, *Angew. Chem. Int. Ed. Engl.* **2015**.
- [115] K. G. Gallagher, S. Goebel, T. Greszler, M. Mathias, W. Oelerich, D. Eroglu, V. Srinivasan, *Energy Environ. Sci.* **2014**, *7*, 1555.
- [116] P. a. Cox, J. B. Goodenough, P. J. Tavener, D. Telles, R. G. Egdell, *J. Solid State Chem.* **1986**, *62*, 360.
- [117] D. Briggs, G. Beamson, Z. C. Z. Plc, T. S. Uk, *Anal. Chem.* **2002**, *65*, 1517.
- [118] Y. Kaga, *Surf. Sci. Spectra* **1999**, *6*, 68.